



Terms and Conditions of Use of Digitised Theses from Trinity College Library Dublin

Copyright statement

All material supplied by Trinity College Library is protected by copyright (under the Copyright and Related Rights Act, 2000 as amended) and other relevant Intellectual Property Rights. By accessing and using a Digitised Thesis from Trinity College Library you acknowledge that all Intellectual Property Rights in any Works supplied are the sole and exclusive property of the copyright and/or other IPR holder. Specific copyright holders may not be explicitly identified. Use of materials from other sources within a thesis should not be construed as a claim over them.

A non-exclusive, non-transferable licence is hereby granted to those using or reproducing, in whole or in part, the material for valid purposes, providing the copyright owners are acknowledged using the normal conventions. Where specific permission to use material is required, this is identified and such permission must be sought from the copyright holder or agency cited.

Liability statement

By using a Digitised Thesis, I accept that Trinity College Dublin bears no legal responsibility for the accuracy, legality or comprehensiveness of materials contained within the thesis, and that Trinity College Dublin accepts no liability for indirect, consequential, or incidental, damages or losses arising from use of the thesis for whatever reason. Information located in a thesis may be subject to specific use constraints, details of which may not be explicitly described. It is the responsibility of potential and actual users to be aware of such constraints and to abide by them. By making use of material from a digitised thesis, you accept these copyright and disclaimer provisions. Where it is brought to the attention of Trinity College Library that there may be a breach of copyright or other restraint, it is the policy to withdraw or take down access to a thesis while the issue is being resolved.

Access Agreement

By using a Digitised Thesis from Trinity College Library you are bound by the following Terms & Conditions. Please read them carefully.

I have read and I understand the following statement: All material supplied via a Digitised Thesis from Trinity College Library is protected by copyright and other intellectual property rights, and duplication or sale of all or part of any of a thesis is not permitted, except that material may be duplicated by you for your research use or for educational purposes in electronic or print form providing the copyright owners are acknowledged using the normal conventions. You must obtain permission for any other use. Electronic or print copies may not be offered, whether for sale or otherwise to anyone. This copy has been supplied on the understanding that it is copyright material and that no quotation from the thesis may be published without proper acknowledgement.

VORTEX SHEDDING LOCK-IN
OF A 2-D WIND TURBINE
BLADE SECTION AT HIGH
ANGLES OF ATTACK

ALBERTO PELLEGRINO

Department of Mechanical & Manufacturing Engineering

Parsons Building

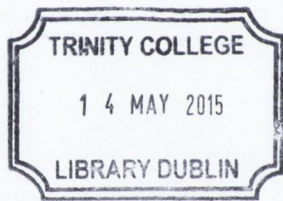
Trinity College

Dublin 2

Ireland

March 2015

A thesis submitted to the University of Dublin in partial
fulfillment of the requirements for the degree of Ph.D.

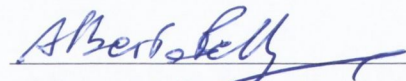


Thesis 10581

Declaration

I declare that this thesis has not been submitted as an exercise for a degree at this or any other university and it is entirely my own work.

I agree to deposit this thesis in the University's open access institutional repository or allow the library to do so on my behalf, subject to Irish Copyright Legislation and Trinity College Library conditions of use and acknowledgement.



Alberto Pellegrino, March 2015

Abstract

The vortex shedding behaviour of a 2-D wind turbine blade section at high angles of attack ($\alpha = [35^\circ \rightarrow 145^\circ]$) has been investigated using unsteady RANS with the transition SST turbulence model. The Reynolds number is $Re = 10^6$ based on a chord length of 1m. The airfoil examined is the NREL S809 (Phase-VI).

Initially, the unsteady flow around the fixed airfoil has been simulated to calculate the vortex shedding frequency, f_{v0} , (or the Strouhal number) for each angle of attack considered. The range of the vortex shedding frequencies obtained, non-dimensionalised by the projected chord of the airfoil, is $[0.11 < St < 0.16]$. The fluctuating coefficients at the harmonics of the fundamental vortex shedding frequency for lift, drag and pitching moment are presented; significant contributions at the higher harmonics have been observed. Generally, it is inferred that the camber of the airfoil does not substantially affect the force coefficients, suggesting that the results presented may be applicable to turbine blades of different geometry.

Secondly, a parametric study on vortex shedding frequency lock-in of the airfoil in forced oscillation has been conducted. It is well known that, in bluff body flows, oscillations can lead to a synchronisation (lock-in) of the vortex shedding frequency, f_v , with the body's motion frequency, f_m . In order to investigate the susceptibility of the airfoil to lock-in, the frequency ratio, $r = f_m/f_{v0}$, has been varied. Three single degrees of freedom are considered in isolation: prescribed sinusoidal pitching, stream-wise and transverse motion. Different mean angles of attack, vibration frequencies and vibration amplitudes have been considered and the lock-in region boundaries have been proposed. Generally, synchronisation is present for all the types of motions examined, although different behaviours have been observed. For example, the stream-wise motion appears to be the least likely to synchronise, compared to the pitching and transverse motion. In order to investigate the

effect that the stream-wise motion has on the transverse and pitching lock-in behaviour, two 2-degrees of freedom couplings have been examined (coupled stream-wise/transverse and stream-wise/pitching motion). Different behaviours have been observed, depending on the relative amplitude and phase of the two coupled motions, and on the orientation of the airfoil with respect to the flow. In addition, the relative path travelled by the airfoil and by the shed vortex (formed on the upwind edge) seems to strongly affect the interaction between the coupled motions.

In addition, a lumped parameter model (wake oscillator model) has been proposed for single degree of freedom oscillating airfoils in pitching and transverse motion. An acceptable qualitative agreement with the CFD results has been achieved for the pitching motion, whereas the model fails to predict the transverse motion behaviour. A more complex modelling is needed to become a reliable means for the assessment of VIV risk.

Acknowledgments

First of all, I would like to thank Dr. Craig Meskell for his competent guidance, confident help, fatherly support/patience during these years. I would have achieved nothing without him.

Thanks to all the Fluids Lab guys, past and present, for the enjoyable time together and the interesting conversations from time to time. In particular thanks to Kevin for the company late in the night during these last “thesis months”, started together - finished together (thanks Sajad for keeping the office quiet, at last...being away during the last crucial month in August!).

Thanks to the “Italian party”, Cristina and Andrea, for the close friendship grown from a working context.

A special thanks goes to Laura for these years lived together. Her support has been important, even fundamental in one particular occasion. This achievement is also a result of her caring attitude.

Thanks also to my parents, their interest/presence has not been affected by the distance! And thanks to my sister Federica for the multiple visits here in Dublin.

This research is carried out under the EU FP7 ITN project SYSWIND (Grant No. PITN-GA-2009-238325). The SYSWIND project is funded by the Marie Curie Actions under the Seventh Framework Programme for Research and Technological Development of the EU. I would like to thank the organisers of SYSWIND, especially Prof. Biswajit Basu (Trinity College, Dublin).

Computations have been conducted on the Irish Centre for High-End Computing (ICHEC) systems.

“When everything seems to be going against you, remember that the airplane takes off against the wind, not with it.”

Henry Ford

Nomenclature

c	Airfoil's chord
d	Generic characteristic length (cylinder's diameter)
f	Frequency
f^*	Non-dimensional frequency
f_m	Generic motion frequency
f_p	Pitching motion frequency
f_s	Stream-wise motion frequency
f_t	Transverse motion frequency
f_v	Vortex shedding frequency
f_{v0}	Static vortex shedding frequency
p	Pressure
q	Wake variable
r	Frequency ratio
s	Generic displacement
t	Time
x	Horizontal displacement
y	Vertical displacement
A	Coupling force factor
A_s	Stream-wise motion amplitude
A_t	Transverse motion amplitude
C_d	Drag force coefficient
C_{f0}	Generic mean force coefficient
C_l	Lift force coefficient
C_m	Pitching moment coefficient

D	Drag force
L	Lift force
M	Pitching moment
R_A	Amplitude ratio
U_∞	Freestream velocity
α	Instantaneous angle of attack (and angle of attack for static configuration)
α_{ampl}	Pitching motion amplitude
α_{mean}	Mean angle of attack (moving configuration)
ε	Damping factor
μ	Flow dynamic viscosity
ρ	Flow density
τ	Non-dimensional time

CFD	Computational Fluid Dynamics
DOF	Degree of Freedom
LE	Airfoil's leading edge
PSD	Power spectral density
Re	Reynolds number
St	Strouhal number
SST	Shear Stress Transport
TE	Airfoil's trailing edge
UDF	User Defined Function
VIV	Vortex-induced vibration

Contents

Declaration	ii
Abstract	xii
1 Introduction	1
1.1 Context	2
1.2 Objectives and Overview	4
1.3 Publications	6
2 Literature Review	7
2.1 Vortex shedding	8
2.1.1 Cylinders.	12
2.1.2 Prismatic bodies.	13
2.2 Static airfoils	17
2.2.1 Flat plates and elliptic sections.	17
2.2.2 Wind turbine blades.	19
2.3 Frequency lock-in	20
2.3.1 Transverse motion (heave, y).	23
2.3.2 Stream-wise motion (in-line, x).	24
2.3.3 Coupled stream-wise/transverse motion (x, y).	26
2.4 Oscillating airfoils	26
2.4.1 Pitching motion (α).	27
2.4.2 Transverse motion (plunging, y).	29
2.4.3 Transverse/pitching motion (flapping, y, α).	30
2.4.4 Stream-wise motion (in-line, x).	31
2.5 Summary	32

3	Computational Fluid Dynamics model	33
3.1	Set-up	34
3.2	Validation	37
3.2.1	Steady case (airfoil)	37
3.2.2	Unsteady case (cylinder)	38
3.2.3	Sensitivity analysis	40
3.3	Summary	41
4	Case 1: static airfoil	43
4.1	Harmonic forces decomposition	43
4.1.1	Strouhal number	51
4.1.2	Mean and fluctuating loads	51
4.2	Summary	56
5	Case 2: 1-DOF moving airfoil	59
5.1	Pitching oscillation motion	61
5.1.1	Synchronisation at fixed pitching amplitude	62
5.1.2	Pitching amplitude effect	67
5.2	Stream-wise oscillation motion	68
5.2.1	Synchronisation at fixed stream-wise amplitude	69
5.2.2	Stream-wise amplitude effect	74
5.3	Transverse oscillation motion	78
5.3.1	Synchronisation at fixed transverse amplitude	78
5.3.2	Transverse amplitude effect	88
5.4	Summary	89
6	Lumped parameter model	93
6.1	Implementation	94
6.1.1	Set-up	94
6.1.2	Verification	94
6.2	Pitching motion VIV model	97
6.2.1	Results	97
6.3	Transverse motion VIV model	101

6.3.1	Results	102
6.4	Summary	104
7	Case 3: 2-DOF moving airfoil	107
7.1	Coupled stream-wise/transverse motion	108
7.2	Coupled stream-wise/pitching motion	118
7.3	Summary	131
8	Conclusions	133
8.1	Future Work	134
	Bibliography	137

List of Figures

2.1	Drawings of water flow behind obstacles by Leonardo Da Vinci.	10
2.2	Schematic of an asymmetric vortex street.	10
2.3	Flow visualization of atmospheric vortex shedding.	11
2.4	Structural failures due to flow-structure interaction.	11
2.5	Oscillating forces acting on a cylinder due to vortex shedding.	13
2.6	Regime of fluid flow across smooth cylinders [32].	14
2.7	Instantaneous vorticity contours around rectangular cross-sections.	16
2.8	Schematic of a 2-D airfoil degrees of freedom. The airfoil is the NREL S809.	27
3.1	VIV models classification	34
3.2	Flow field domain: dimensions and boundary conditions.	35
3.3	Fluid domain grid.	36
3.4	Steady aerodynamic force coefficients for the NREL S809 airfoil at $Re = 10^6$ against angle of attack: comparison between experiments and CFD results.	38
3.5	Instantaneous vorticity magnitude for a cylinder.	40
4.1	Schematic of the NREL S809 airfoil for positive angles of attack.	44
4.2	Instantaneous vorticity magnitude, no periodic vortex shedding.	47
4.3	Instantaneous vorticity magnitude at $\alpha = 50^\circ$, $t=10s$	48
4.4	Time record of the aerodynamic force coefficients at $\alpha = 50^\circ$	48
4.5	Detail of the time record of the aerodynamic force coefficients at $\alpha = 50^\circ$	49
4.6	Detail of the time record of the aerodynamic force coefficients at $\alpha = 40^\circ$	49
4.7	Instantaneous vorticity magnitude at different incidences, $t = 10s$	50
4.8	Strouhal number against angle of attack with different characteristic length.	52
4.9	Mean forces component coefficients against angle of attack.	53

4.10	Lift force component coefficients against angle of attack.	54
4.11	Drag force component coefficients against angle of attack.	55
4.12	Moment component coefficients against angle of attack.	55
4.13	Relative phase of dominant harmonic.	56
5.1	Detail of the time record of the lift force coefficient for pitching motion at $\alpha_{mean} = 140^\circ$	63
5.2	Spectrum of the lift force coefficient for pitching motion at $\alpha_{mean} = 140^\circ$	64
5.3	Synchronisation map for pitching motion at $\alpha_{ampl} = 7^\circ$	64
5.4	Instantaneous vorticity field for pitching motion at different conditions.	66
5.5	Instantaneous horizontal velocity, pitching motion.	67
5.6	Synchronisation region for pitching amplitude effect.	68
5.7	Flow field domain for translational motion.	69
5.8	Detail of the time record and spectrum of the lift force coefficient for stream-wise motion at $\alpha_{mean} = 140^\circ$	71
5.9	Instantaneous vorticity field for stream-wise motion at different conditions.	72
5.10	Synchronisation map for stream-wise motion at $A_s = 0.25c$	74
5.11	Proposed synchronisation boundaries for stream-wise motion amplitude effect.	76
5.12	Close-up of the instantaneous vorticity field, stream-wise amplitude effect comparison.	77
5.13	Detail of the time record and spectrum of the lift force coefficient for transverse motion.	80
5.14	Instantaneous vorticity field for transverse motion at different conditions.	82
5.15	Close-up of the instantaneous vorticity field, transverse motion; lock-in condition.	83
5.16	Synchronisation map for transverse motion at $A_t = 0.25c$	84
5.17	Close-up of the instantaneous vorticity field, transverse motion; “transitional behaviour” condition.	85
5.18	Close-up of the instantaneous pressure field, transverse motion; “transitional behaviour” condition.	86

5.19	Portion of the time history used in Figs.5.17 and 5.18.	87
5.20	Proposed synchronisation boundaries for transverse motion amplitude effect.	89
6.1	Comparison of predicted lock-in boundaries for a cylinder.	96
6.2	Sensitivity of the VIV model of a cylinder to parameter values.	96
6.3	Detail of the time record and spectrum of the wake variable, q	99
6.4	Variation of the coupling factor, A , for pitching motion.	100
6.5	Proposed synchronization boundaries for pitching motion; VIV model.	100
6.6	Proposed synchronization boundaries for pitching motion effect; VIV model.	101
6.7	Variation of the coupling factor, A , for transverse motion.	103
6.8	Proposed synchronization boundaries for transverse motion; VIV model.	103
6.9	Proposed synchronization boundaries for transverse amplitude effect; VIV model.	104
7.1	Trajectories for the coupled stream-wise/transverse motion.	110
7.2	Synchronisation map for the coupled stream-wise/transverse motion.	113
7.3	Instantaneous vorticity field for the coupled stream-wise/transverse motion.	114
7.4	Close-up of the instantaneous vorticity field for coupled stream-wise/transverse motion over an oscillation cycle; lock-in conditions.	115
7.5	Close-up of the instantaneous vorticity field for coupled stream-wise/transverse motion over an oscillation cycle; lock-out condition.	116
7.6	Portion of the time history used in Fig. 7.5.	117
7.7	Trajectories for the coupled stream-wise/pitching motion.	120
7.8	Synchronisation map for the coupled stream-wise/pitching motion.	122
7.9	Instantaneous vorticity field for the coupled stream-wise/pitching motion.	123
7.10	Detail of the time record and spectrum of the lift force coefficient for the coupled stream-wise/pitching motion.	124
7.11	Close-up of the instantaneous vorticity field for the coupled stream-wise/pitching motion; lock-in condition.	126
7.12	Close-up of the instantaneous vorticity field for the coupled stream-wise/pitching motion; lock-out condition.	127

7.13 Close-up of the instantaneous vorticity field for the coupled stream-wise/pitching motion; pseudo-lock-in condition. 128

7.14 Close-up of the instantaneous vorticity field for the coupled stream-wise/pitching motion; pseudo-lock-in condition. 129

7.15 Portion of the time history used in Figs. 7.12, 7.13 and 7.14. 130

7.16 Vorticity record along a horizontal line probe. 131

List of Tables

2.1	Comparison between free and forced vibration.	22
3.1	Inlet flow properties.	35
3.2	Smooth cylinder test validation with experiments data [104].	39
3.3	Grid sensitivity analysis.	40
3.4	Time-step sensitivity analysis.	41
7.1	Combinations of motion amplitude and phase for the coupled stream-wise/transverse motion.	109
7.2	Trajectories followed by the airfoil for the coupled stream-wise/transverse motion.	109
7.3	Combinations of motion amplitudes and phase for the coupled stream-wise/pitching motion.	119
7.4	Trajectories followed by the airfoil for the coupled stream-wise/pitching motion.	119

Chapter 1

Introduction

Wind energy has been used for thousands of years, mainly for sailing ship propulsion and for driving windmills to grind grain or to pump water. The use of windmills to generate electricity can be traced back to the late nineteenth century with the 12 kW windmill generator constructed by Brush in the USA and the research undertaken by LaCour in Denmark [1]. Hence, the windmills turned into wind turbines as the rotor was connected to an electric generator. Wind turbines started to be developed in the then USSR, USA, Europe. In the mid 1950's Johannes Juul introduced in Denmark what was later called the Danish concept by constructing the *Gedser* turbine, which had an upwind three-bladed stall-regulated rotor (an extensive review of the wind turbines history and development is given by Spera [2]). However, for much of the twentieth century there was little interest in using wind energy. An important event for wind energy development was the oil crisis in 1973. As a consequence, wind turbines became suddenly interesting again for many countries that wanted to be less dependent on oil imports, and many national research programs were initiated to investigate the possibilities of utilising wind energy [1]. The growth in wind turbines installation was remarkable: as stated in the Statistical Review of World Energy 2013 [3], in 2012 there were a total of 284 GW of wind generating capacity installed globally. Nowadays, the main driver for the use of wind turbines to generate electrical power is the very low CO₂ emissions and the potential of wind energy to help limit climate change. In fact, throughout the world, national and regional policies designed to encourage the decarbonisation of the electricity supply, while also reducing dependency on energy imports, are encouraging the continuing rapid expansion of the wind generation sector [4].

1.1 Context

The majority of the machines installed are horizontal axis design (HAWT). As with any technology that harvests ambient energy, wind turbines must be permanently exposed to environmental extremes. This coupled with the proportionately very large upfront capital cost [5], means that design for long term survival is a priority.

As a result, the minimum design requirement for wind turbines as defined by the IEC Standard [6] include specifications for extreme wind loading conditions (see section 6.3 of the Standard). For example, the structure must be designed to withstand steady, turbulent and deterministic gusts which occur on average only every 50 years (i.e. a 50 year return period). As part of the transient wind (i.e. gust) environment a sudden change of wind direction of up to 180° must be considered. Consider a turbine blade, which will either have been feathered towards the prevailing mean wind in severe wind conditions, or will be at a low angle of attack relative to the local flow direction in operational conditions. In the extreme change of direction scenario, the blade will be suddenly inclined at high angle of attack to the local flow. Hence the section will behave more like a bluff body than a streamlined airfoil. In addition, complications may occur under parked conditions (e.g. yaw mode). The design standard only requires calculation of ultimate loads, rather than fatigue loads in scenarios with extreme change of direction (see section 7 of the Standard [6]). However, in these cases the blades will act as bluff bodies, and so the vortex shedding phenomenon might occur, inducing periodic loads on the blades. This could cause harmful and unwanted vortex-induced vibrations, which may lead to damage or even catastrophic failure due to increased fatigue. Therefore, the ultimate load (stress) assessment requires a dynamic analysis.

Vortex-induced vibration of wind turbines is a relatively new subject of research, and no real practical issues has been officially reported. Flow-structure interaction in wind turbines has been studied for almost two decades. In wind turbines two main aeroelastic instabilities can occur, stall flutter (or stall-induced vibrations by extension) and classical flutter, provided that the net damping of the flow-structure system (sum of the aerodynamic and structural damping) becomes negative. As a consequence, energy is transferred from the flow to the structure, and large self-excited oscillations take place

leading to significant failures.

The first problem, stall-induced vibrations, started to appear on stall-regulated wind turbines in the early 1990's when their size became significant, reaching a rated power of 500kW. The turning point was the advent of new composite materials due to demand for lighter blades, which led also to a reduced structural damping [7]. Less structural damping meant that the structure was more prone to experience an aeroelastic instability. Since then, the possible aeroelastic instabilities coming from the interaction between unsteady aerodynamic forces and long slender flexible blades has become a key factor in modern wind turbines design. Dedicated aeroelastic models have been developed (see Hansen & Madsen [8] for an exhaustive review). Nonetheless, engineering-type empirical models lack accuracy in describing the real physics of the system due to their simplified aerodynamic modelling (e.g. BEM, Blade Element Momentum). Furthermore, if the flow is fully separated from the blades the high non-linearity of the fluid mechanics makes the problem even more complicated. Therefore, a CFD (Computational Fluid Dynamics) approach has been used for this work, which would offer a more appropriate modelling of the system, by means of a commercial Navier-Stokes solver (ANSYS Fluent[®]). The URANS (Unsteady Reynolds Averaged Navier-Stokes) method has been chosen for practical reasons of time and resources. It is known that a LES (Large Eddy Simulation) approach, extremely computationally expensive in comparison, is more suitable for detached flow simulations, as the standard URANS is not sufficient to capture correctly the flow unsteadiness (see e.g. [9, 10]). Also a DES (Detached Eddy Simulation) approach would be more appropriate, less computationally expensive than LES but still far more computationally expensive than URANS [11]. Nonetheless, the URANS approach seems to be the most reasonable way to simulate unsteady flows around moving airfoils at high Reynolds ($Re = 10^6$ and more) [9]. Giving the amount of time available for this work, the rationale in the choice of the method is that it has been preferred to conduct an extensive, yet approximate, parametric study with URANS rather than few highly detailed cases with LES (or DES). The purpose is to capture the basic principles of the flow behaviour and try to give a physical explanation, rather than to obtain highly detailed results.

Concerning the computational time issue, another substantial choice has been done: a 2-D approach over a more realistic 3-D. The behaviour of the aerodynamic loads on

a bluff body has been observed to be “less 3-D” as soon as lock-in occurs; hence, the span-wise loads correlation is stronger (see e.g. [12]). Moreover, results from a numerical study on vortex shedding of a 3-D airfoil at $\alpha = 60^\circ$ conducted by Elakoury *et al.* [10] show a strong span-wise vortex shedding coherence. These considerations lend credibility to the choice of the 2-D approach as a preliminary investigation.

Similarities could be seen between stall-induced vibrations and vortex-induced vibrations. This, enhanced by the fact that the wind turbines rotor size is bound to increase even more in the near future (i.e. longer and more flexible blades), brings the attention to the potential hazard caused by vortex-induced vibrations. Hence the interest on this topic for the present research work.

1.2 Objectives and Overview

Although there has been a considerable research effort in the area of unsteady flow around airfoils, generally the focus has been more on aerolasticity rather than vortex-induced vibration. In this work the focus is on vortex shedding and its related lock-in phenomenon which may originate from the interaction between the fluctuating fluid loads caused by the shed vortices and the structure motion. For a certain range of structural motion frequency, the frequency of the vortex shedding will be synchronised with the frequency of the structure motion, giving rise to a resonance condition which would lead to a growth in vibration amplitude.

The ultimate goal, is to obtain a lock-in map/set of data of the NREL S809 airfoil for the three single degree of freedom prescribed motions (i.e. pitching, stream-wise, transverse) at different angles of attack and motion amplitudes, which may be used to build a system identification model of vortex-induced vibrations. In addition, two couplings of these motions will be considered (stream-wise/transverse, stream-wise/pitching) for two sample angles of attack.

This work will concentrate on:

- unsteady analysis of vortex shedding of the static NREL S809 airfoil at high angles of attack, in order to obtain the Strouhal number variation with angles of attack. An emphasis has been given to the higher harmonics behaviour of the aerodynamic

forces and moment with angles of attack;

- unsteady analysis of vortex shedding of the oscillating NREL S809 airfoil with pure sinusoidal prescribed motion, at high mean angles of attack. Three types of motion are considered: pitching, stream-wise, transverse. The main purpose is to obtain the synchronisation boundaries for different angles of attack, motion frequencies and motion amplitudes;
- unsteady analysis of vortex shedding of the oscillating NREL S809 airfoil with coupled two degrees of freedom motion (stream-wise/transverse, stream-wise/pitching). The main purpose is to assess in which conditions the stream-wise motion prevents the pitching and transverse motion to lock-in.

The interest of this research is not to investigate the fluidelastic instability of the airfoil, but rather the fluid-structure interaction and vortex shedding lock-in behavior. The choice to work with forced motion instead of studying a free vibrating system is that at lock-in condition, the damping is zero. Therefore a long transient simulation would be needed to resolve a light damped model. Furthermore, for a free vibrating system a damping parameter would be introduced, which would affect the motion amplitude. A forced vibrating system instead allows to have an explicit control on the motion amplitude.

The present research work aims to investigate the susceptibility of a wind turbine blade section to experience frequency lock-in due to vortex shedding. This work cannot be directly applied to the wind turbine industry. This work wants to be an initial step to fill a gap present in the literature on vortex shedding of wind turbine blade sections at high angles of attack, towards a study on 3-D/Reynolds number/blade taper effects, among others.

Chapter 2 reviews the literature on vortex shedding of bluff bodies and airfoils. Chapter 3 presents the CFD model used throughout this work. Chapter 4 presents the vortex shedding results of the static airfoil. In Chapter 5 the three single degree of freedom motions are analysed. In Chapter 6 a lumped parameter model for VIV of airfoils, based on the wake oscillator model, is proposed for two 1-degree of freedom VIV of airfoils in pitching and transverse oscillation. In Chapter 7 two 2-degrees of freedom couplings

are presented (stream-wise/transverse and stream-wise/pitching). Finally, in Chapter 8 conclusions and considerations are drawn, and avenues for future work are advanced.

In this work it has been found that airfoils at high angles of attack can suffer vortex shedding lock-in. The vortex shedding lock-in behavior is strongly dependent on the type of motion, in particular the stream-wise motion is the least likely to synchronise. In addition, the angle of attack strongly affects the extent of the frequency ratio at which synchronisation occurs.

1.3 Publications

A part of the work presented in this thesis has been (or is being) disseminated through the following publications:

- Pellegrino, A., Meskell, C., Vortex shedding from a wind turbine blade section at high angles of attack. *Journal of Wind Engineering and Industrial Aerodynamic*, 121:131-137, 2013.
- Pellegrino, A., Meskell, C., Vortex shedding lock-in due to pitching oscillation of a wind turbine blade section at high angles of attack. *Journal of Fluids and Structures*. Submitted 2014, in process.
- Pellegrino, A., Meskell, C., Vortex shedding lock-in due to stream-wise oscillation of a 2-D wind turbine blade section at high angles of attack. *ASME, Pressure Vessels & Piping Conference - PVP 2014, Anaheim, California, USA*.
- Pellegrino, A., Meskell, C., Vortex shedding for a pitching wind turbine blade section at high angles of attack. *In 12th Americas Conference on Wind Engineering 12ACWE, 2013. Seattle, Washington, USA*.
- Pellegrino, A., Meskell, C., Analysis of vortex shedding from a wind turbine blade at high angle of attack. *In 10th International Conference on Flow-Induced Vibration - FIV2012, 2012. Dublin, Ireland*.

Chapter 2

Literature Review

For structures placed in the path of a flowing fluid, the interaction of fluid & structure plays a very important role in their operational behaviour as the flow field is altered due to the presence of the structure. The fluid flow and the structure are coupled through the forces exerted on the structure by the flow: *flow-induced vibrations* (FIV) describe the interaction that occurs between the fluid dynamic forces and the structure inertial, damping, and elastic forces. The fluid forces cause the structure to deform/move, which consequently changes its orientation to the flow: the flow-field has thus been affected. The structural deformation/motion will induce additional fluid forces which may produce an additional change in the system, which may again induce additional fluid forces and so on.

Flow-induced vibrations can be classified according to different criteria. Two widely used classifications of FIV were proposed by Naudascher & Rockwell [13,14] and by Weaver [15], based respectively on the source of excitation and the nature of vibrations.

Naudascher classifies FIV as:

- Extraneously induced excitation (EIE), which are caused by fluctuation in the incoming flow.
- Instability induced excitation (IIE), which are associated with a flow instability and involves local flow oscillations.
- Movement induced excitation (MIE), which are fluctuating forces arisen from movements of the body.

Weaver instead classifies FIV as:

- Forced vibrations induced by turbulence (turbulent buffeting).
- Self-controlled vibrations (flow periodicity, e.g. *vortex shedding*).
- Self-excited vibrations (fluidelastic instabilities, e.g. flutter or galloping).

Thorough reviews of flow-induced vibrations generally can be also found in books by Paidoussis *et al.* [16] and by Blevins [17], among others.

This Chapter reviews the work on vortex shedding of bluff bodies as well as of moving airfoils present in the literature. In Section 2.1 a generic overview of vortex shedding of most common shapes (cylindrical and prismatic) is presented. Vortex shedding of static airfoils is reviewed in Section 2.2. Frequency lock-in is presented generally in Section 2.3 with an overview on translational motions. Section 2.4 reviews the work done on oscillating airfoils (rotational and translational motion).

2.1 Vortex shedding

The problem of a bluff body in cross flow is well known and widely studied, but still is a challenge for researchers after over a century of effort. A bluff body behaves in the opposite way to a streamlined body (airfoil), i.e. the pressure drag contribution dominates over the skin friction. The complexity of bluff body flow is well known, since it may change its behaviour from a quasi-steady to an unsteady regime. A review on this problem is presented by Roshko [18] who states that the features that characterise a bluff body in aerodynamics are a large region of separated flow, a high value of the drag coefficient and the phenomenon of vortex shedding. On his first experiments in the mid 1950's, Roshko observed that as a body becomes "more bluff" (in the sense that the created cross-flow obstruction becomes more significant) the recirculation region becomes larger and the shedding frequency decreases. As a general comment, he stated that the problem of bluff body flow remains almost entirely in the empirical, descriptive realm of knowledge.

Vortex shedding happens when the flow separates at two points on the opposite faces of the obstacle, generating opposite sign circulations which in turn give rise to opposing sign

shear layers. If the body is symmetric, these two shear layers are of equal intensity. Behind the body an inherently unstable wake is formed by the coupled interaction of the shear layers, resulting in two staggered rows of counter-rotating vortices moving downstream at the same convective velocity. It is common to express the frequency of periodic vortex shedding, f_v , using a dimensionless quantity, called *Strouhal number*.

Early representations of vortex shedding can be found, back in the 15th century, in drawings by Leonardo da Vinci (Fig. 2.1), and later in Flemish paintings of the 16th century. Early in the last century, first experimental observations were reported by Henri Bénard and Arnulph Mallock. It is in 1912 that an explanation for vortex shedding was advanced by Theodore von Kármán who proposed a model of bluff body wakes at low Reynolds number as an infinite double-row of alternating sign vortices, known as “Kármán vortex street” [19]. In reality this vortex street is not infinite, but it will be dissipated by the flow viscosity.

The structure of the Kármán vortex street is characterised by the convective velocity of the vortices, their circulation, γ , and the transverse-to-streamwise vortex spacing ratio, h/a (shown in Fig. 2.2). von Kármán [19] showed that for two parallel rows of vortices of equal but opposing circulation a stable arrangement of vortices only exists if $h/a = 0.281$. This would imply a universal Strouhal number since the streamwise vortex spacing is the product of the convective velocity and the inverse of shedding frequency. Further studies showed that h/a is obstacle-geometry dependent (e.g. [20]). However, Roshko [21] showed that it was possible to define a wake Strouhal number, which was constant for several obstacle geometries, around a value of 0.2.

Bluff bodies can be natural elements (e.g. mountains or islands) or industrial/civil engineering elements (e.g. tall buildings, bridges, antennae, chimneys, tubes), immersed in flows such as air or water. Figure 2.3 shows a natural flow visualization of atmospheric vortex shedding behind island mountain peaks, resulting in von Kármán vortices shaped clouds.

In industrial/civil engineering elements, the oscillating wake causes periodic forces to be experienced by the body (vibration modes excitation), potentially yielding vortex shedding induced vibration (VIV) which can lead to catastrophic failure. Remarkable incidents due to VIV in civil engineering occurred over the last two centuries. Some of

the major ones are the failure of the Brighton Chain Pier Bridge in 1836; the collapse of the Tacoma Narrow Bridge in 1940 (Fig. 2.4(a)); the collapse of three out of eight cooling towers at Ferrybridge Power Station in 1965 (Fig. 2.4(b)). In particular, the Tacoma Narrow Bridge incident dramatically exemplified the importance of the unsteady loads (caused by unsteady aerodynamics) rather than static loads considered till then [22].

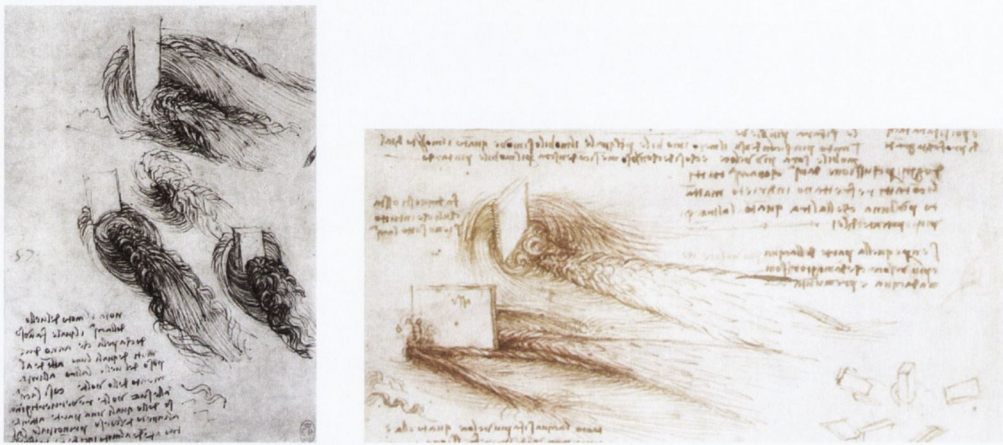


Figure 2.1: Drawings of water flow behind obstacles by Leonardo Da Vinci.

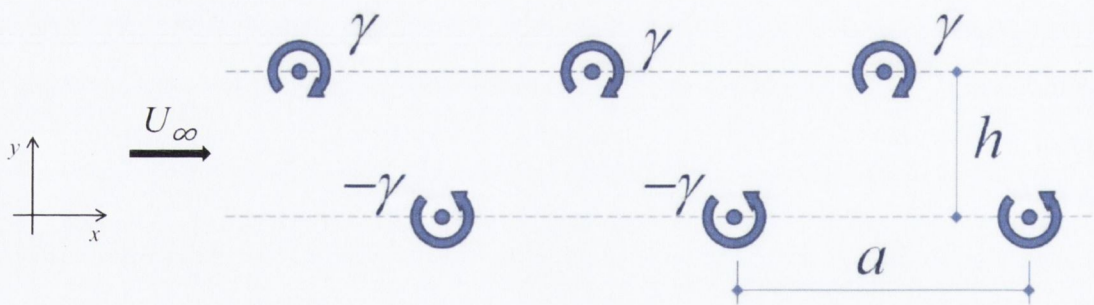
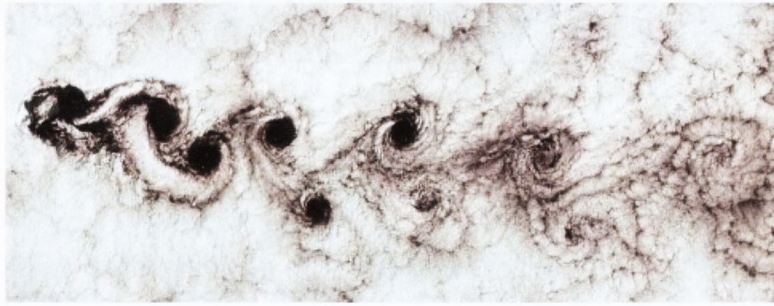


Figure 2.2: Schematic of an asymmetric vortex street of counter-rotating vortices with transverse (h) and streamwise (a) spacing.

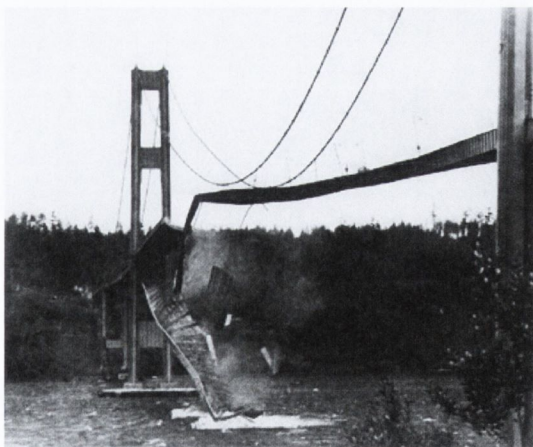


(a) Atmospheric von Kármán vortices over Alexander Selkirk Island, Chile, in the southern Pacific Ocean (NASA *Landsat 7* satellite),



(b) Atmospheric von Kármán vortices over Guadalupe Island.

Figure 2.3: Flow visualization of atmospheric vortex shedding behind islands mountain peaks, resulting in von Kármán vortices shaped clouds.



(a) Tacoma Narrows Bridge, Seattle, USA



(b) Ferrybridge Power Station

Figure 2.4: Structural failures due to flow-structure interaction.

2.1.1 Cylinders.

To date, most of the studies in the literature have been carried out on a cylindrical body due to its simple geometric shape and prevalence in civil and power generation engineering. Extensive reviews of research work with cylinders in steady currents has been presented by King [23], Fung [24], Zdravkovich [25], Williamson [26], among others.

An explanation of vortex formation mechanism related to a cylinder, nowadays still accepted, has been proposed by Gerrard [27]. In his model, the forming vortex will continue to grow as long as it is fed by circulation from the separated shear layer until it is strong enough to draw the shear layer from the opposite side across the wake. The approaching, oppositely signed, vorticity from the other shear layer, with sufficient concentration, will cut off further supply of circulation to the vortex. At that point it sheds and convects downstream, completing half a cycle.

Since a dominant shedding frequency, f_v , exists in the wake, it can be expected to be observed also in load fluctuations. A review on fluctuating loads on a cylinder has been given by Norberg [28]. The loads acting on the structure are normally characterised as *drag* and *lift* forces, respectively in-line and transverse with the flow direction. The fluctuating lift and drag are dominated by the actions from the vortex shedding, and are mainly due to the fluctuating pressures acting on the surface of the cylinder. Figure 2.5 shows a schematic of an asymmetric vortex street behind a cylinder with the resulting induced forces. Spectral analysis of the unsteady fluid force shows that the lift fluctuation energy is concentrated in a band around f_v , whereas the drag fluctuation energy is concentrated in a band around $2f_v$ [29, 30], with harmonics.

The separation points for a cylinder (or rounded bodies in general) move on the surface depending on the flow regime, which is usually expressed by the Reynolds number, a measure of the relation between the inertial and the viscous forces. Small Reynolds number corresponds to slow viscous flow where frictional forces are dominant. When the Reynolds number increases, inertial forces become more significant and velocity variations occur leading to turbulent flow regions. Figure 2.6 shows the effect of Reynolds number values on the flow around a cylinder.

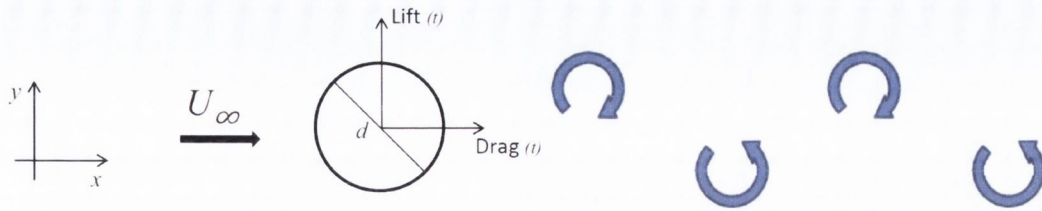


Figure 2.5: Oscillating forces acting on a cylinder due to vortex shedding.

2.1.2 Prismatic bodies.

A prismatic body is another bluff body shape of great interest, especially for its application in civil engineering (tall buildings and bridge decks section in cross flow). The main difference between prisms (or bodies with sharp edges in general) and cylinders (or rounded bodies in general) is that flow separation occurs at the edges, i.e. the position of the separation points is fixed. Most commonly used prismatic shapes are square and rectangular sections.

Other than the Reynolds number, for a prism another significant parameter is the aspect ratio of the section, b/d ; b is the chord length and d is the depth of the section. The drag force, lift force and Strouhal number, which defines the periodicity of the vortex shedding, vary with the b/d ratio. Shimada & Ishihara [31] investigated numerically the aerodynamic characteristics of prisms of infinite length and various b/d ratios (ranging from 0.6 to 8), at zero incidence. They organised these cases into three categories according to their aerodynamic behaviour as the rectangular body becomes more and more elongated: separated flow ($b/d < 2.8$), intermittently reattached flow ($2.8 < b/d < 6$), fully reattached flow ($b/d \geq 6$). For an elongated bluff body, the flow separates at the leading edge and reattaches along the chord of the body before separating once again at the trailing edge. In Fig. 2.7 [31], different flow behaviours around the body as well as the wake structures behind it influenced by the b/d ratio are presented. It can be seen that for $b < d$ the vortices are shed as a pair of vortex rows, whereas when the body becomes more elongated, the wake is organised in a unique vortex row. As the chord length increases further, in the fully reattached flow behaviour, vortex shedding resumes from the trailing edge of the section.

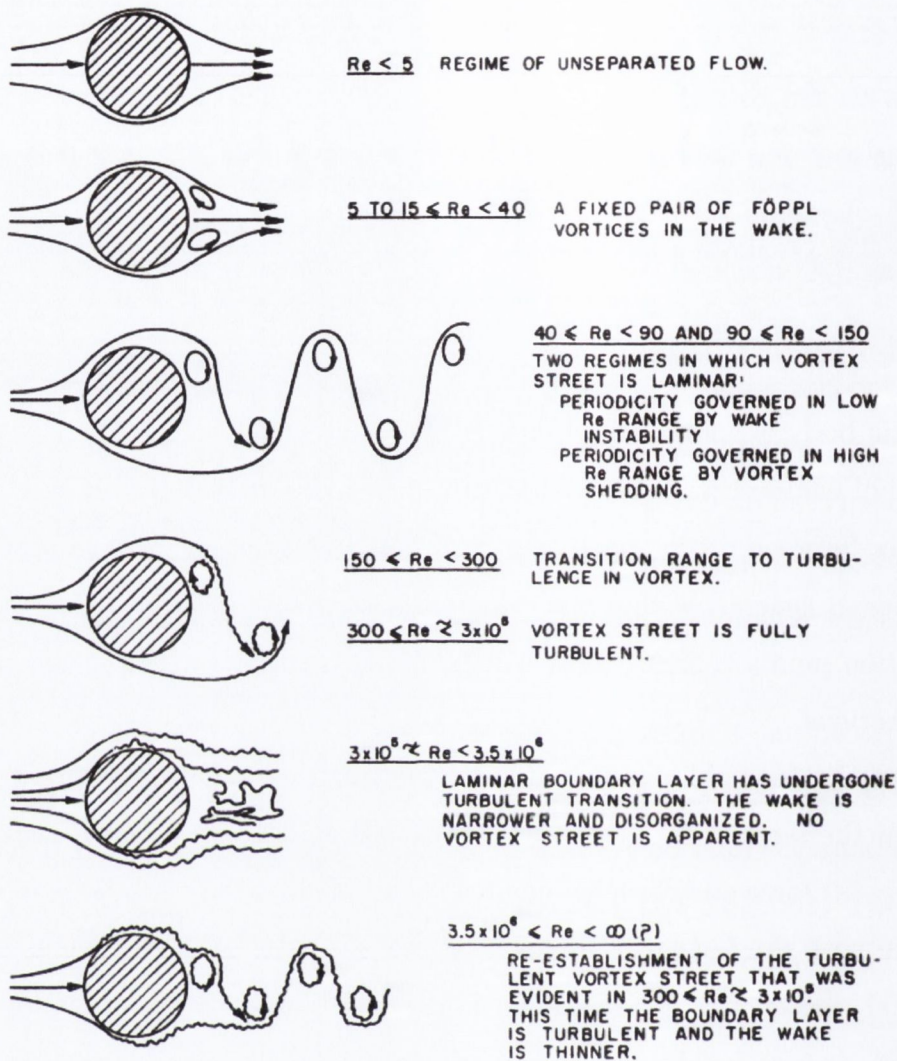


Figure 2.6: Regime of fluid flow across smooth cylinders [32].

It is then well accepted that for an elongated bluff body, the flow separates at the leading edge and reattaches along the chord of the body before separating once again at the trailing edge. The decks of nearly all long-span suspension and cable-stayed bridges can be classified as elongated bluff bodies. The leading edge separating-reattaching flow adds complexity to the case of classical Kármán vortex shedding in the wake of shorter bluff bodies (with no reattachment along the body). Still, for elongated bluff bodies, even if the vortex formation happens at the trailing edges, the importance of the flow at the leading edge is dominant. In fact, in general, previous studies have concluded that changes in the leading edge geometry affect the shedding frequency more significantly than changes to the trailing edge geometry. This will be discussed in more detail in Chapter 5,

in the context of the wind turbine blade geometry. Experiments on the effects of leading edge geometry on the vortex shedding frequency of an elongated bluff body have been conducted by Taylor *et al.* [33]. They observed a vortex shedding frequency decrease with increasing leading edge separation angle. Other experimental and numerical studies on vortex shedding from elongated prisms have been done by Nakamura *et al.* [34], pointing out differences between vortex shedding from bluff shapes and elongated bluff shapes.

Another parameter differentiating prisms from cylinders is the angle of attack. Knisely [35] conducted experiments on vortex shedding for a family of prisms with different b/d ratio (from 0.04 to 1, hence ranging from a thin flat plate to a square section) at different angles of attack (from 0° to 90°) to determine their Strouhal number. It was found a general tendency for a rapid rise in the Strouhal number to occur at relatively small angles of attack, which is associated with reattachment of the separated shear layer. The angle of attack where reattachment and, hence, the rapid rise in Strouhal numbers occurs is dependent on the b/d ratio. As the angle of attack approaches 90° , there is a sudden decline in the value of the Strouhal number, associated with shear layer-corner interaction (i.e. detachment). This aspect can be related to the wake structure (von Kármán h/a). The flow reattachment process causes the reduction of the distance between fixed separation points (h); hence the stream-wise vortex spacing is reduced (a), causing an increase in temporal frequency of vortex shedding. In Chapters 4 and 5 this aspect will be discussed for the presented results.

A square section at incidence of 45° and low Reynolds number ($Re = 200$), effectively in a diamond configuration, has been studied by Leontini & Thompson [36] to investigate the impact of the sharpness of the side corners. It was found that the lift and drag forces are strong functions of the sharpness of these corners. However, the configuration of the wake remains essentially the same in all cases, i.e. a classic Kármán vortex street.

The effect of rounded corners on the Strouhal frequency has been investigated in the past, e.g. by Parker & Welsh [37]. The general tendency is for the Strouhal number to increase with increasing rounding radius. The rate of increase with rounding appears to depend on the after-body length as well.

A triangular section, at different incidences, has been studied experimentally by Csiba *et al.* [38] to investigate the influence of unequal strength opposing shear layers on periodi-

cally shed vortices. Their results suggest that the classical theory based on equal strength shear layers only partially captures the behaviour for shedding with unequal shear layers, and requires further modification.

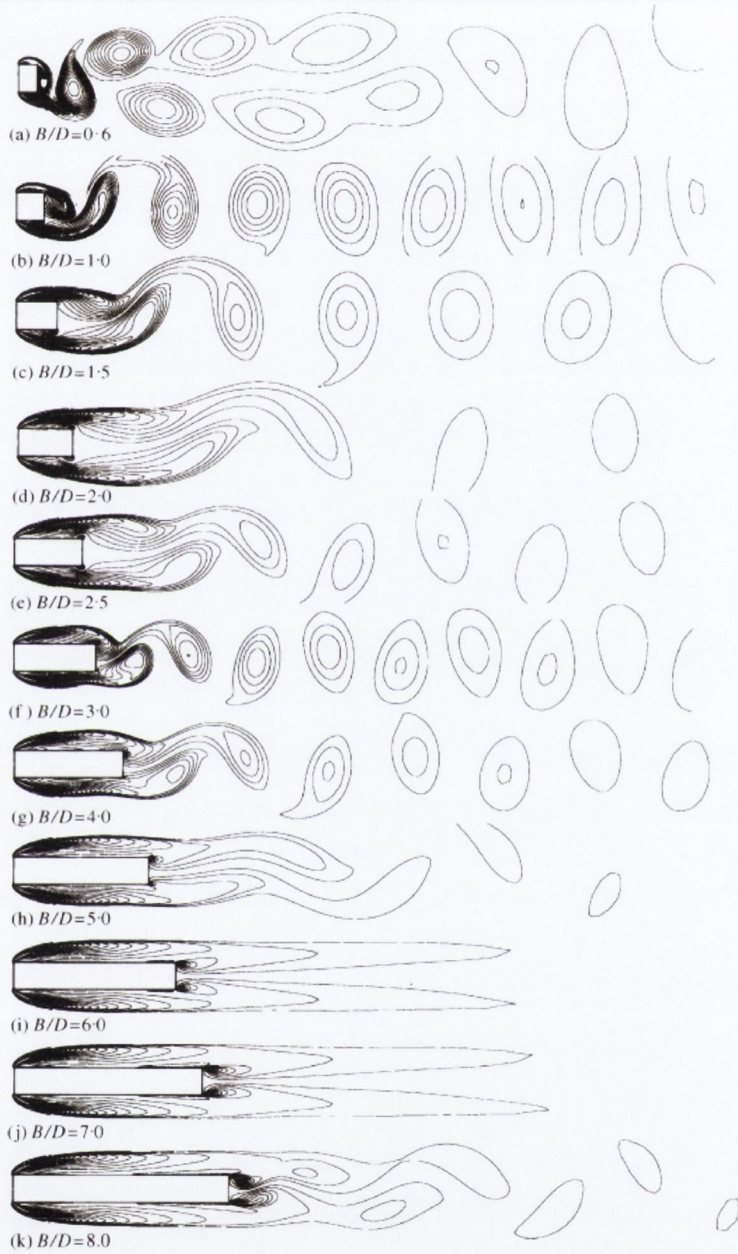


Figure 2.7: Instantaneous vorticity contours around rectangular cross-sections with various b/d ratios at the maximum lift [31].

2.2 Static airfoils

The main focus of this thesis is a wind turbine blade section (airfoil NREL S809). The introduction with circular and prismatic shapes served the purpose to introduce the basic principles of vortex shedding. In fact, while various shapes have been tested, little is known about the response of airfoil sections at very high angles of attack (and even less for high Reynolds numbers). However, similarities between tested shapes and airfoils exist. For example, a D-section resembles a thick airfoil; elliptical sections are close to an airfoil with two rounded edges; flat plates are similar to thin airfoil with two sharp edges. Despite these similarities, airfoils differ from the above shapes in having both a round and sharp edge. Airfoils embed the main properties of both of them (rounded and sharp edge bodies) from a fluid mechanics point of view. That is, a sharp edge means a defined flow separation point, whereas a rounded edge means a “moving” separation point. Therefore, studies on elliptic sections or flat plates are still interesting, since their cross-flow behaviour at high angles of attack can give a good idea of what could happen in the case of airfoils.

2.2.1 Flat plates and elliptic sections.

The earliest work concerning with vortex shedding of sharp-edged structures was that of Fage & Johansen in 1927 [20], dealing with an infinitely long flat static plate at incidence. They found that the vortices generated at each edge passed downstream with a shedding frequency which increased as the inclination of the plate decreased (starting from a position perpendicular to the incoming flow). As a consequence of that, the longitudinal spacing of the vortices decreased. They also noticed that vorticity was shed from the two edges of the plate at the same rate, which falls slowly as the inclination is decreased. It is important to point out that they used two Strouhal number normalisations, both the actual width (say d) and the windward width ($d' = d \sin \alpha$) of the plate, showing that the vortex shedding frequency scales with the projection of the plate width normal to the free-stream direction.

Other experiments on a static flat plate at high angle of attack (precisely at 45°) have been conducted by Perry & Steiner [39]: the flow field immediately behind the plate

was shown to be highly asymmetric. The results revealed the dynamics of the vortices rolled up from the leading and trailing edges of the inclined plate: the vortex rolled up from the leading edge was found to remain attached to the rear of the plate for a longer period of time than the trailing edge vortex. In addition, what they found suggested that vortices shed from the trailing edge and the leading edge seem to be of unequal strength. This aspect was confirmed by other studies. The flat plate case studied by Knisely [35] within his investigation on rectangular shapes revealed that the vortex from the trailing edge dominates the wake of the inclined plate. Lam [40] investigated the flow past an inclined flat plate at ($\alpha = 30^\circ$), showing that the train of trailing edge vortices have higher vortex strength than the train detached from the leading edge vortices. More recently, Lam & Leung [41] investigated the vortex shedding wake behind a long flat plate inclined at moderate high angles of attack ($\alpha = 20^\circ, 25^\circ$ and 30°) to confirm through detailed experiments the above mentioned wake asymmetry. When compared at the same stream-wise locations, the trailing edge vortex in the separated wake always possesses more intense vorticity levels but a smaller spatial extent of fluid circulation than the leading edge vortex. Moreover, they believe this different vortex strength to cause the observed different mechanisms of the two vortices trains formation.

Breuer *et al.* [42] conducted numerical studies on the separated turbulent flow past an inclined flat plate (with sharp edges) at moderate incidence ($\alpha = 18^\circ$) and Reynolds number ($Re = 20000$). The purpose of this investigation was to compare different CFD techniques and approaches: RANS (combined with a one-equation Spalart-Allmaras turbulence model), LES and DES. As they expected, the unsteady RANS approach failed to predict the unsteady characteristics of the separated flow. In contrast, the DES approach yielded reasonably the shedding phenomenon and some integral parameters. However, remarkable deviations were observed between the DES and LES predictions when the same grid resolution was applied. In addition, results showed once again that the wake is strongly dominated by the trailing edge vortices.

Regarding elliptic sections, work has been done by Nair & Sengupta [43, 44]. Among other things, they present the flow around an elliptic prism at high angle of attack and moderate Reynolds numbers, finding that the frequency of vortices in the wake is a function of the angle of attack and the type of bubble formation.

2.2.2 Wind turbine blades.

Medici & Alfredsson [45] conducted experiments on the vortex shedding of a scaled two-bladed wind turbine model. They found that the measured Strouhal number value, $St \approx 0.12$, from the rotor disc is comparable with that reported for a solid disc. It is worth noting that this Strouhal number is also consistent with slender structural components at high angles of attack [46]. In addition, if the turbine is yawed (i.e. rotated with respect to the axis vertical-to-the-ground), the wake rotates in the opposite direction, with a consequent change in vortex shedding frequency (and therefore in loads on the turbine). It may then be inferred that the rotor disk orientation could be an issue for yawed-controlled turbines at standstill or operating in wind parks as the vortex shedding frequency may be more variable due to the wake's motion.

The standstill condition of the NREL Phase-VI blade at a tip angle of attack $\alpha = 90^\circ$ has been simulated using CFD by Sørensen *et al.* in the project KNOW-BLADE [47]. The aim was to improve the knowledge about rotor standstill for parked conditions, since very little data exist for airfoils at very high angles of attack (above $\alpha = 40^\circ$). Also, a RANS/DES approach comparison was performed: it was shown that the DES methodology provides a more physical representation of the heavily stalled part of the flow over the blade at high angles of attack. Precisely, looking at the vortex pattern behind the blade, a distinct difference between the RANS and DES results has been observed: the wake computed with the RANS model forms a few large-scale structures while the DES simulation predicts a variety of scales in the wake. It must be noted though, that RANS methodology (as well as DES) was capable to predict the forces on the blade within 20% along the total blade.

A work on a wind turbine blade section (DU96-W-180) at $\alpha = 90^\circ$ has been done by Skrzypiński *et al.* [48]. Among other things, their CFD 2-D computations returned a Strouhal number value of 0.13, while a value of 0.16 was obtained from 3-D computations. Most importantly, they flag that 2-D computations made on the airfoil Risø A1-21 returned the same Strouhal number value as that of the DU96-W-180 profile. Hence, they comment that this similarity is indicative that at high angles of attack, i.e. where the flow separation is well defined and established, the Strouhal number is relatively independent

of the airfoil shape.

2.3 Frequency lock-in

Vortex shedding induced vibration (VIV) can be a problem for a wide range of structures exposed to a cross flow since the resulting vibration amplitudes can lead to damage due to fatigue/fretting wear, and even to catastrophic failure in extreme cases. In particular, VIV can be expected in flexible slender bodies of any cross-section, and therefore this field is still an active area of research, in a wide range of engineering fields of interest such as civil constructions (bridge decks, bridge suspension cables, tall buildings) and industrial applications (heat-exchanger tube arrays in nuclear plants, ocean riser pipes, tall chimneys, marine piles). As the size of commercial wind turbines has increased dramatically in the last three decades (from a rated power of 50 kW with rotors of 10-15m diameter up to 6MW machines with a rotor of 150m), the flexibility of the blade has increased as well. Although to date no explicit VIV issues on wind turbines have been registered, wind turbine blades may be prone to VIV in certain conditions. This will be especially true for off-shore wind turbines at standstill, due to more severe atmospheric conditions (stronger wind loads, storms). In addition, off-shore machines are planned to be bigger than on-shore ones (i.e. longer and more slender blades), but with a smaller maintenance window, which means more stringent design/safety requirements. It is worth noting that such structure dimension and wind velocity will lead to high Reynolds numbers (of the order of 10^6 and more).

The literature is rich in comprehensive reviews on VIV, e.g. by Williamson & Govardhan [49, 50] and Sarpkaya [51]. For high Reynolds numbers, the effect of viscosity is dominant only at a very small scale near the boundary, and the high level of vorticity is not dissipated in the vicinity of the body. Hence the flow profile downstream shows two shear layers. As presented in Section 2.1, these two shear layers of opposite vorticity are produced by the two edges of the body, interacting in a coupled instability. The resulting effect is the creation of alternating vortices (vortex shedding), defining a self sustained oscillation with a very well defined dominant vortex shedding frequency, f_v . As fluctuations of vorticity develop in the unstable wake, fluctuating forces and moment result on

the body.

One of the most interesting phenomenon in VIV is the so called “lock-in” between the vortex shedding and vibration frequencies [51]. Lock-in is a resonance phenomenon that occurs when the vortex shedding frequency of an elastic bluff body is close to its structure natural frequency. The vortex shedding frequency diverges from that corresponding to a fixed body (static case) and becomes equal to the frequency of the body’s oscillation. This locking-in of the vortex shedding frequency to the body’s motion frequency can occur over a range of flow speeds dependent on the oscillation amplitude and Reynolds number. The amplification of motion at lock-in condition observed in experiments can be understood as the consequence of a non-linear coupling between the structural motion and the fluid wake in which additional energy is extracted from the flow. It is important to note that the lock-in condition causes the vortex shedding to be almost perfectly correlated across the span, which in turn causes the amplitude of vibration to increase [52]. In general for industrial and civil engineering structures, this condition must be avoided keeping the structural natural frequency value well distinct from the expected vortex shedding frequency one.

A body’s vibration can be free or forced, also referred to as prescribed motion. These two vibration types lead to different flow behaviour, well summarised by Konstantinidis [53] and reported in Tab. 2.1. Most of all, he points out the difference between frequency lock-in and frequency synchronisation (or lock-on). Lock-in means that the vortex shedding frequency changes itself to adapt with the oscillation frequency, and belongs to the “free vibrations” branch. Synchronisation instead, means that the vortex shedding frequency coincides with the prescribed oscillation frequency, and belongs to the “forced excitation” branch.

Free vibrations	Forced excitation
Self-excited/self-sustained oscillations	Oscillations controlled externally
2-way coupling fluid-structure	1-way coupling (no feedback)
Energy transfer only from fluid to structure	2-way energy transfer fluid - structure
3 main frequencies involved (at least): f_n (input), f (output), f_v (output)	2 main frequencies involved: f_{ex} (input), f_v (output)
LOCK-IN	SYNCHRONISATION (or LOCK-ON)

Table 2.1: Difference between free and forced vibration. f_n is the structure natural frequency, f is the free oscillation frequency, f_v is the vortex shedding frequency, f_{ex} is the excitation frequency.

The canonical lock-in problem is an elastically mounted cylinder constrained to move in the transverse direction to the free-stream. For a given natural frequency, the “lock-in range” indicates the range of flow velocities over which the vortex shedding frequency is sufficiently close to the structural frequency for lock-in to occur. It is well known that the response varies with the body shape. In this regard, extremely important was the contribution of Blevins [17] who noted a decrease in response amplitude for cylinders with sharp edges.

VIV for cylinders have been largely studied experimentally. The development of numerical methods for VIV is still a challenge for researchers. One of these proposed engineering models is the wake oscillator model (to be coupled with a structure model for fully coupled systems), which will be introduced in Chapter 6.

As a general remark on VIV, it is important to note that this phenomenon can be used also in a positive fashion. That is, as a new concept for generation of clean and renewable energy from ocean/river currents. An example of such a device to harvest energy, named VIVACE, has been introduced by Bernitsas *et al.* [54]. This energy converter design is based on the idea of enhancing rather than spoiling vortex shedding, and maximizing under significant damping rather than suppressing VIV (opposite of what usually engineers try to do to prevent damage to equipment and structures).

2.3.1 Transverse motion (heave, y).

As mentioned above, vortex shedding can be dramatically changed when a structure oscillates in a flow stream, in the cross-flow and in the stream-wise direction.

In the 1960's Bishop & Hassan [55] pioneered the research of transverse VIV with experiments on cylinders subjected to forced cross-flow oscillations in uniform flow. Their experiments revealed the magnification of the mean drag and lift amplitudes when the excitation frequency is close to the natural shedding frequency. In addition, they observed a sudden change in the phase angle between the lift force and cylinder displacement when the oscillation frequency is varied around the shedding frequency. Many other studies on oscillating cylinder lock-in by different researchers followed, e.g. by Stansby [52] who considered both uniform and shear flows. One of the most notable is Feng [56] who made one of the more widely known contributions to cylinders VIV. He also tested vortex shedding of a D-section.

Williamson & Roshko [57] conducted experiments at which the period of forced oscillation was varied up to three times the period of natural shedding and the amplitude up to five cylinder diameters. They observed a series of vortex shedding patterns in the synchronisation region, which they classified in terms of the number of vortices shed per oscillation cycle. One of the most interesting results of this research is that, for given oscillation and flow conditions, the vortex pattern deviates from that according to which two vortices are shed per oscillation cycle ("2S" mode) and takes the more complicated form at which two pairs of vortices are shed per oscillation cycle ("2P" mode). With this observation, they tried to explain the phase jump near resonance (observed earlier by Bishop & Hassan [55]) attributing it to the sudden transition between 2S and 2P modes. They also showed that variations between the 2S and 2P wake cycles are the cause of hysteretic response.

Transverse VIV of cylinder is widely studied in ocean engineering for marine risers/pipes (long, flexible cylinders). Their peculiarity is to be immersed in deep water. Hence they are subjected to shear and oscillatory cross-flow as well as in-line flow, meaning that they may be excited in multiple and higher modes. Experiments have been conducted by Trim *et al.* [58] who have shown that in-line fatigue damage is as severe as

cross-flow fatigue damage, for bare risers, although industry analysis approaches generally ignore in-line damage due to VIV. Helical strikes coverage decreases the in-line damage level relative to the cross-flow one. CFD simulations have been performed by Chen & Kim [59] and by Williden & Graham [60]. The latter reported that the shear stress contributions to the transverse force acting on the body are very significant, and that the free transverse vibrations exhibited significant spanwise correlation over a large length of the body despite the sheared flow.

Transverse VIV of prisms is taken into account for civil engineering constructions, such as tall buildings and bridges. Kawai [61] investigated experimentally the effect of turbulence on the VIV from a prism, finding that the vibration strengthens as the turbulent intensity increases. Leontini & Thompson [36] studied a diamond section free to oscillate, undergoing VIV. They showed that the flow response is markedly more varied than for the cylinder, particularly for sharp corner bodies, reporting an increased number of possible flow regimes (as a function of flow velocity). As the side corners are progressively rounded, the flow response moves from “diamond-like” to “cylinder-like”, and the number of flow regimes possible (as a function of flow velocity) decreases. More complex prismatic shapes are studied for bridge decks, and many investigations have been conducted. For example, Diana *et al.* [62] carried out experiments on VIV of a multibox deck girder to evaluate the vibration amplitudes and the lock-in frequency ranges.

2.3.2 Stream-wise motion (in-line, x).

Since the 1970's, stream-wise vibration were found to be possible for cylinders in cross flow. Though pure stream-wise VIV of bluff bodies have not been thoroughly investigated compared to transverse motion or pitching and plunging oscillations of airfoils. This is because the fluid forces observed in this direction usually tend to be an order of magnitude smaller than those seen in the transverse direction [63]. However, in recent years there has been a renewed interest in VIV acting in the stream-wise direction, as the freedom-to-move in this direction has been found to greatly alter the overall response regime compared to that of a cylinder vibrating only in the transverse direction [64].

It is well known that, in uniform flow, the preferred mode of vortex shedding is anti-symmetric. The peculiarity of stream-wise oscillations is that the mode of shedding can be

antisymmetric, symmetric, or chaotic depending on the forcing frequency and amplitude. Therefore, a transition from antisymmetric to symmetric shedding may be expected.

Griffin & Ramberg [65] were among the first to study vortex shedding from an oscillating cylinder in the stream-wise direction. They found that the vortex shedding frequency, f_v , locks-in to the oscillation frequency, f_e , and to the half of it, calling “primary” lock-in ($f_v = f_e$) and “subharmonic” lock-in ($f_v = f_e/2$). This means that synchronisation occurs also for a frequency range around twice the vortex shedding frequency. A factor of 2 is employed to take into account the fact that alternating vortex shedding at one frequency induces a component of the force in the stream-wise direction at twice that frequency.

An extensive summary on bluff bodies stream-wise VIV has been presented by Nau-dascher [66], in which different shapes are considered (rounded, angular-shaped, axisymmetric bodies as well as plates). Among other aspects, he described the shear-layer breathing behaviour, over a vibration cycle. When the cylinder is in the downstream position, the free shear layers move closer together forming a narrower wake. The near wake reaches a minimum width as the cylinder moves upstream. In the upstream position, a new vortex pair starts to grow near the separation points which are moving upstream, fluid from the near wake feeds these vortices, and the free shear layers move outward. The near wake reaches a maximum width when the cylinder is in its downstream stroke. This was observed also for angular bluff bodies, that is with fixed separation points. He also pointed out that in all cases the excitation was shown to be affected by similar instability-induced and movement-induced phenomena (both IIE and MIE). This means that without stream-wise motion there is no symmetrical formation of pairs of vortices and no feedback fluid forces to sustain the free vibration.

Mittal & Tezduyar [67] run computations on unsteady flow past a cylinder forced to oscillate in the stream-wise direction. As expected they observed a change from an asymmetric mode of vortex shedding to a symmetric one. Other numerical investigations have been done by Srikanth *et al.* [68] on a rectangular section oscillating stream-wise at low Reynolds number. They claim to be the first to obtain computational results showing the so called S-II mode, where the symmetric vortex shedding involves two pair of vortices per cycle. A variant symmetric mode, named as S-III mode, is also observed (which means three pairs of vortices shed per cycle). Moreover, they attributed the observed chaotic

regime to mode competition (asymmetric and symmetric vortex shedding).

Recently, experiments on stream-wise VIV of a cylinder have been conducted by Cagney *et al.* [69, 70]. What they observed in general, already noticed in the past by other researchers, is that lock-in for stream-wise vibration direction is driven by the drag force. They investigate thoroughly mode competition between symmetric and asymmetric vortex shedding: the symmetric mode was found to be less stable and short in time [69]. Also, they studied the wake and structural response finding that the cylinder experienced two regions of comparatively high amplitude oscillations (called first and second response branch), separated by a low amplitude region [70].

2.3.3 Coupled stream-wise/transverse motion (x, y) .

Jauvtis & Williamson [71] studied experimentally the response of an elastically mounted cylinder which is free to move in two translating degrees of freedom, transverse and stream-wise directions, at low Reynolds numbers. The main question they posed was “to what extent does stream-wise motion influence the transverse vibration”. It was found that, against expectations, the freedom to move in two directions has very little effect on the transverse response and the vortex wake dynamics.

2.4 Oscillating airfoils

A 2-D airfoil can have three degrees of freedom to vibrate, as shown in Fig. 2.8: two translational (transverse, or plunging, and stream-wise, i.e. respectively vertical and in-line with respect to the flow) and one rotational (pitching).

The pitching and plunging motion of airfoils have been studied for decades. Early theoretical analyses and experiments of oscillating flat plates date back to the 1920's and 1930's with the need to understand/predict the onset of aircraft with flutter. In those years, Theodorsen [72] and Garrick [73] described the time-dependent loads acting on a flat plate undergoing combined forced sinusoidal oscillation in plunge and pitch motion in a 2-D potential flow. Experiments of an airfoil in an oscillating flow were conducted by Katzmayer [74]. Their studies also showed that oscillating airfoils can generate thrust at certain combinations of oscillation frequency and amplitude.

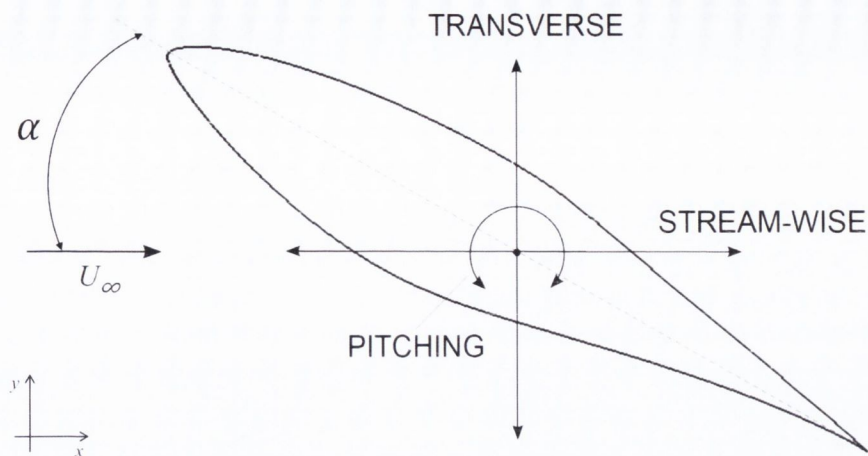


Figure 2.8: Schematic of a 2-D airfoil degrees of freedom. The airfoil is the NREL S809.

One of the most fundamental problems investigated in the domain of unsteady airfoils is the case in which the effective incidence of the airfoil oscillates periodically. Accordingly, the aerodynamic loads fluctuate (leading, in many cases to vibration and noise). In real situations, the oscillation of the incidence is caused usually by a periodic fluctuation of the external flow (e.g. airplanes passing through turbulence) or by a forced oscillation of the airfoil itself (e.g. the pitching oscillation of helicopters rotor blades). A thorough review on unsteady airfoils (sinusoidal pitching motion) has been made by McCroskey in the early 1980's [75].

2.4.1 Pitching motion (α).

The main focus of the study of airfoil pitching motion has been the dynamic stall phenomenon for rotorcraft or turbomachinery blades. Experiments were conducted by Carr [76] and by McCroskey *et al.* [77]. The latter considered high Reynolds numbers (order of 10^6) and investigated the effect of leading edge modification. They stated that the main difference between static and dynamic stall is the vortex shedding phenomenon, and consequently the transient aerodynamic forces and moments produced are considerably larger.

The vortex shedding characteristics of a pitching airfoil has been investigated experimentally, among others, by Koochesfahani [78]. He showed that at certain high reduced frequencies the wake transforms into a jet-like flow with thrust generation. He also re-

vealed that the characteristics of the near-wake were highly influenced by the amplitude of oscillation and Reynolds number (freestream velocity). Other experiments were conducted by Chang & Eun [79] who reported mean velocity and turbulent intensity profiles in the near wake of an elliptic airfoil oscillating in pitching motion at moderate Reynolds numbers (order of 10^4).

Numerical studies have been done by, among others, Akbari & Price [80] who simulated the flow field around pitching elliptic airfoils. They investigated the effect of parameters like the oscillation frequency, the mean angle of attack and the location of the pitching axis. In this regard, they noted that moving the pitch-axis from the mid-chord to the quarter-chord caused the formation of stronger vortices, which lead to a more unsteady and complex wake structure. However, the fundamental characteristics of the flow field remained the same. The pitching axis positioned at the half-chord point was used also by Mittal & Tezduyar [67]).

In general, these studies have been confined to low/moderate Reynolds flow regimes, and the angles of attack considered are not substantially above the angle of stall. In addition, most studies refer to symmetrical airfoils (for example NACA 0012 or elliptic shaped airfoils). An interest in high-Reynolds flow is showed by Raveh & Dowell [81] who conducted a study on the frequency lock-in phenomenon for oscillating airfoils in transonic buffeting flows. In the turbomachinery field, Zhu & Kamemoto [82] determined experimentally the lock-in boundaries, for certain angles of attack, of an axial pump blade subjected to pitching motion.

In recent years, the dynamic stall problem study has been extended to wind turbine rotor blades as well (e.g. CFD analysis by Johansen *et al.* [83], Yu *et al.* [84]).

Recently, Hasegawa & Nakagawa [85] measured the unsteady fluid forces of a pitching discoid 3-D airfoil, at a incidence of 90° and moderate Reynolds number (order of 10^4), in order to investigate the relationship between the forces and the vortex behaviour. They described the vortex growth during the downstroke path due to the pressure difference between the windward and the leeward side of the airfoil. This growth is related also to the relative velocity between the airfoil's edge velocity and the freestream one, hence the vortex strength increases with the reduced frequency. As a consequence, the vortex generation/growth occurs during the downstroke path; after that, the vortex shedding

from the airfoil's edge takes place during the upstroke path.

An interest in frequency lock-in of airfoils is demonstrated by some work done recently. Tang & Dowell [86] conducted experiments on a NACA0012 at high angles of attack and relatively high Reynolds numbers (1×10^5 to 5×10^5). The lock-in behaviour of the airfoil oscillating with a prescribed pitching motion about the quarter-chord was determined ("V"-shaped lock-in region). Vortex-induced vibrations on the same airfoil in pitching motion at the same Reynolds number regime have been studied by Besem *et al.* [87], both experimentally and numerically. Wind tunnel experiments were conducted for incidences $\alpha = [25^\circ \rightarrow 90^\circ]$. A computational analysis was also carried out in order to determine the lock-in region at $\alpha = 40^\circ$, which is observed to be not perfectly symmetric about the natural shedding frequency. At this angle of attack, they calculate a Strouhal number of about 0.16 (static airfoil configuration), for a Reynolds number of 2×10^5 . In addition, they report that the airfoil does not shed numerically for $\alpha = 30^\circ$, while in the experiments the vortex shedding starts to appear at $\alpha = 25^\circ$. This may be due to substantial differences between experimental and numerical studies, e.g. surface roughness (present in the experiments), turbulence model (used in the CFD model).

2.4.2 Transverse motion (plunging, y).

For airfoils, heave (transverse) motion is called plunge. In years, plunging motion of airfoils has received less attention than pitching motion which has been studied especially due to the links with fixed wing twisting modes, helicopter blade motion and generic dynamic stall. Recently though, plunging motion gained importance thanks to the interest in bio-fluid dynamics (mechanics of animal locomotion), with the aim to understand thrust generation from oscillating airfoils. Studies on pure plunging motion of symmetrical airfoils have been conducted by, e.g., Wang [88] and Lai & Platzer [89]. The latter showed that the wake of a plunging airfoil can be characterised as "drag-producing, neutral or thrust-producing" depending on the plunge motion frequency and amplitude. A numerical study on the vortex shedding lock-in phenomenon in the wake has been done by Young & Lai [90]. They reported that lock-in boundaries are not symmetric about the natural vortex shedding frequency, due to the presence of the airfoil's sharp trailing edge forcing the flow to separate at the trailing edge on the windward side of the airfoil for the majority

of the plunge cycle at higher frequencies and amplitudes.

Some work has been done for transverse VIV on airfoils at very high angles of attack. Ehrmann *et al.* [91] conducted experiments on different types of airfoil shape at $\alpha = 90^\circ$, a round-round edged airfoil, a sharp-sharp edged airfoil and a NACA 0018 airfoil, to be compared to results obtained for a cylinder. The main outcome is that the presence of a sharp leading or trailing edge affects the lock-in behaviour significantly, leading to a smaller response (i.e. smaller lock-in range). Instead, an airfoil with both rounded edges presents a similar (comparable magnitude) response amplitude of a cylinder, albeit smaller. On the other hand its wake characteristics are similar to a proper airfoil (NACA 0018 and sharp edges). Another difference between rounded and sharp edges is that no hysteresis was observed for airfoils in presence of sharp edge. In addition, the airfoil shapes present a more spanwise coherence of vortex shedding, indicated by small and consistent phase differences, different from the cylinder behaviour.

Another interesting work has been done by Skrzypiński *et al.* [48] who conducted a CFD unsteady analysis of vortex-induced vibrations of a DU96-W-180 airfoil at $\alpha = 90^\circ$ in the transverse direction, based on 2-D/3-D RANS and 3-D DES approaches. They report that, even though the 2-D computations seemed to be capable of indicating the presence of vortex induced vibrations, the 3-D computations appeared more accurate. Also, they observed that the spanwise load correlation in the 3-D flow was higher for the oscillating airfoil than for the static case.

2.4.3 Transverse/pitching motion (flapping, y, α).

Flapping motion of airfoils indicates a combined plunging and pitching motion; this configuration well matches the animal flight technique. The tradition in scientific work inspired by biological locomotion dates back at least to the 1500's when Leonardo da Vinci designed a number of ornithopters based on bird's flight [88]. The basic mechanism of thrust generation in flapping flight was illustrated by Glauert [92] in a classical linear theory of an oscillating wing in inviscid flow. Glauert's theory predicts a thrust, generated by shedding a vortex wake which carries the momentum backward with respect to the wing.

The development of micro air vehicles increased the need to understand the flapping-

wing mechanism used in nature; therefore, the majority of bio-fluid dynamics studies concern a flapping airfoil at low Reynolds number. A review on flapping-wing aerodynamics has been drafted by Platzer *et al.* [93]. On this topic, works have been done by Ohmi *et al.* on symmetric airfoils (elliptic airfoil [94] and NACA 0012 [95]) undergoing constant translational motion combined with harmonic pitching motion. Tuncer & Platzer [96] conducted a computational study on a flapping NACA 0012 airfoil finding that a maximum propulsive efficiency is obtained for cases where the flow remains mostly attached.

Despite the usual low Reynolds regime linked to this problem, some works have been done also for high Reynolds numbers. Ashraf *et al.* [97] investigated the effect of Reynolds number (up to $Re = 2 \times 10^6$), airfoil's camber and thickness on flapping airfoil propulsion, observing that for thin airfoils a large leading edge vortex is formed (due to a sharp leading edge) causing significant drag. Thick airfoils are less prone to experience leading edge flow separation, hence an optimum thickness for propulsive performance was observed. Isogai *et al.* [98] conducted numerical simulations at $Re = 10^5$, observing high propulsion efficiency by optimizing the interaction of the leading edge vortex with the airfoil motion, i.e. for a combination of phase angle (pitch oscillation leading the plunge oscillation by 90°) and motion parameters for which there appears no appreciable flow separation.

Regarding wind turbines blade sections, Guerri *et al.* [99] investigated flow induced vibrations of a NACA 632 415 airfoil using CFD, though at low Reynolds number and small angles of attack.

2.4.4 Stream-wise motion (in-line, x).

As a general comment, to date no interest seems to be shown for stream-wise VIV of airfoils, especially at high angles of attack and high Reynolds numbers. What has been studied, was confined to a dynamic stall context.

The interest to investigate the unsteady events occurring on rotor blade in forward flight brought Maresca *et al.* [100] to conduct experiments on a symmetric airfoil (NACA 0012), at relative high incidences (around stall), in longitudinal oscillations (i.e. parallel to the flow). They observed that for incidences above stall ($\alpha = 20^\circ$), strong unsteady effects appear and depend on the frequency and amplitude of the oscillations. Also,

their instantaneous data reveal that the airfoil was experiencing both dynamic stall and dynamic reattachment of the boundary layer, which contribute to a favourable effect of unsteadiness on the mean lift coefficient. The measurements indicate an overshoot of the instantaneous lift and drag which is explained by a strong vortex shedding process occurring during the dynamic stall. These events are quite similar to those observed in the case of oscillations in pitch motion [101]. Instead, dynamic reattachment which occurs progressively from the leading edge may be observed for a short part of the period, when the airfoil is going forward. The same NACA 0012 airfoil was considered by Favier *et al.* [102] to conduct a study on the combined pitching and fore-aft translation motion (parallel to the flow).

2.5 Summary

Studies of the unsteady flow around moving airfoils have been carried out for decades. In the beginning, the focus has been on the pitching motion in order to understand the dynamic stall phenomenon in the aeronautic field (rotorcraft and turbomachinery blades), for practical reasons.

The problem of vortex shedding of airfoils at very high angles of attack and high Reynolds number does not seem to be studied with the same emphasis, contrary to common bluff body shapes such as cylinders and prisms for which extensive work is present in the literature. In addition, it seems that for airfoils (at high Reynolds number and high angles of attack) no particular attention has been paid to the lock-in phenomenon, especially with experiments. Moreover, studies on oscillating airfoils commonly involve pitching and plunging (transverse) motions, owing to the already existing tradition in aeronautical research. Chord-wise (stream-wise) motion does not receive the same attention. Nonetheless, some recent work on this topic has appeared, indicating that a research interest on VIV of airfoils is becoming established.

From these observations, after a review of the literature on vortex shedding of generic shapes and on oscillating airfoils, it can be concluded that vortex shedding of airfoils at high angles of attack and high Reynolds numbers (vortex-induced vibration, lock-in) represents a wide open research topic, as well as a challenge for researchers.

Chapter 3

Computational Fluid Dynamics model

Païdoussis *et al.* [16] presented a classification of VIV models with different approaches depending on the grade of accuracy, shown schematically in Fig. 3.1. The simplest one is the *forced system model* where forces are independent on the body motion, and therefore only dependent on time (case of static body). The next step is the *fluidelastic system model* where the forces depend on both time and body's motion. The last and more accurate is the *coupled system model* where the forces depend on another variable related to the wake dynamics, the evolution of which depends on the body's motion. The first two models are limited since there is no relation to the physics of the wake, whereas the third one considers the fluid forces as the result of the wake dynamics itself influenced by the body motion, therefore considering VIV as resulting from the coupling of two systems (the bluff body and the unstable wake).

Following the VIV models classification presented above, the current work presents a study of vortex shedding on the NREL S809 airfoil based on these first two models. The forced system model, i.e. static airfoil, is described in Chapter 4; the fluidelastic system model, i.e. forced oscillating airfoil, is described in Chapter 5 and 7. The focus of the analysis is the range of motion frequencies at which the lock-in phenomenon (between vortex shedding frequency and motion frequency) occurs.

This Chapter introduces the CFD model used throughout this work.

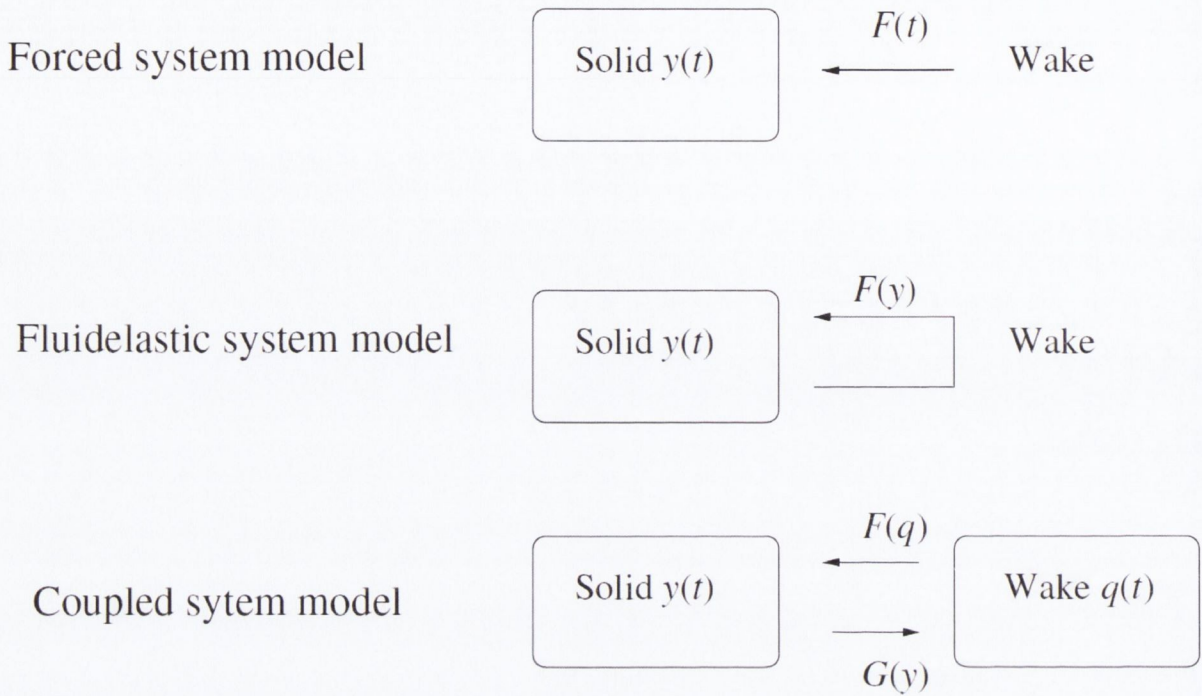


Figure 3.1: VIV models classification [16].

3.1 Set-up

The fluid domain, illustrated in Fig. 3.2 has been created with the ANSYS[®] default meshing tool. It must be flagged that, due to a continuing upgrade of the platforms used for this work during these years, different releases of the ANSYS Fluent[®] software have been used: 14.0, 14.5, 15.0.

The domain extends to $10c$ (airfoil chord) length from the body in the upstream direction, $40c$ in the downstream direction and $10c$ in both the vertical upward and downward directions. The reference chord length is 1m. Although the fluid domain is relatively small for an airfoil at low incidences, for the high angles of attack considered in this work it can be said that the induced velocity at the inlet boundary is low and can be therefore neglected. The fluid domain has been divided into different zones in which the mesh density is different, keeping it finer in the vicinity of the airfoil and fading in the far wake downstream. Note that these zones are used for mesh generation and are not boundaries in the flow field. The inner zone has been modelled as a circle in order to facilitate the rotation of the airfoil with respect to the incoming flow, when needed. To

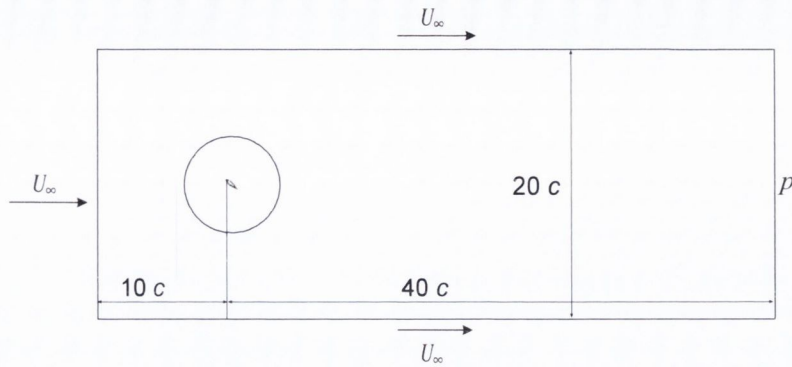


Figure 3.2: Flow field domain: dimensions and boundary conditions.

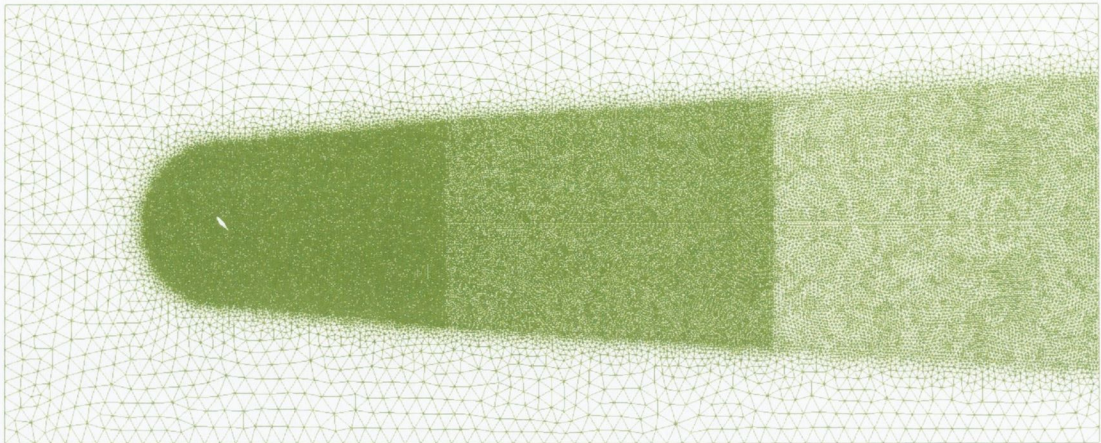
simulate the oscillating airfoil (Chapters 5 and 7), a sliding mesh is used (rather than a solid body translation/rotation of the whole grid, for example) to have a defined far field, and a moving surface rather than a moving boundary. The mesh is unstructured, with triangular elements throughout except the quadratic elements in the boundary layer. The near wall mesh has 512 cells in the chord-wise direction and the overall mesh is composed in total of approximately 100,000 nodes. In the wake zone, the cell size is 0.05m in the near field, 0.09m in the mid-field and 0.15m in the far field. Figure 3.3 shows the fluid domain grid, overall view (3.3(a)) and close-up (3.3(b)).

The no-slip condition was used at the airfoil surface. Inlet flow velocity was specified at the upstream boundary of the domain, with the inflow conditions shown in Tab. 3.1. Flow velocity has been set based on a Reynolds number value of $Re = 10^6$ with air as the fluid. The outlet condition was specified in the downstream boundary of the domain with a reference pressure $p_{\text{gauge}} = 0$.

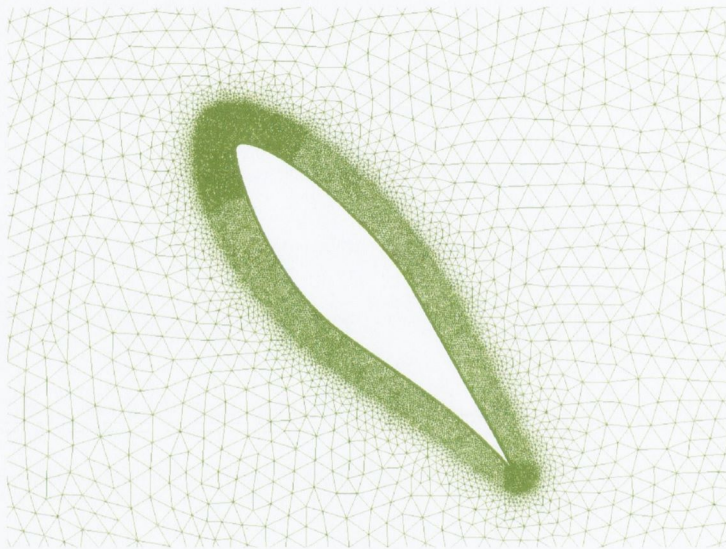
Inlet flow properties ($Re = 10^6$)			
Velocity	U_∞	14.607	m/s
Density	ρ	1.225	kg/m ³
Viscosity	μ	1.7894×10^{-5}	kg/ms

Table 3.1: Inlet flow properties.

Turbulence closure is achieved by the Shear Stress Transport SST eddy viscosity model (fully turbulent mode). This transition turbulence model requires a fine mesh in the vicinity of the airfoil. For that purpose, the height of the first cell has been tuned in order



(a) Overall mesh,



(b) Mesh airfoil close-up.

Figure 3.3: Fluid domain grid.

to obtain a y^+ value below 2 everywhere on the airfoil surface. The applied boundary conditions value for the turbulent quantities k and ω is 1 (default solver value). A second order scheme is used for the momentum equations, whereas a first order scheme is used for the turbulence equations.

This model runs on a (Linux based) system with 24 parallel cores. Each node has a CPU clock rate of 2.4GHz and a RAM of 64GB. The wall clock time per simulation (motion parametric study, see Chapters 5 and 7) is in the range of 40-60 hours.

3.2 Validation

The validation of the fluid dynamic model concerns both the near field and the far field, keeping the same flow properties and Reynolds number, to fully test the fluid-dynamic model. For the near field validation, a steady-state analysis has been conducted for an angular range $\alpha = [0^\circ \rightarrow 18^\circ]$ (Section 3.2.1). Such analysis deals with the capability of the model to capture the physics in the near vicinity of the airfoil. For the far field, where the vortex shedding phenomenon develops, the standard case of unsteady flow around a cylinder was analysed, as there is almost no detailed experimental data available for vortex shedding of airfoils at high angle of attack and high Reynolds number (Section 3.2.2). The unsteady vortex shedding analysis requires accuracy in the far field behind the body too.

3.2.1 Steady case (airfoil)

In Figure 3.4 the lift and drag curves at steady-state conditions are presented. The current results are compared with Delft University of Technology experimental results [103] and CFD results available in the literature, obtained for the same Reynolds number of 10^6 . It can be seen that a good agreement has been achieved. First of all, the lift curve upward slope (Fig. 3.4(a)) is well captured in the pre-stall regime. The stall regime is well predicted too. This means that the model succeeds in capturing the physics for an attached boundary layer and for a detached boundary layer in the stall regime (albeit not yet fully detached, characteristics of a bluff body). Likewise, as shown in Fig. 3.4(b), the pre-stall regime is well captured also for the drag. In the stall regime the drag is under-predicted compared with experimental results, which is not surprising due to the 2-dimensionality of this analysis. Nonetheless, current results are comparable with other 2-D numerical ones. Note that the turbulence model used, Shear Stress Transport (SST), is optimised for this study configuration and hence widely used. In fact its good behaviour in adverse pressure gradients and separating flow is well known. Accurate results required a residuals tolerance of 10^{-6} .

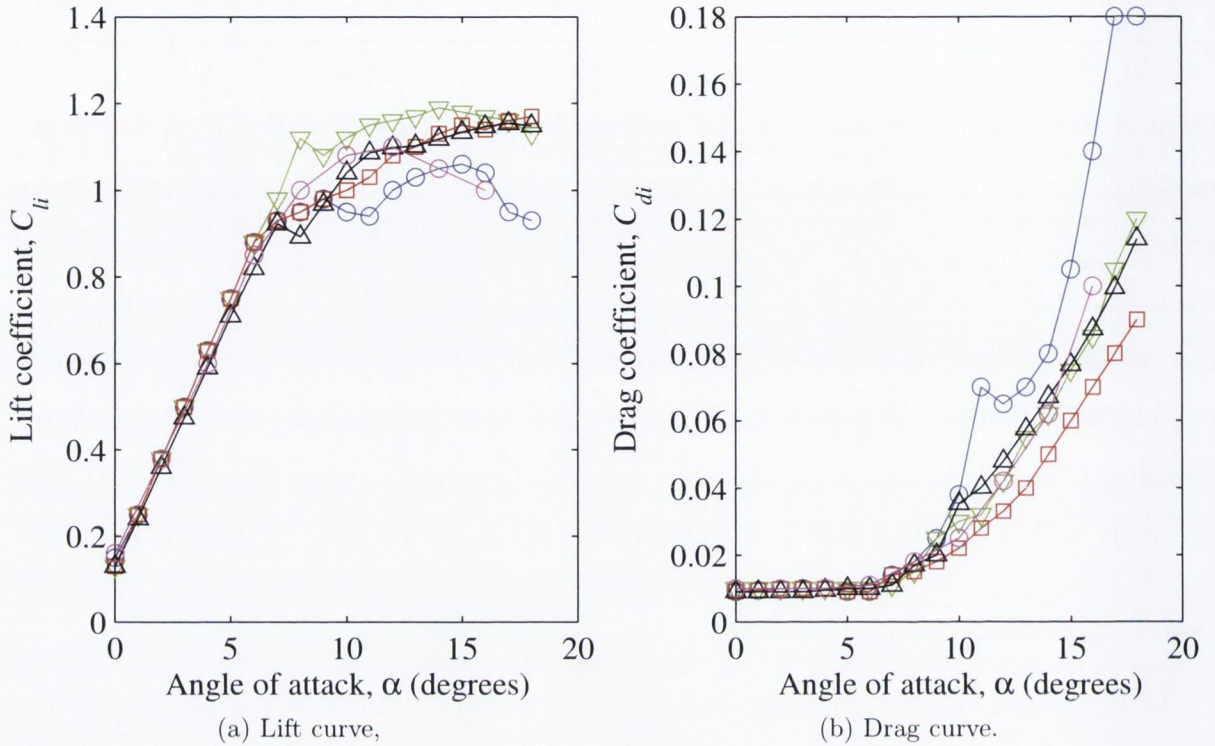


Figure 3.4: Steady aerodynamic force coefficients for the NREL S809 airfoil at $Re = 10^6$ against angle of attack. Comparison between $-\circ-$, Delft University Experiments [103] and CFD results: $-\nabla-$, ANSYS-CFX; $-\square-$, XFOIL 6.0; $-\circ-$, ELLIPSYS 2D; $-\triangle-$, current study (ANSYS-Fluent).

3.2.2 Unsteady case (cylinder)

As mentioned before, limited data are available for vortex shedding from airfoils at high angles of attack. Therefore, in order to have confidence in the modelling approach, at first it was sensible to conduct a preliminary unsteady analysis on a cylinder for which detailed experimental results are present in the literature. For this test case the same model settings and conditions are used, as well as the characteristic length (cylinder diameter, $d = 1\text{m}$).

The PISO scheme, with Second Order Upwind discretization for the momentum, is used (segregated mode), with sub-iterations within the individual time-steps. The formal order of the time integration scheme is less than 2.

A time-step of 0.005s is used. The choice of the time-step value has been advanced starting from the commonly used non-dimensional vortex shedding frequency for cylinders, $St = 0.2$. This value of 0.005s is used for the static case of NREL S809 airfoil in Chapter 4.

For the oscillating case (Chapters 5 and 7) the time-step value has been halved ($\Delta t = 0.0025\text{s}$). This choice came after migration to a distributive platform (Linux based), for which the results of the model validation seem to be unpredictable with $\Delta t = 0.005\text{s}$. Note that the time-step has been chosen relatively large considering that this work deals with a high recirculation zone in the near field, and with wake instability. It was sufficient enough to capture vortex shedding and it allowed to conduct an extensive parametric study with a reasonable wall clock time per simulation.

Figure 3.5 shows a typical contour plot of instantaneous vorticity behind a cylinder, consistent with the wake structure results available in the literature. In Tab. 3.2, experimental and simulated values of Strouhal number, lift coefficient root mean square and mean drag coefficient are given. Results show a good agreement with experiments for both the vortex shedding frequency and the amplitude of the aerodynamic forces. It must be said that the model needed to be tuned: accurate results required a residuals tolerance of at least 10^{-5} . In addition, a momentum under-relaxation factor value of 0.5 (the solver default value was 0.7) is needed to avoid residual divergence at the beginning of the simulation due to the high turbulence level associated with the relatively high Reynolds number ($Re = 10^6$).

	Experiments	CFD results
St	0.255	0.262
$C_l[\text{rms}]$	0.08	0.08
$C_d[\text{mean}]$	0.55	0.5

Table 3.2: Smooth cylinder test validation with experiments data [104].

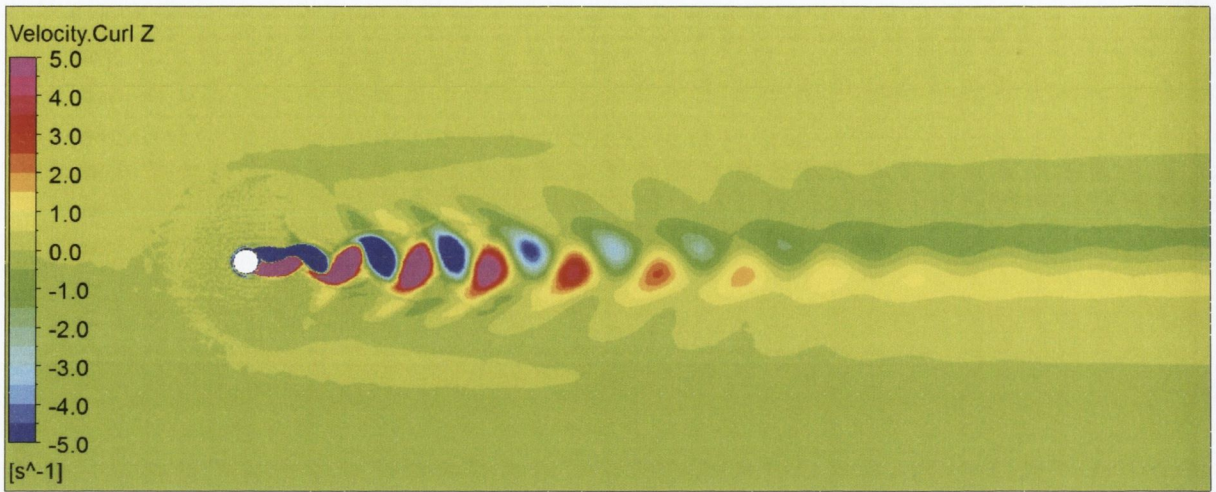


Figure 3.5: Instantaneous vorticity magnitude for a circular cylinder, $t=10s$. ■, counter-clockwise (positive) vorticity; ■, clockwise (negative) vorticity.

3.2.3 Sensitivity analysis

A sensitivity analysis of the model (unsteady case with airfoil) has been conducted considering the Strouhal number of the fixed airfoil at $\alpha = 40^\circ$ ($St = 0.148$). The aim is to assess if a sufficient grid resolution is applied, as well as a reasonable time-step value.

The size of the grid elements has been doubled and halved; the finer mesh does not give a different result of the Strouhal number, while it does the coarser one (see Table 3.3). Hence the used grid can be considered appropriate.

Then, four time-steps ($n\Delta t$, with $n = 2, 1, 1/2, 1/4$) have been used with the same grid (see Table 3.4). A doubled time-step gives a different Strouhal number value, whereas a smaller time-step gives almost the same result. The choice goes to $\Delta t = 0.005s$ for a practical reason of time consumption per simulation.

Grid	St
Used	0.148
Coarser	0.145
Finer	0.148

Table 3.3: Grid sensitivity analysis.

Δt [s]	St
0.01	0.144
0.005	0.148
0.0025	0.149
0.00125	0.149

Table 3.4: Time-step sensitivity analysis.

3.3 Summary

The fluid-dynamic model has been validated for a steady and unsteady regime. Good agreement has been achieved with steady results of the NREL S809. Reasonable agreement has been obtained also with unsteady results for vortex shedding of a cylinder.

Therefore results obtained suggested that this model might be a reliable mean to conduct both steady and unsteady analysis for high Reynolds numbers (fully turbulent flow regime).

Once verified, the fluid-dynamic model (at the same Reynolds number and using the same meshing density and turbulence model) has been used to perform simulations of the unsteady flow around the wind turbine blade section at different angles of attack, in the positive range $\alpha = [0^\circ \rightarrow 180^\circ]$ and negative range $\alpha = [0^\circ \rightarrow -180^\circ]$, stepping by 10° , to give a clear idea of the global airfoil behaviour. This is presented in the next Chapter.

Chapter 4

Case 1: static airfoil

A series of two-dimensional unsteady simulations of the flow around the NREL S809 airfoil, in a static configuration, at different angles of attack have been performed. Figure 4.1 shows the S809 with the positive angular direction specified for the airfoil inclination with respect to the freestream direction. Two typical configurations are illustrated: airfoil with the sharp trailing edge (labelled STE in Fig. 4.1) in down-wind position, Fig. 4.1(a), and up-wind position, Fig. 4.1(b). All calculations have been made at $Re = 10^6$.

The PISO scheme, with Second Order Upwind discretization for the momentum and a time-step of 0.005s have been used.

Using the data obtained, the non-dimensional vortex shedding frequency (i.e. the Strouhal number) and the non-dimensional loading coefficients at higher harmonics have been calculated, for different angles of attack.

4.1 Harmonic forces decomposition

The lift force, L , is defined perpendicular to the flow direction, while the drag is parallel to the flow. When considering the loads on airfoils it is common to use the pitching moment, M , around the quarter chord (i.e. a point on the chord line, 25% of the chord from the leading edge) as this is theoretically the aerodynamic centre. However, as this airfoil is at such a high angle of attack and the behaviour as a bluff body is of most interest here, the pitching moment has been taken through the mid-chord point (i.e. equidistant from leading and trailing edge).

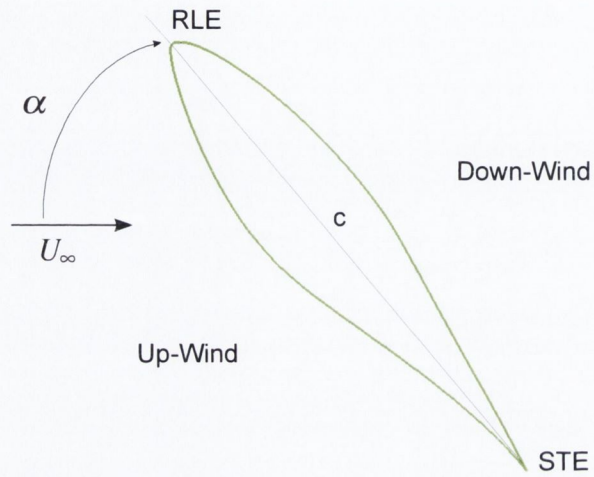
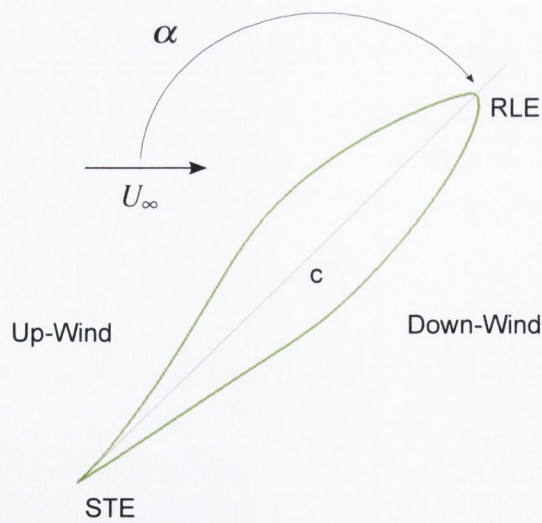
(a) $0^\circ < \alpha < 90^\circ$,(b) $90^\circ < \alpha < 180^\circ$.

Figure 4.1: Schematic of the NREL S809 airfoil for positive angles of attack. RLE is rounded-leading-edge, STE is sharp-trailing-edge.

The aerodynamic loads can be non-dimensionalised using the chord as the reference length:

$$\begin{aligned} C_l &= \frac{L}{0.5\rho U_\infty^2 c} \\ C_d &= \frac{D}{0.5\rho U_\infty^2 c} \\ C_m &= \frac{M}{0.5\rho U_\infty^2 c^2} \end{aligned} \quad (4.1)$$

The time series of the aerodynamic forces and moment coefficients have been decomposed into Fourier series, as shown in Eq. (4.2), in order to quantify the vortex induced excitation at higher frequencies.

$$C_g(t) = C_{g0} + \sum_k C_{gk} \sin(k2\pi f_v t + \phi_k) \quad (4.2)$$

where C_g is the overall instantaneous force coefficient, C_{g0} is the mean coefficient, C_{gk} is the amplitude of the fluctuating force coefficient for the k^{th} harmonic, f_v is the vortex shedding frequency, ϕ_k is the phase for the k^{th} harmonic.

Once the fundamental vortex shedding frequency has been obtained for each angle of attack, the Fourier coefficients at harmonics of this frequency are obtained. For the lift force, the first three harmonics are needed to fit the time data, whereas the first four harmonics are required for the drag force and the pitching moment.

Two ranges of angles of attack have been considered, positive $\alpha = [20^\circ \rightarrow 160^\circ]$ and negative $\alpha = [-20^\circ \rightarrow -160^\circ]$. The ranges $\alpha = [0^\circ \rightarrow \pm 20^\circ]$ and $\alpha = [180^\circ \rightarrow \pm 20^\circ]$ have not been considered since at these angles the flow is largely attached and so no periodic vortex shedding would be expected. The CFD simulations have been run for a physical time of 10s to allow the periodic wake associated with vortex shedding to become established. The transient initial period is discarded, and only established period vortex shedding is considered.

Although large separated fluid regions are present for incidences in ranges of $-30^\circ < \alpha < 30^\circ$ and $150^\circ < \alpha < -160^\circ$, no evidence of periodic vortex shedding has been seen for these angles of attack, maybe due to the damping/dissipation associated with a 2-D, 2-equations RANS simulation. This is shown in Fig. 4.2. For example, at $\alpha = 20^\circ$ and $\alpha = 150^\circ$ (respectively in Figs. 4.2(a) and 4.2(b)) the wake is formed by the two

shear layers which eventually dissipate, without turning into a vortex street. For $\alpha = 30^\circ$ (Fig. 4.2(c)) vortices pairs are shed, albeit not properly organised as in a Kármán vortex street (therefore it is not a periodic vortex shedding dominated by a fundamental vortex shedding frequency). This can be seen as a transitional regime where the vortex shedding is starting to establish itself. Therefore the range of angle of attack discussed below is confined to $\alpha = [40^\circ \rightarrow 140^\circ]$, $\alpha = [-40^\circ \rightarrow -150^\circ]$.

It must be acknowledged that the same configuration performed on another CFD solver and hardware led to a different result, i.e. periodic vortex shedding has been observed for incidences below $\alpha \approx 40^\circ$. This fact should be taken into account as it may influence some of the conclusions made in this work. For the present finding, a possible explanation could be that the mesh used is not extremely fine and the time-step used is relatively large. Therefore, the small scales of vorticity typical for low incidences are not captured by this model, even if it would be normally expected to observe periodic vortex shedding also for $\alpha < 35^\circ$. Though, the objective of the study is the configuration at very high angles of attack.

A typical contour plot of instantaneous vorticity is shown in Fig. 4.3. The particular case of $\alpha = 50^\circ$ at 10s is illustrated. The flow field immediately behind the airfoil, which is effectively a bluff body, is specific to the geometry. Close to the airfoil the wake structure appears to be highly asymmetric which is consistent with results from Perry & Steiner [39] for a flat plate at an incidence angle of 45° . In the downstream wake a familiar vortex street can be seen.

The CFD simulations provide the temporal variation of the aerodynamic forces (lift, drag) and pitching moment. Figure 4.4 shows the time record of these aerodynamic coefficients for $\alpha = 50^\circ$. The simulated time is 10s, giving then both the transient and the periodic part of the signal. For the sake of clarity, in Fig. 4.5 the detail of these records with only 1.2s of time is also presented. These plots are typical of what has been obtained for all the present simulations. It is apparent that all three quantities are periodic, with significant higher harmonics, leading to signals which are not pure sinusoids.

It has been noted that $\alpha = 50^\circ$ is a significant incidence. A dramatic change in behaviour has been observed between $\alpha = 40^\circ$ and $\alpha = 50^\circ$. This will be consistent for all the results presented in this thesis.

Figure 4.6 shows that, compared to Fig. 4.5, for $\alpha = 40^\circ$ the higher harmonics content is lower for all three load coefficients.

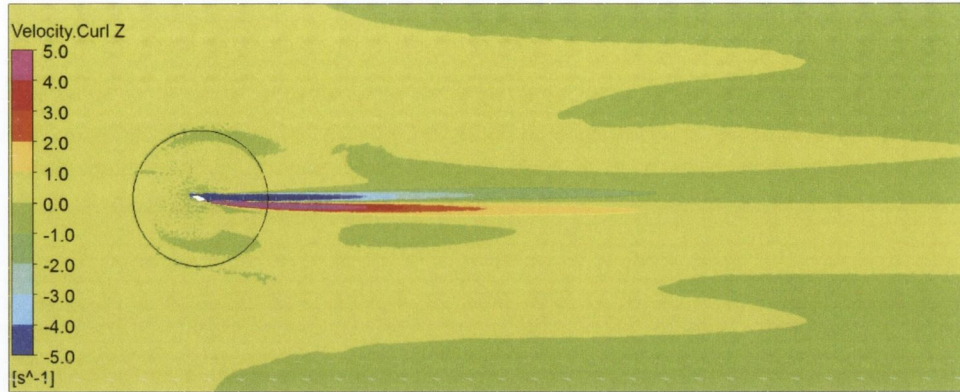
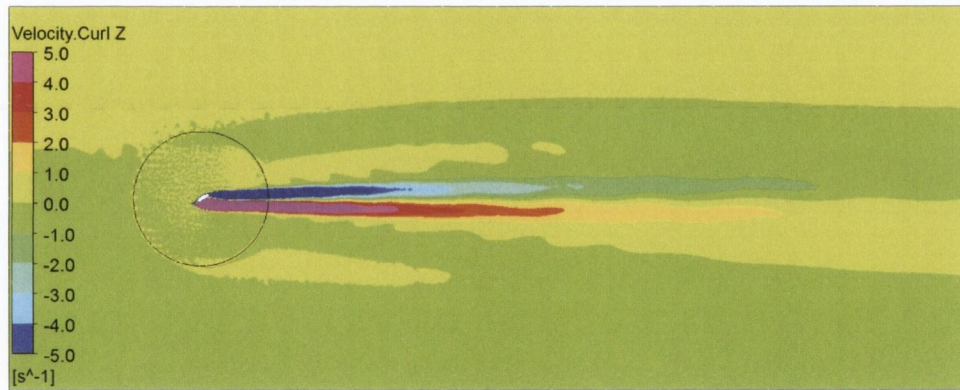
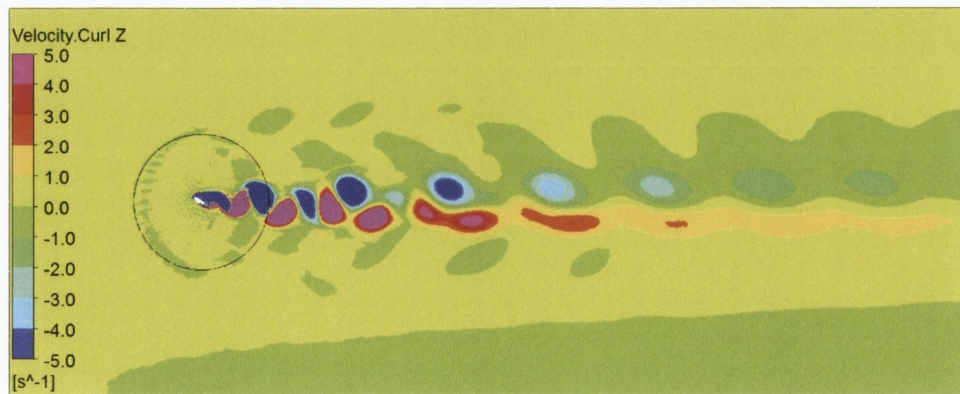
(a) $\alpha = 20^\circ$,(b) $\alpha = 150^\circ$,(c) $\alpha = 30^\circ$.

Figure 4.2: Instantaneous vorticity magnitude at different incidences, $t = 10s$. Vortex shedding is not observed for $\alpha = 20^\circ$ (a) and $\alpha = 150^\circ$ (b). Vortex shedding is not periodic for $\alpha = 30^\circ$ (c). ■, counter-clockwise (positive) vorticity; ■, clockwise (negative) vorticity.

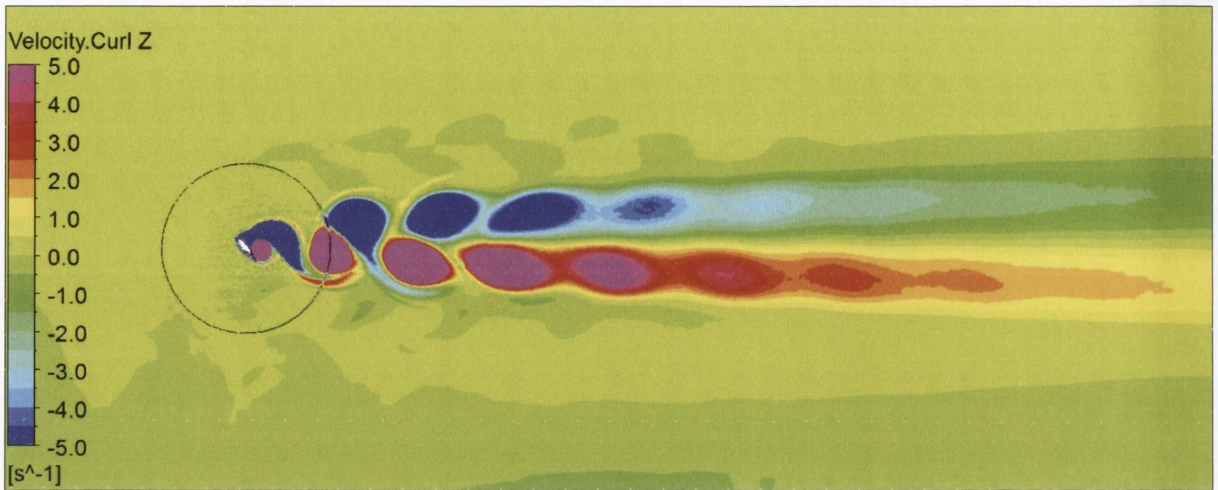


Figure 4.3: Instantaneous vorticity magnitude at $\alpha = 50^\circ$, $t=10s$. ■, counter-clockwise (positive) vorticity; ■, clockwise (negative) vorticity.

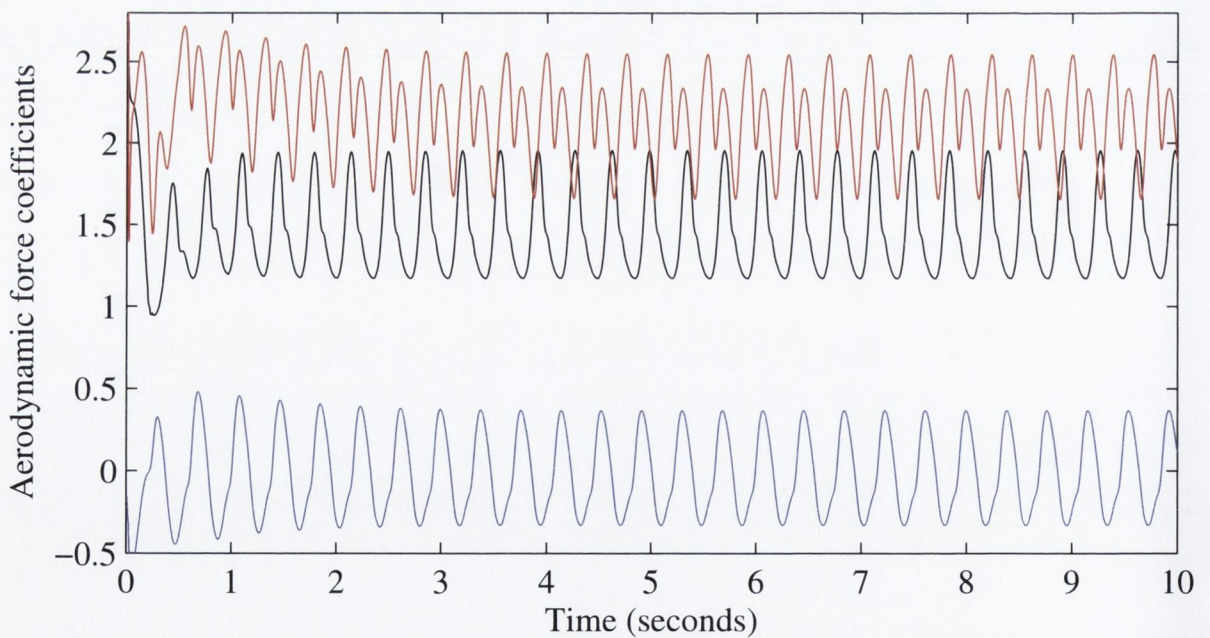
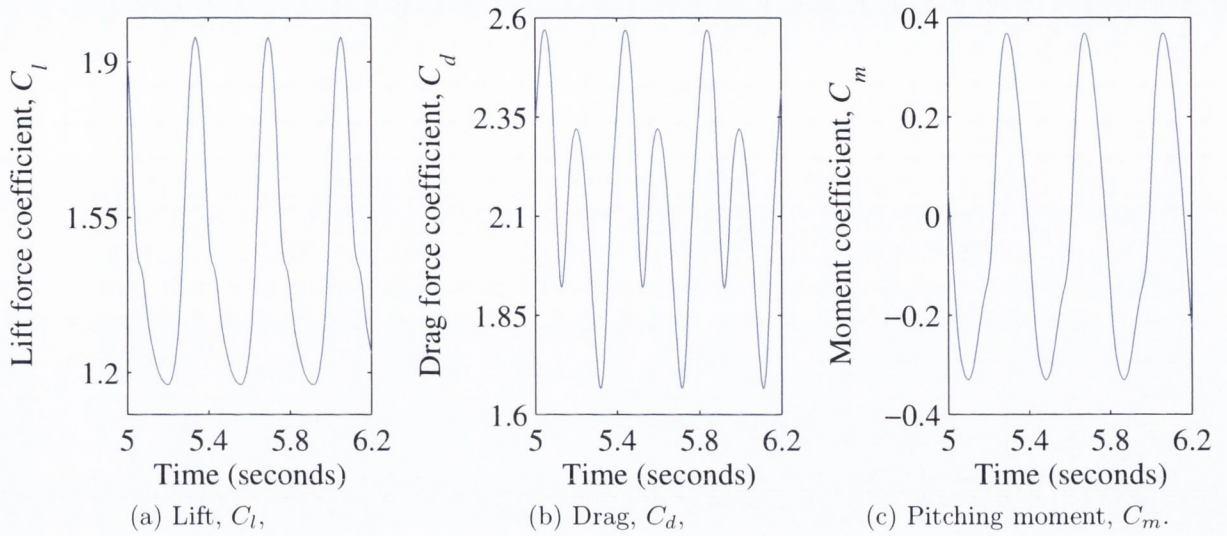
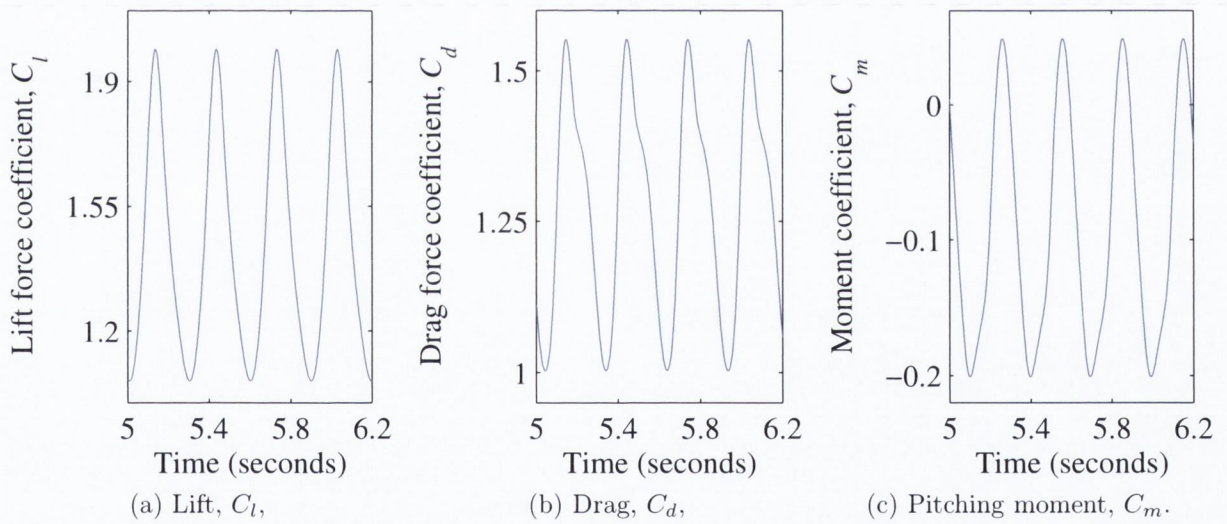


Figure 4.4: Time record of the aerodynamic force coefficients at $\alpha = 50^\circ$: —, lift coefficient, C_l ; —, drag coefficient, C_d ; —, pitching moment coefficient, C_m .

Figure 4.5: Detail of the time record of the aerodynamic force coefficients at $\alpha = 50^\circ$.Figure 4.6: Detail of the time record of the aerodynamic force coefficients at $\alpha = 40^\circ$.

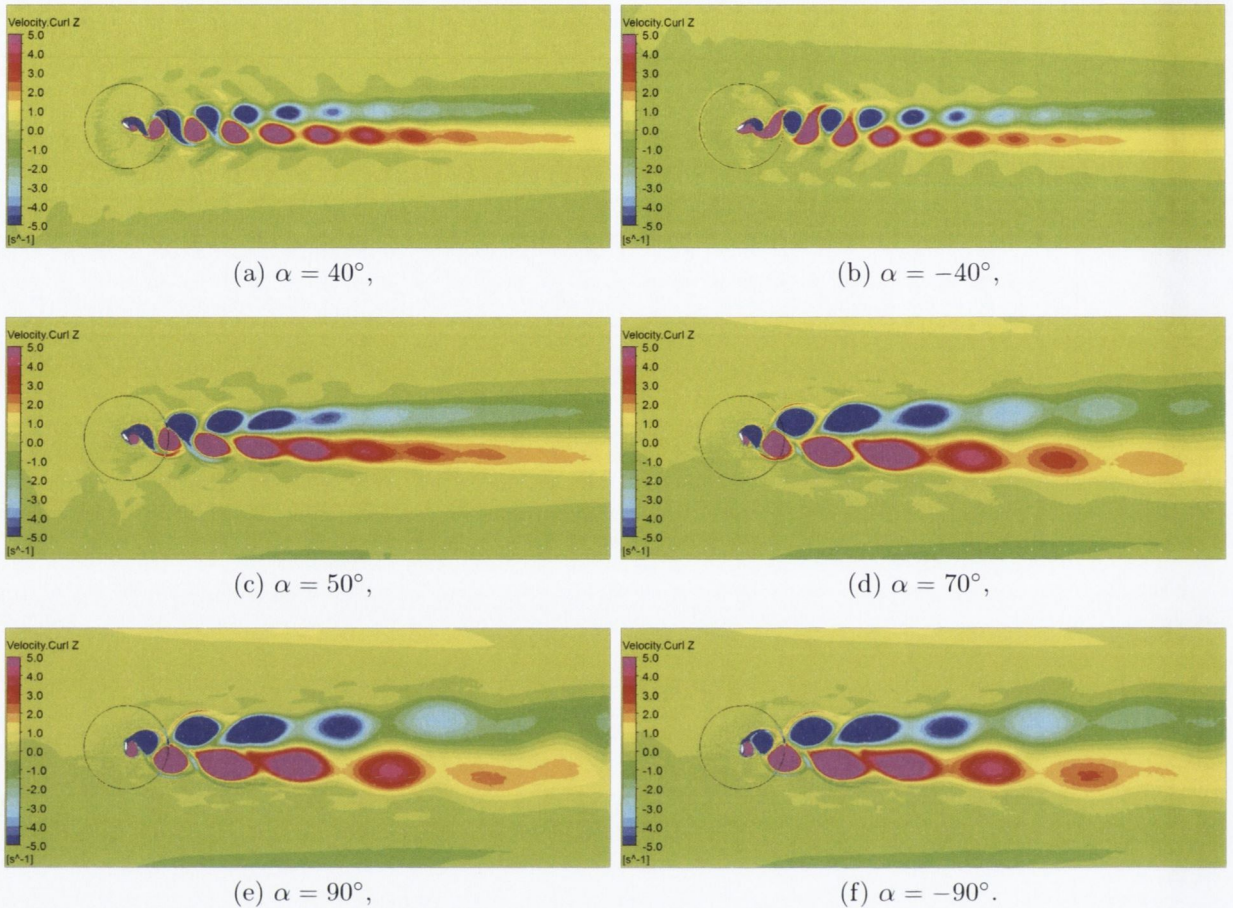


Figure 4.7: Instantaneous vorticity magnitude at different incidences, $t = 10s$, showing different vortex street structures. ■, counter-clockwise (positive) vorticity; ■, clockwise (negative) vorticity.

Figure 4.7 shows the vortex street at different angles of attack. It can be seen that as α is increased towards a vertical position of the airfoil to the flow (Figs. 4.7(a), 4.7(c), 4.7(d), 4.7(e)), the vortex shape becomes bigger and more elongated. Also, the vortex spacing increases both in the x and y direction. This is consistent with results found in the literature (about the von Kármán h/a , see Chapter 2). Figures 4.7(a) and 4.7(b) show that the wake structure for $\alpha = 40^\circ$ and $\alpha = -40^\circ$ is very similar, seen in a specular way as the trailing edge will be either downward or upward. This suggests that the airfoil camber's effect is not dominant at such high incidences. Moreover, Figs. 4.7(e) and 4.7(f) show that, when the airfoil is in a vertical position to the flow, the separation point on the leading edge is well defined too and whether the leading edge is in the up or down position it does not make any difference. In fact these two wakes are highly comparable

in all their features.

These observation will be presented again under other evidences in Sections 4.1.1, 4.1.2.

4.1.1 Strouhal number

The Strouhal number at each angle of attack considered has been obtained from the frequency of vortex shedding, i.e. the frequency of the lift coefficient signal.

Figure 4.8 shows the Strouhal number trend against angle of attack. As expected, the frequency of the vortex shedding in the wake is a function of the angle of attack, consistent with what found by Nair & Sengupta [44] in their experiments on elliptic prisms at high angle of attack and moderate Reynolds numbers. Two normalisations are considered: the first uses the chord of the airfoil as the characteristic length ($d = c$), while the other uses the projection of the chord on the vertical axis ($d = c \sin \alpha$). The St trend in the case of the projected chord shows less variation than with the simple geometric reference length (as also can be found in [20]).

A Strouhal number value of approximately 0.15 is found, for example, at $\alpha = 40^\circ$. As a comparison, a value ≈ 0.16 is reported for an airfoil (NACA0012) investigated numerically at the same incidence (yet at a lower Reynolds number of 2×10^5) [87].

No symmetry is present, with respect to the angular position of $\alpha = \pm 90^\circ$, due to the interchanging convex-concave as the upper-lower side of the airfoil. In general it can be noticed that the St takes higher values for the negative angles of attack compared with positive angles. This is probably due to the presence in negative angular positions of a cusp (i.e. trailing edge) on the leeward side of the airfoil which strongly affects the vorticity in the near proximity of the body.

4.1.2 Mean and fluctuating loads

The fluid loadings coefficients (lift, drag, pitching moment) have been decomposed into mean and periodic components as shown in Eq.(4.2), for each angle of attack considered.

Figure 4.9 shows the variation of the mean forces and moment component coefficients (C_{l0} , C_{d0} , C_{m0}) with angle of attack. It can be seen that the lift coefficient changes in sign approaching $\alpha = 90^\circ$. It is relatively high and is comparable to what would be expected

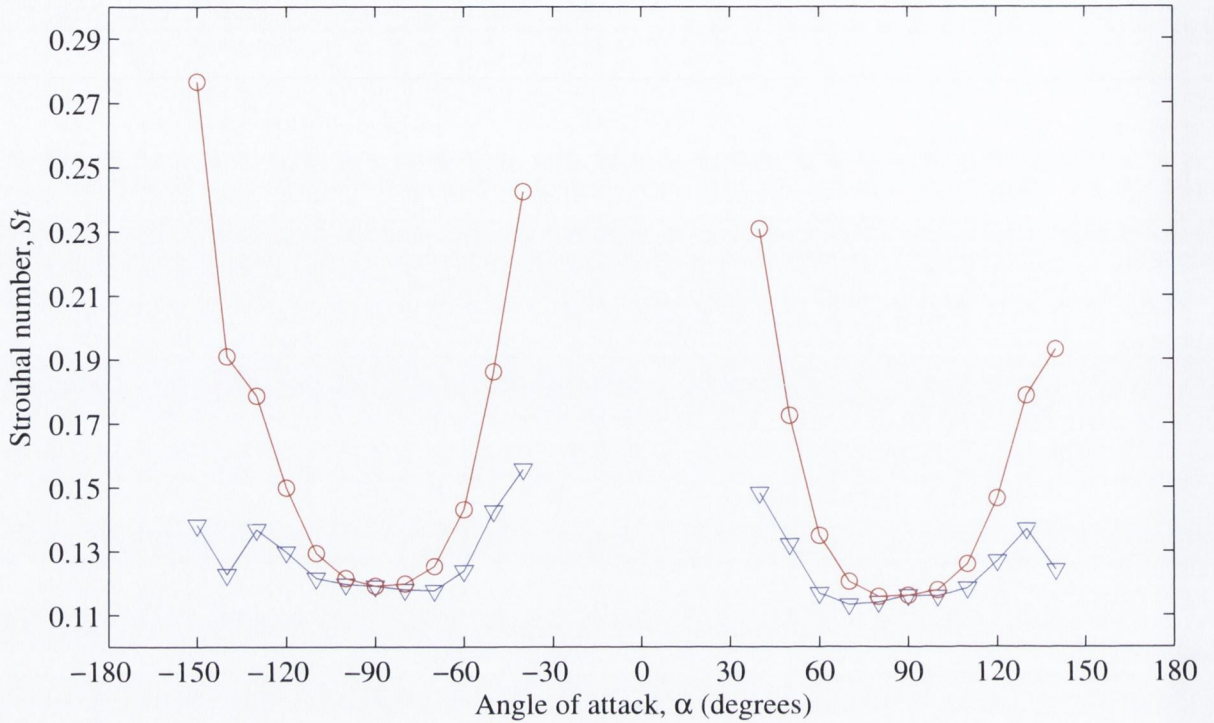


Figure 4.8: Strouhal number against angle of attack with different characteristic length: $-\circ-$, airfoil chord (c); $-\nabla-$, projected chord ($c \sin \alpha$).

at low angle of attack typical of the design operational range. However, unsurprisingly for high angles of attack, this is accompanied by a very high mean drag coefficient, which is one order of magnitude greater than what would be found at low angles. For a comparison, a flat plate at $\alpha = 90^\circ$ presents a two-dimensional drag coefficient $C_d \approx 2$ [46].

The moment behaviour by comparison is very flat, albeit showing a sign change.

There is no substantial difference in the mean coefficients between positive and negative angles of attack, indicating that the camber of the airfoil is not of significant importance at these high angles. Furthermore, the mean coefficients for angles in the range $\alpha = [40^\circ \rightarrow 90^\circ]$ and $\alpha = [-140^\circ \rightarrow -90^\circ]$ are comparable, indicating that the shape of the leading edge is unimportant as for $90^\circ < \alpha < -90^\circ$ the sharp trailing edge is actually upwind of the rounded leading edge. These observations suggest that, at least for the mean force coefficients the values obtained may be generally applicable to a wide range of airfoil sections.

Figure 4.10 plots the variation with angle of attack of the coefficient of the lift force components for the first three harmonics of the vortex shedding frequency (C_{l1} , C_{l2} , C_{l3}).

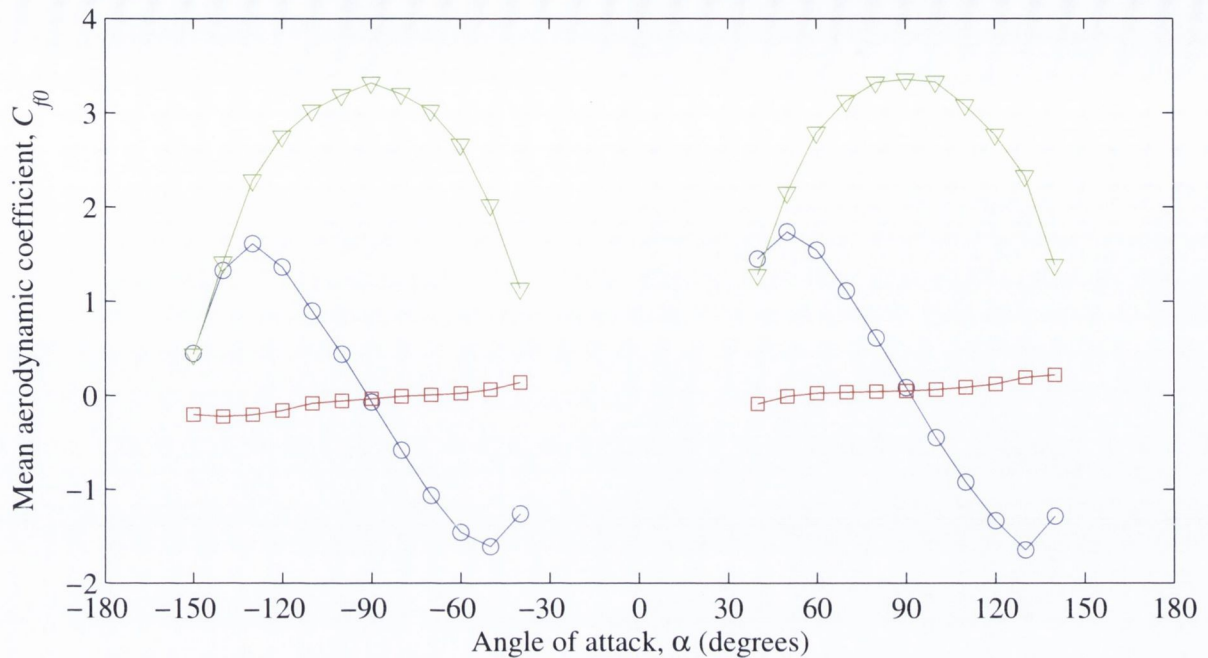


Figure 4.9: Mean forces component coefficients against angle of attack: $-\circ-$, mean lift coefficient, C_{l0} ; $-\nabla-$, mean drag coefficient, C_{d0} ; $-\square-$, mean pitching moment coefficient, C_{m0} .

The main characteristic is that the first harmonic dominates, as would be expected, for the whole range of angles considered. The second harmonic is greater than the third. The trend of each harmonic for positive and negative angles is similar. However, it can be seen that for positive angles of attack the first harmonic of lift experiences a minimum around 70° , while for negative angles the trend is monotonic. This is due to the camber: geometrically, positive angles of attack present the oncoming flow with a concave shape, while negative angles present a convex profile. A more significant feature, in contrast to the mean coefficient, C_{l0} , for angles where the sharp trailing edge is upwind ($90^\circ < \alpha < -90^\circ$), the fluctuating lift force at the vortex shedding frequency is substantially higher, than when the rounded leading edge is upwind ($-90^\circ < \alpha < 90^\circ$).

Figure 4.11 shows the variation with angle of attack of the coefficient of the drag force components for the first four harmonics of the vortex shedding frequency (C_{d1} , C_{d2} , C_{d3} , C_{d4}). In this case, the even harmonics are as important as the odd harmonics, with the second harmonic dominating in the region around $\alpha = \pm 90^\circ$. This is consistent with vortex shedding for a cylinder [29, 30]. The trends for all harmonics are similar for

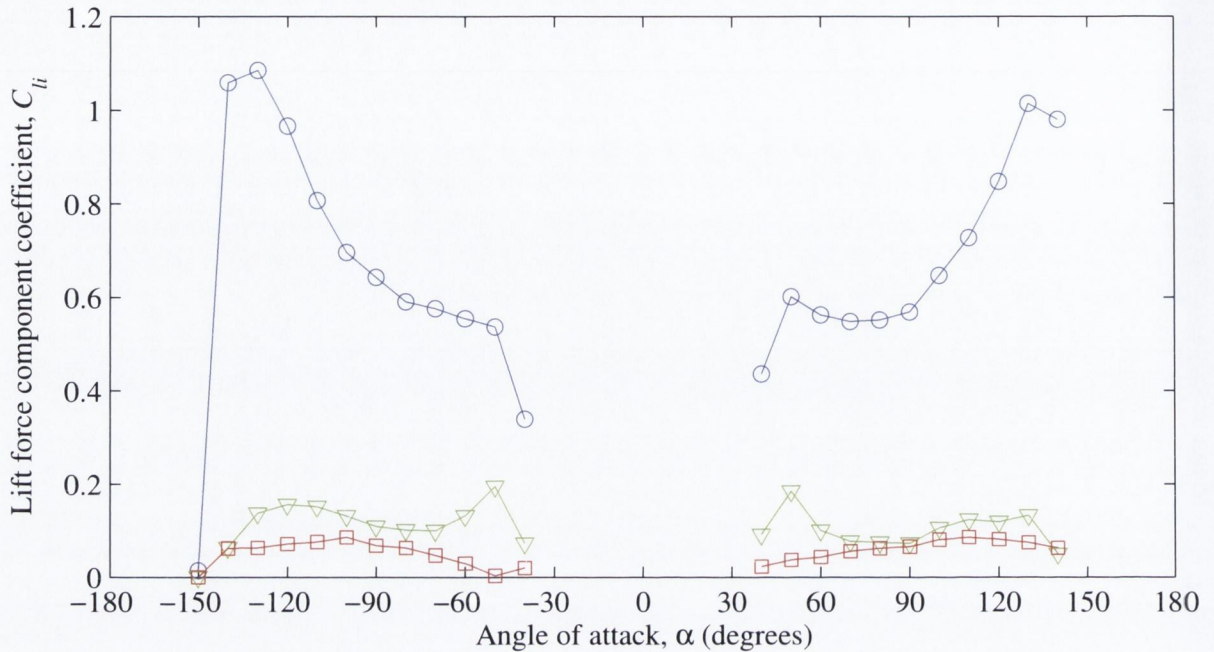


Figure 4.10: Lift force component coefficients against angle of attack: $-\circ-$, first harmonic; $-\nabla-$, second harmonic; $-\square-$, third harmonic.

both positive and negative angles of attack, again suggesting that camber is not much important. The coefficient for the second harmonic is lower when the sharp trailing edge is upwind, while the first harmonic is largely insensitive to this.

Figure 4.12 shows the associated coefficients for the pitching moment about the mid-chord for the first four harmonics (C_{m1} , C_{m2} , C_{m3} , C_{m4}) which follow similar behaviour to the lift coefficient. In fact, as seen for the lift force, the first harmonic is dominating for the whole range of angles considered, though presenting higher values when the rounded leading edge is upwind ($-90^\circ < \alpha < 90^\circ$). Instead, the second harmonic is greater than the third just when the rounded leading edge is upwind ($-90^\circ < \alpha < 90^\circ$), and not in the whole range.

Figure 4.13 shows the phase angle relative to the lift coefficient of the dominant harmonic of the moment and drag coefficient, as determined in Figs. 4.10, 4.11 and 4.12. The subscript denotes the coefficients and the harmonic number. As can be seen the moment is always out of phase with the lift for all angles of attack. This is an artefact of the sign convention and the choice of the mid-chord for the centre of moment. The drag coefficient is a little harder to interpret. For $|\alpha| > 120^\circ$ the first harmonic of the drag is dominant

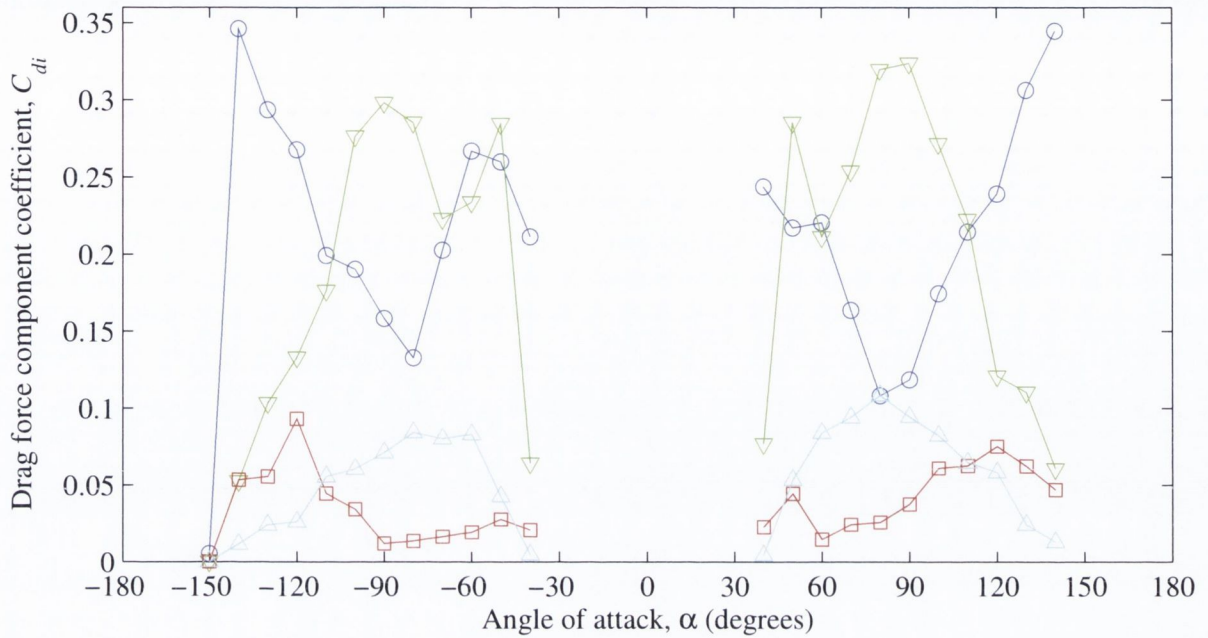


Figure 4.11: Drag force component coefficients against angle of attack: $- \bigcirc -$, first harmonic; $- \nabla -$, second harmonic; $- \square -$, third harmonic; $- \triangle -$, fourth harmonic.

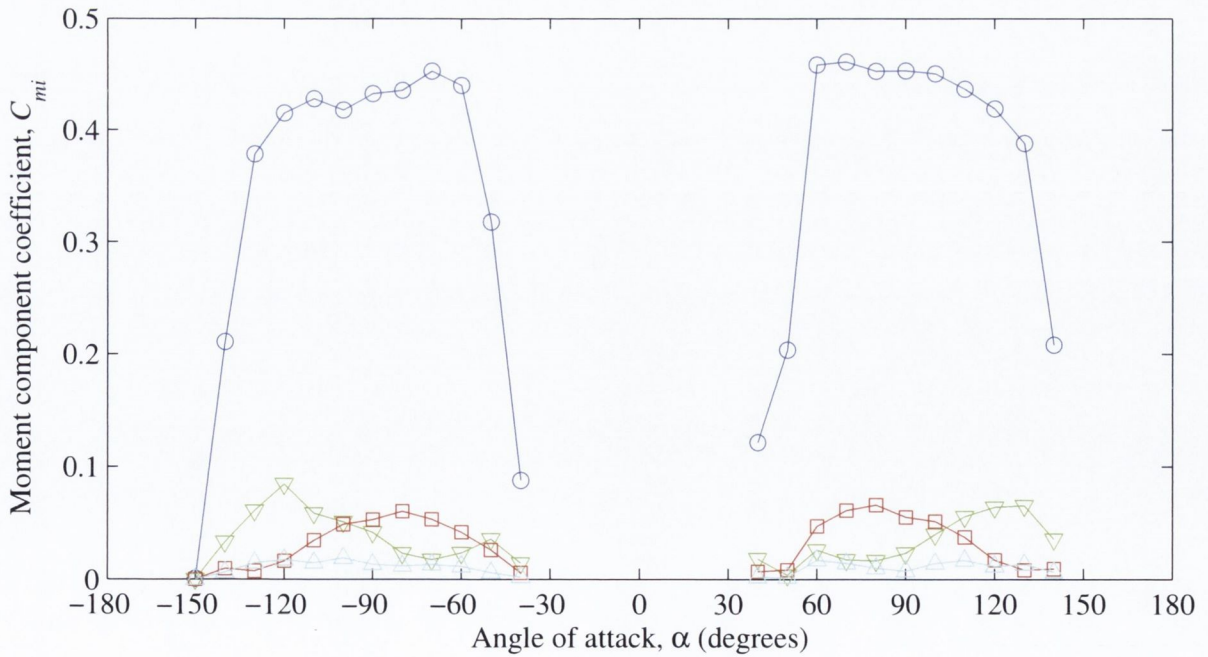


Figure 4.12: Moment component coefficients against angle of attack: $- \bigcirc -$, first harmonic; $- \nabla -$, second harmonic; $- \square -$, third harmonic; $- \triangle -$, fourth harmonic.

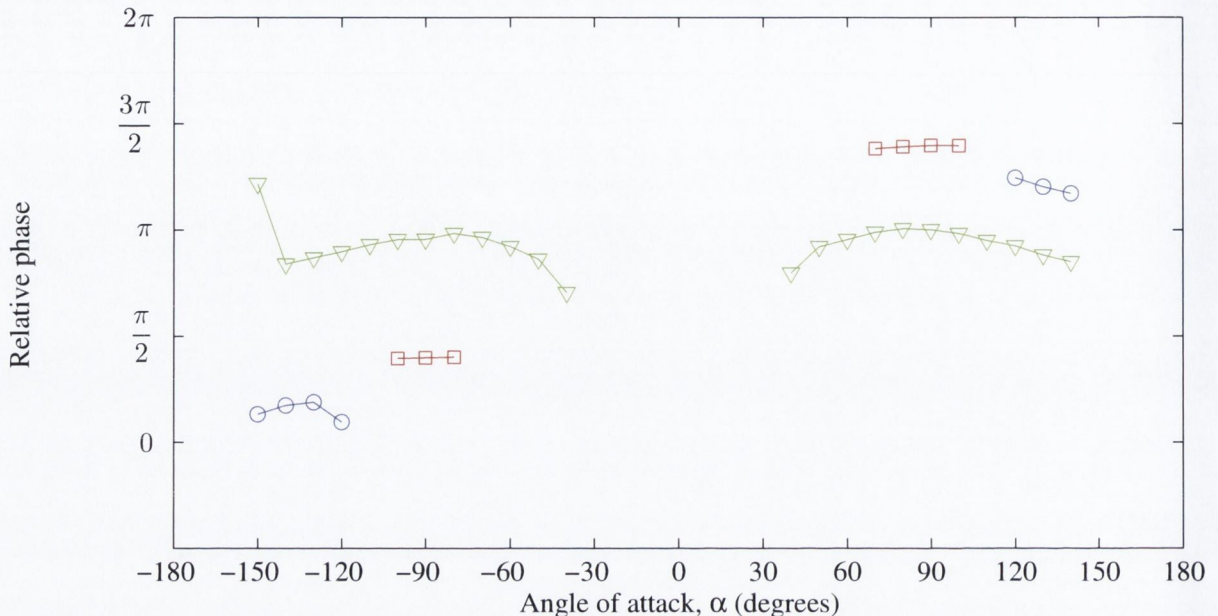


Figure 4.13: Relative phase of dominant harmonic: $-\circ-$, $[\phi_{l1d1}]$; $-\square-$, $[\phi_{l1d2}]$; $-\nabla-$, $[\phi_{l1m1}]$.

and so the phase difference is straight forward. For $|\alpha| \approx 90^\circ$ the second harmonic is the largest, so a pseudo phase angle is calculated as: $\phi_{l1d2} = \phi_{l1} - \frac{1}{2}\phi_{d2}$. At a number of angles the first and second harmonics are comparable, and so it is not possible to extract a meaningful phase for these. What is apparent is that the phase of the drag is approximately 0 for negative angles and approximately π for positive angles. This jump is effectively a minus sign in the amplitude which is related to the sign convention: a negative angle of attack will generate lift downwards, while drag is always in the stream-wise direction.

4.2 Summary

It has been shown that, in general, the wake shape behind the NREL S809 at high incidences is consistent with what is seen in the literature for common bluff bodies, suggesting that the vortex shedding process has been correctly captured. When the projected chord of the blade section is used to non-dimensionalise the vortex shedding frequency, the Strouhal number varies from 0.12 to 0.16 for negative angles $\alpha = [-40^\circ \rightarrow -150^\circ]$ and from 0.11 to 0.15 for positive angles $\alpha = [40^\circ \rightarrow 140^\circ]$.

The magnitude and harmonic content of the fluctuating forces and moment depend

on the angle of attack. Furthermore, the strength of the loading depends on whether the sharp trailing edge is upstream or downstream; when the trailing edge is upstream, the first harmonic of lift and drag are higher whereas for the pitching moment is lower, but the second harmonic of drag is lower whereas for the pitching moment is higher. It has been observed that, as both positive and negative incidences provide similar behaviours in terms of periodic loads, the effect of the airfoil's camber may be minimal. Therefore, the results obtained may be applicable to a wider range of airfoil's shapes.

An analysis on the phase angle relative to the lift coefficient of the dominant harmonic of the moment and drag coefficient showed that the moment and drag are synchronised with the lift. When the magnitude of lift increases due to a vortex being shed, so too does the moment and drag.

In the next Chapter, the study on the moving airfoil in a 1-DOF forced oscillation is presented, for all the three types of motion (see Fig. 2.8). This forced motion configuration represents the fluidelastic system model presented by Païdoussis *et al.* [16] (see Chapter 3).

Chapter 5

Case 2: 1-DOF moving airfoil

The fluidelastic system model [16], i.e. the NREL S809 airfoil forced to oscillate, is presented in this Chapter. The aim is to define the frequency range of motion at which synchronisation with the vortex shedding frequency occurs, for different high incidences and a relatively high Reynolds number ($Re = 10^6$). This is accomplished for each type of motion (pitching, stream-wise or x , transverse or y).

In order to determine the lock-in region for the moving airfoil at a given mean angle of attack, the vortex-shedding characteristics of the airfoil in a static configuration at that angle of attack must be known (see Chapter 4). The vortex shedding frequency depends on the mean angle of attack. With the static vortex shedding frequency, f_{v0} , (i.e. with no airfoil motion) at each mean angle of attack considered, α_{mean} , and being f_m the generic frequency of motion, the frequency ratio for a generic type of motion, r , can be defined as:

$$r = \frac{f_m}{f_{v0}} \quad (5.1)$$

As the static vortex shedding frequency is fixed for a given α_{mean} and flow velocity, the motion frequency, f_m , is varied to obtain each value of r . The range of mean incidences investigated is ($35^\circ \leq \alpha_{mean} \leq 145^\circ$), as no periodic vortex shedding has been observed in the ranges ($0^\circ \leq \alpha_{mean} \leq 30^\circ$) and ($150^\circ \leq \alpha_{mean} \leq 180^\circ$) at the Reynolds number considered (see Chapter 4). In the ranges ($35^\circ \leq \alpha_{mean} \leq 50^\circ$) and ($130^\circ \leq \alpha_{mean} \leq 145^\circ$) an α_{mean} increment of 5° was used, whereas in the range ($50^\circ \leq \alpha_{mean} \leq 130^\circ$) the α_{mean}

increment was 10° , as in this region no rapid change in the lock-in characteristics has been observed. Furthermore only the positive range of angles of attack ($0^\circ \leq \alpha_{mean} \leq 180^\circ$) has been considered, as for the negative range ($0^\circ \geq \alpha_{mean} \geq -180^\circ$) it is assumed that the behaviour will be qualitatively the same. This is based on the vortex shedding behaviour for the static airfoil (see Chapter 4).

The assessment of the lock-in condition is obtained with an analysis of the spectrum of the lift force coefficient, since the frequencies present in the wake are expected to be equal to the frequencies observed in the fluctuating lift force coefficient [28]. Therefore, if the vortex shedding frequency locks in to the motion frequency, a unique dominant frequency (with its possible harmonics) will be observed in the fluctuating lift force coefficient (see for example Bishop & Hassan [55]). The criterion to assess lock-in adopted in this work is: $f_v = p \cdot f_m$, where p is an integer.

The lift force coefficient results are obtained for a simulated time of 30s. For each of the three types of motion, a parametric study has been conducted for a constant motion amplitude, varying the relative frequency ratio, r , i.e. varying the motion frequency (as the static vortex shedding frequency is fixed) for each angle of attack. Then, an investigation of the motion amplitude effect follows, for some critical angles of attack where synchronisation is seen to be more likely to occur.

Computations have been made using the PISO scheme, with Second Order Upwind discretization for the momentum and a time-step of 0.0025s. It may be useful to express time in a dimensionless fashion as follows:

$$\tau = \frac{tU_\infty}{c} \quad (5.2)$$

Therefore, the dimensionless time-step used is $\Delta\tau = 0.0365$.

All calculations have been made at a Reynolds number of $Re = 10^6$, referred to the airfoil's chord length.

It is worth noting the choice of the two translational motions, “stream-wise” & “transverse”. In wind energy, the two translational motions of a blade section are usually defined as “edge-wise” & “flap-wise” whether it is respectively in- or out-of the plane described by the blade. Precisely, this is true for the section at the root of the blade; then, as the blade is twisted, the sections are oriented differently span-wise, meaning that the

edge-wise motion will have also a small component out-of-plane (and conversely for the flap-wise motion, a small component in-plane). This convention is commonly used because most of the work for wind turbines in the literature refers to standard operational conditions, i.e. at low incidences or near the stall (or not significantly above). For a 2-D airfoil a stricter convention would be calling “edge-wise” & “flap-wise” whether it is respectively an in-line or perpendicular motion with respect to the chord of the airfoil. For the purpose of the current work, this choice would not be sensible. The present work deals with extreme conditions, especially at standstill. In this scenario, the blade section can be oriented in many different configurations to the flow; consequently, for example, an airfoil at $\alpha_{mean} = 90^\circ$ in edge-wise motion will experience an oscillation direction close to that of an airfoil at $\alpha_{mean} = 10^\circ$ in flap-wise motion. Or posing in another way, the flap-wise direction of an airfoil at $\alpha_{mean} = 90^\circ$ is almost perpendicular to the flap-wise direction of an airfoil at $\alpha_{mean} = 10^\circ$. It has been thought that this convention would be no more consistent in such a scenario. Therefore, in this work the motion of the airfoil is defined in terms of the motion direction with respect to the flow direction instead of the chord line (see Fig. 2.8). Hence the terms “stream-wise” & “transverse”.

The NREL S809 subject to a single degree of freedom motion in pitching will be presented in Section 5.1, followed by the stream-wise motion in Section 5.2 and the transverse motion in Section 5.3.

5.1 Pitching oscillation motion

A series of two-dimensional unsteady simulations of the flow around the pitching NREL S809 airfoil have been performed, at first for one oscillation amplitude only, $\alpha_{ampl} = 7^\circ$, for a range of frequency ratios around $r = 1$. This is a reasonably significant amplitude to use as a basis for an analysis of the amplitude effect. For the pitching motion, the frequency ratio, r , is defined by the pitching frequency, f_p , as follows:

$$r = \frac{f_p}{f_{v0}} \quad (5.3)$$

In addition, the effect of pitching amplitude has been examined for angular positions at which the synchronisation appears to be more significant.

For simplicity a sliding mesh technique (rotation of the inner circular zone) has been used rather than either a re-meshing or deforming mesh scheme in order to reduce the computation time (see Fig. 3.2). The pivot point has been set at the middle of chord $c/2$ (i.e. the point on the chord line is equidistant from leading and trailing edge). One could argue that it is common to use the pitching moment around the quarter of chord (25% of the chord from the leading edge) as this is theoretically the aerodynamic center in subsonic regime. The reason for this mid-chord point choice is that this airfoil is at such a high mean angle of attack that the theoretical aerodynamic center is not relevant and the behaviour as a bluff body is of most interest here. Furthermore, for a vibrating blade in torsional motion (i.e. pitching), the elastic axis is likely to be aft of the quarter chord point. The pitching motion has been applied via a compiled User Defined Function (UDF). The motion is described in Eq. 5.4:

$$\alpha(t) = \alpha_{mean} + \alpha_{ampl} \sin(2\pi f_p t) \quad (5.4)$$

5.1.1 Synchronisation at fixed pitching amplitude

In order to illustrate the effect lock-in has on the vortex shedding excitation that would be experienced by the airfoil, the behaviour of the lift coefficient at $\alpha_{mean} = 140^\circ$ is considered. Figure 5.1 shows a portion of the time record of the lift coefficient for two frequency ratios. For the sake of clarity, only 2 seconds of simulated time are shown, after the wake has well developed; dimensionless time is used. At a frequency ratio $r = 0.8$, shown in Fig. 5.1(a) the vortex shedding is not locked-in to the pitching frequency, while Fig. 5.1(b) shows the equivalent record for the locked-in case ($r = 1.1$). It is clear that when the vortex shedding has locked-in, the lift coefficient is periodic, with a single dominant frequency, albeit with harmonics. In contrast, in Fig. 5.1(a) the trace is clearly not periodic, characteristic of the locked-out condition. This behaviour is consistent with the results of an oscillating cylinder studied, among others, by Bishop & Hassan [55]. Although this appears to be narrowband random, in fact the behaviour is a pseudo-periodic response typical of a signal with two distinct, incommensurate but similar frequencies.

Figure 5.2 shows the spectra associated with the two cases seen in Fig. 5.1. Frequencies

have been normalised with the static vortex shedding frequency, giving a non-dimensional frequency: $f^* = f/f_{v0}$. In the locked-out case, for $r = 0.8$ (Figure 5.2(a)), the pitching and the vortex shedding frequencies can be seen at $f^* = 0.8$ and in the vicinity of $f^* = 1$ respectively. A vortex shedding frequency at $f^* = 1$ (highlighted by the dash-dot line) would occur if the airfoil was static. There is also a smaller peak at $f^* = 1.6$, second harmonic of the excitation frequency, f_p . Moreover, a “broadband noise” around the vortex shedding frequency as well as low frequency noise are present. In contrast, the spectrum obtained for the lock-in cases shown in Fig. 5.2(b) presents clearly the unique dominating frequency (and its second harmonic). It can be clearly seen that, as the motion frequency moves closer to the vortex shedding frequency, eventually these two frequencies coalesce (i.e. the vortex shedding frequency jumps onto the motion frequency).

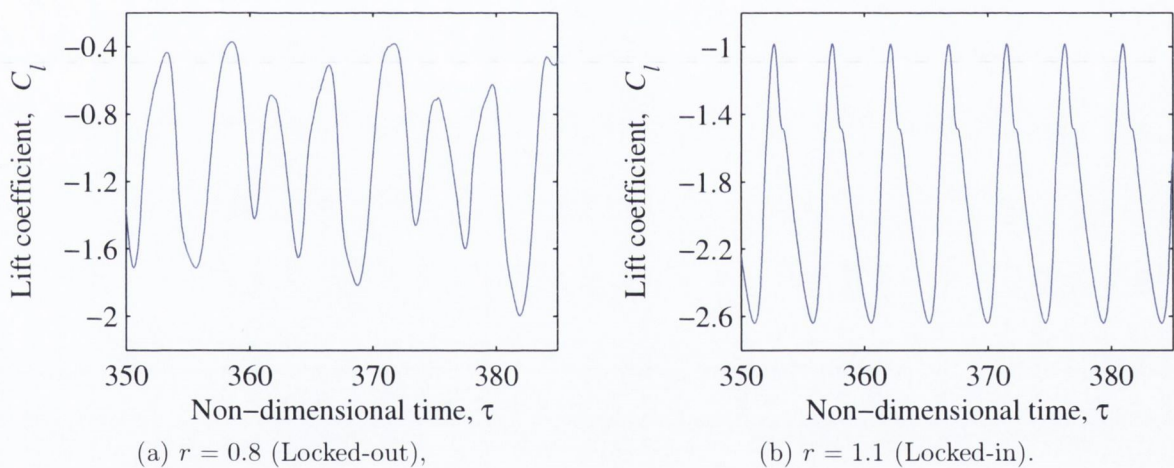


Figure 5.1: Detail of the time record of the lift force coefficient for pitching motion at $\alpha_{mean} = 140^\circ$ and different frequency ratios showing the effect of lock-out (a) and lock-in (b).

The lock-in behaviour of vortex shedding in the presence of pitching motion at $\alpha_{ampl} = 7^\circ$ can be summarised over the entire angle of attack and frequency ranges, shown in Fig. 5.3. The lock-in condition is present for the entire angle of attack range, but the range of frequencies depends strongly on angle. As can be clearly seen, the lock-in range is in general more significant when the airfoil presents a smaller characteristic length (vertical projected chord) i.e. in the regions around $\alpha_{mean} = 40^\circ$ and $\alpha_{mean} = 140^\circ$. Note that these incidence boundaries ($\alpha = 40^\circ$ and $\alpha = 140^\circ$) are directly related to the results for this particular CFD model set-up (see Chapter 4). Therefore they are not to

be considered as absolute lock-in references. The lock-in range in the incidence range ($50^\circ \leq \alpha_{mean} \leq 130^\circ$) is broadly constant.

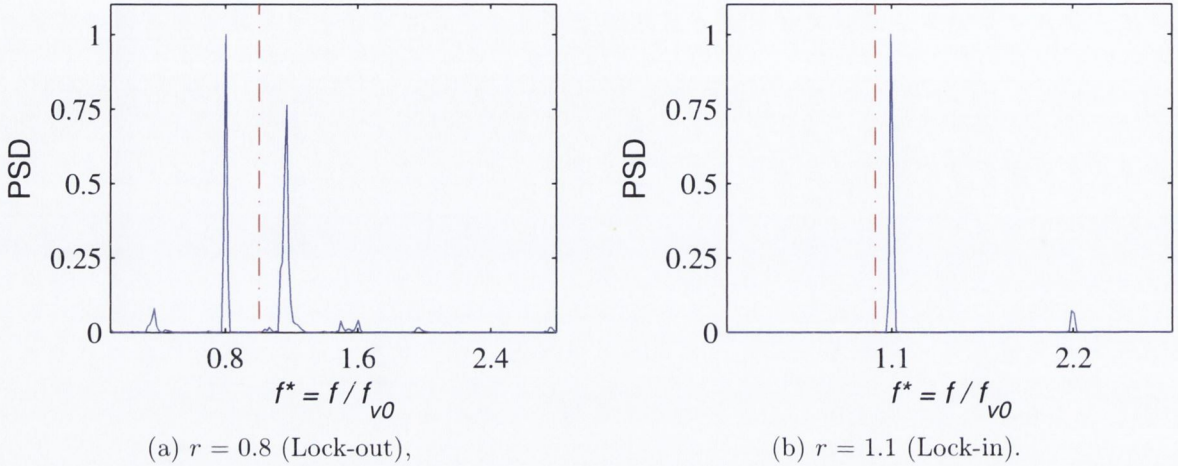


Figure 5.2: Spectrum of the lift force coefficient for pitching motion at $\alpha_{mean} = 140^\circ$ and different frequency ratios showing the effect of lock-out (a) and lock-in (b). PSD arbitrarily scaled. Dash-dot line indicates $f^* = 1$, corresponding to the static case.

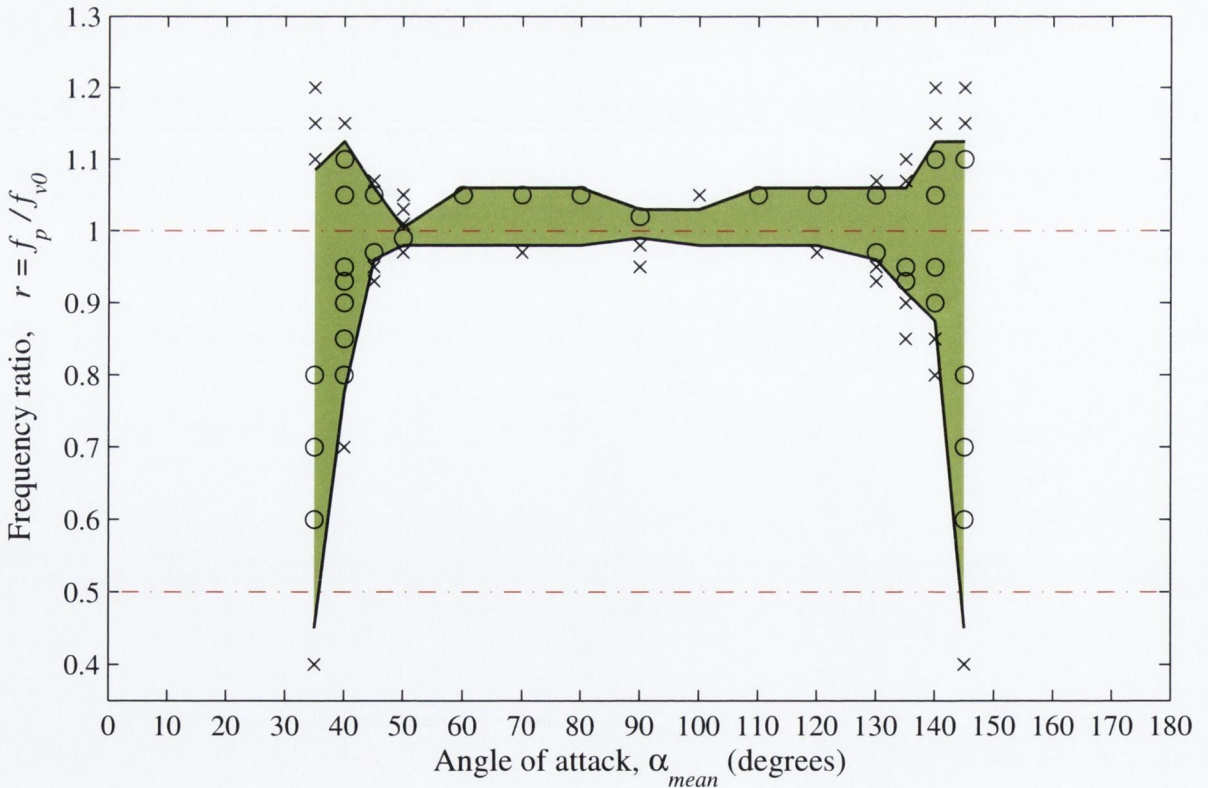
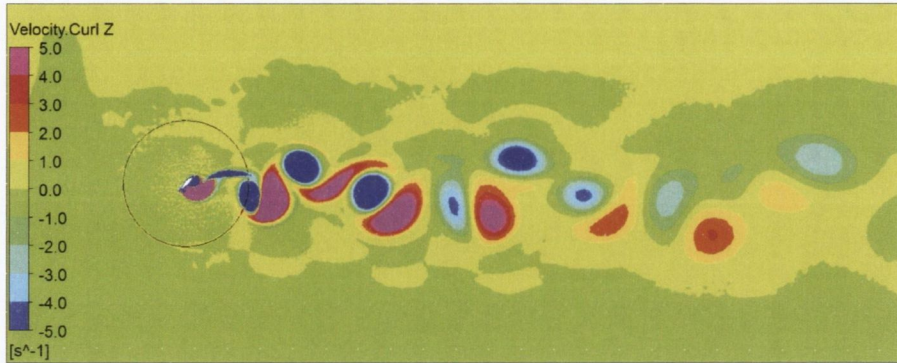


Figure 5.3: Synchronisation map for positive angles of attack, pitching motion at $\alpha_{ampl} = 7^\circ$: \circ , lock-in; \times , lock-out; \blacksquare , synchronisation region.

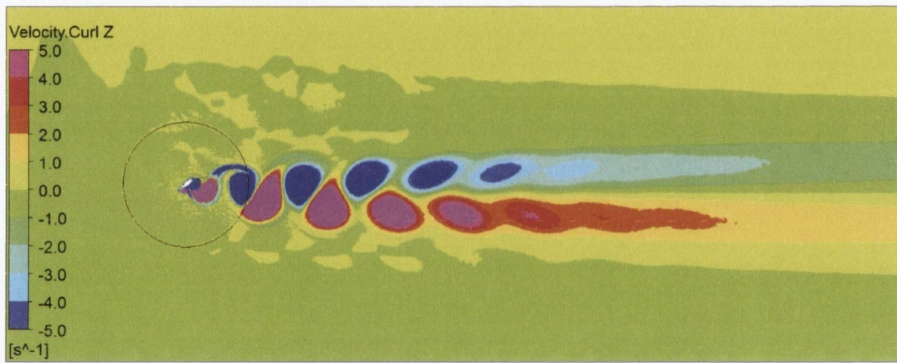
Generally, it is not clear why the wake should be more susceptible to synchronising at angles of attack with shallower characteristic length (Fig. 5.3), but it may be related to the overall structure of the wake before lock-in occurs. Fig. 5.4 shows the vortex street (i.e. instantaneous vorticity field) behind the airfoil for three different cases (two of them already considered above in Figs. 5.1 and 5.2). Consider the instantaneous vorticity field of two locked-out cases. Figure 5.4(c) shows the vorticity for an angle of attack, $\alpha_{mean} = 70^\circ$, and a frequency ratio, $r = 0.97$. The wake has arranged itself into an anti-symmetric configuration similar to the Kármán street often associated with periodic vortex shedding. This configuration is relatively stable, and so would be more resilient against external forcing and hence exhibits a narrower lock-in range. In this situation, the separation points (the leading and trailing edge of the airfoil) are almost at the same stream-wise location, as the blade is almost normal to the flow. In Fig. 5.4(a) the wake behind the airfoil at $\alpha_{mean} = 140^\circ$, $r = 0.8$ shows a different structure. The vortices have been formed and shed periodically, but they have partially paired, in a pattern reminiscent of the 2P mode. This may be due to fact that upstream separation point (i.e. the sharp trailing edge) is now 0.76 chord lengths upstream of the other separation point (i.e. the blunt leading edge). This configuration is less stable than the 2S mode. Once lock-in is established (e.g. $r = 1.1$) the wake structure becomes anti-symmetric as shown in Fig. 5.4(b).

The point made above, about the significantly different behaviour whether the airfoil position presents a smaller or larger characteristic length, can be explained with the help of Fig. 5.5. Two incidences, $\alpha_{mean} = 40^\circ$ with a smaller characteristic length and $\alpha_{mean} = 70^\circ$ with a larger one, are used to contrast how the flow differently reattaches on the leading edge during the down-stroke pitching motion. Figure 5.5(a) shows the instantaneous horizontal velocity for $\alpha_{mean} = 40^\circ$ at its maximum pitching position, while Fig. 5.5(b) at its minimum one (for $\alpha_{ampl} = 7^\circ$). It can be seen that the down-stroke motion causes the reattachment point of the flow to move substantially on the upper surface. This leads to a reduction of the effective characteristic length of the airfoil. Conversely, for $\alpha_{mean} = 70^\circ$, Figs. 5.5(c) and 5.5(d) show that the reattachment point does not move significantly comparing the upper (Fig. 5.5(c)) and the lower (Fig. 5.5(d)) pitching positions. This is consistent with what was observed in Figs. 5.3 and 5.4, i.e. the more resilient wake for

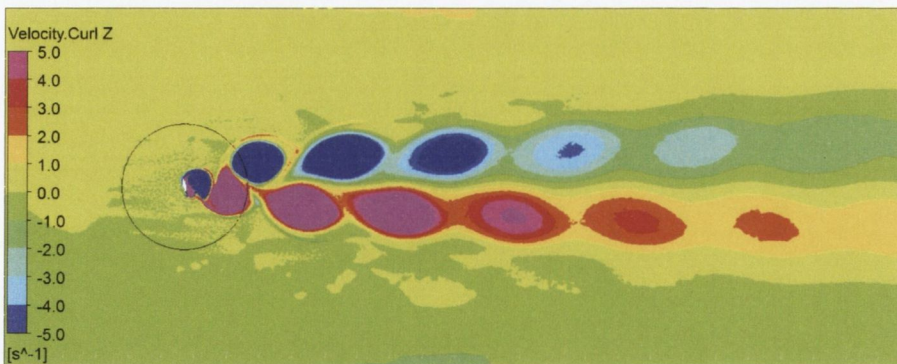
$\alpha_{mean} = 70^\circ$ as well as its two separation points being almost at the same stream-wise location.



(a) $\alpha_{mean} = 140^\circ$; frequency ratio, $r = 0.8$. Vortex shedding locked-out,



(b) $\alpha_{mean} = 140^\circ$; frequency ratio, $r = 1.1$. Vortex shedding locked-in,



(c) $\alpha_{mean} = 70^\circ$; frequency ratio, $r = 0.97$. Vortex shedding locked-out.

Figure 5.4: Instantaneous vorticity field for pitching motion at different conditions, $\alpha_{mean} = 140^\circ$ (a, b) and $\alpha_{mean} = 70^\circ$ (c). ■, counter-clockwise (positive) vorticity; ■, clockwise (negative) vorticity.

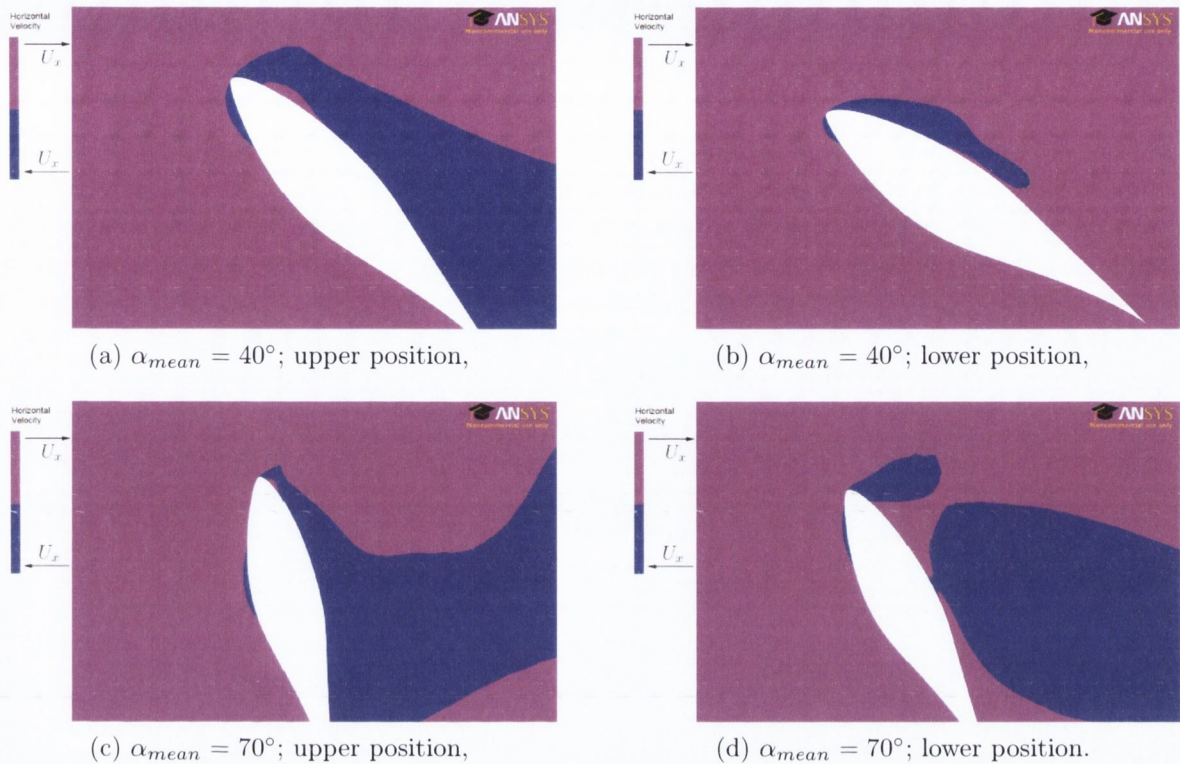


Figure 5.5: Instantaneous horizontal velocity showing the flow reattachment point on the leading edge for $\alpha_{mean} = 40^\circ$ (a, b) and $\alpha_{mean} = 70^\circ$ (c, d) on their max and min pitching position ($\alpha_{ampl} = 7^\circ$). ■, flow velocity left-to-right; ■, flow velocity right-to-left.

5.1.2 Pitching amplitude effect

The effect of the pitching amplitude on the lock-in around $r = 1$ has been assessed for angles $\alpha_{mean} = 40^\circ$ and $\alpha_{mean} = 140^\circ$, for which the synchronisation region are shown respectively in Figs. 5.6(a) and 5.6(b). These two incidences are considered throughout this work as they appeared significant for the results coming from the used model. Also, as the characteristic length is relatively small, such a scenario may be the closest to a real case. As expected, the extent of the frequency lock-in range decreases if the oscillation amplitude is reduced. Moreover, the synchronisation region is broadly smaller for $\alpha_{mean} = 140^\circ$: this suggests that a sharp trailing edge in the upstream position seems to slightly reduce the risk of lock-in, consistent with findings in the literature (see Chapter 2). For both cases, it can be seen that the lock-in behaviour is not symmetric about the natural shedding frequency ($r = 1$). This is consistent with findings of Besem *et al.* [87].

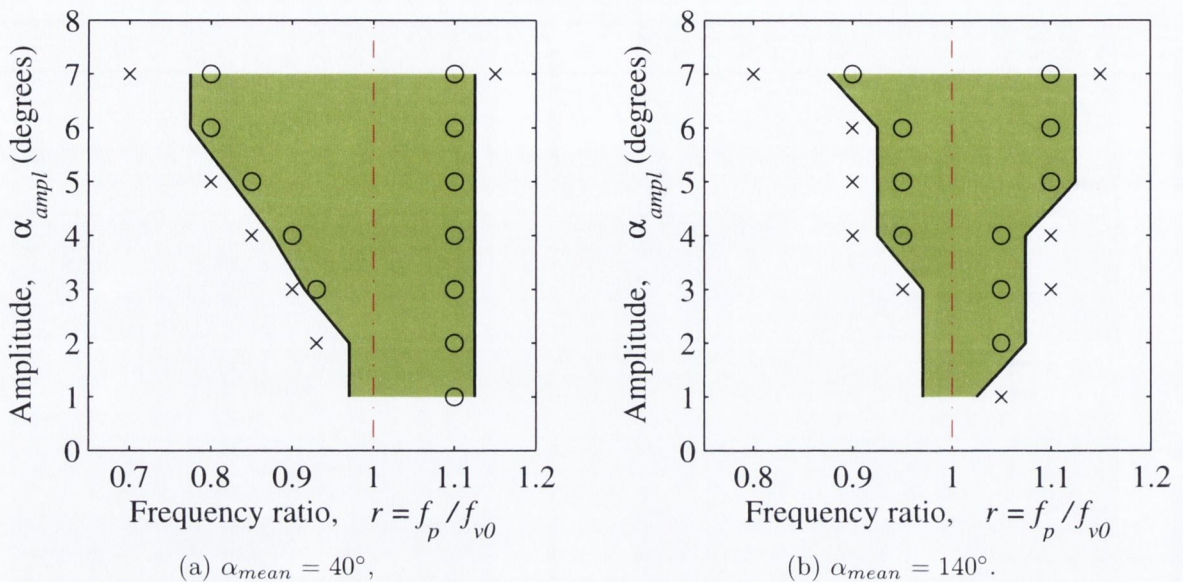


Figure 5.6: Synchronisation region for pitching amplitude effect at two incidences: \circ , lock-in; \times , lock-out; \blacksquare , synchronisation region.

5.2 Stream-wise oscillation motion

A series of two-dimensional unsteady simulations of the flow around the NREL S809 airfoil moving in the stream-wise direction (x), have been performed, at first for one oscillation amplitude only, $A_s = 0.25c$, for a range of frequency ratios around $r = 1$, $r = 0.5$ and $r = 2$. This amplitude value chosen is considered primarily to investigate the lock-in behaviour of the oscillating airfoil in stream-wise motion from a generic research perspective. For the stream-wise motion, the frequency ratio, r , is defined by the stream-wise frequency, f_s , as follows:

$$r = \frac{f_s}{f_{v0}} \quad (5.5)$$

In addition, the effect of the stream-wise amplitude has been examined for angular positions at which the synchronisation appears to be more significant.

For translational motions, a deforming mesh approach has been used. As the oscillation amplitude is quite significant with respect to the chord length, the fluid domain has been slightly modified in order to allow a smoother mesh deformation (see Fig. 5.7) for

a less time-expensive computation. The overall mesh density remains the same. The difference with the previous mesh used for the static and the pitching case, is that the circle (inner fluid domain) is placed within a rectangular box which is put in motion. The mesh elements around the rectangular box will be deformed according to the ANSYS Fluent[®] deforming mesh algorithm. The translational stream-wise motion has been applied via a compiled User Defined Function (UDF). The motion law is described in Eq. 5.6:

$$x(t) = A_s \sin(2\pi f_s t) \quad (5.6)$$

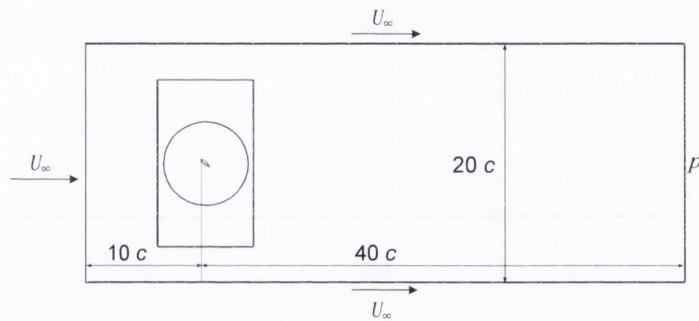


Figure 5.7: Flow field domain for translational motion; dimensions and boundary conditions.

5.2.1 Synchronisation at fixed stream-wise amplitude

In order to demonstrate the effect lock-in has on the vortex shedding excitation that would be experienced by the blade section, the behaviour of the lift coefficient at $\alpha_{mean} = 140^\circ$ is considered. The sample choice fell on the $\alpha_{mean} = 140^\circ$ configuration since at this incidence synchronisation occurs with both first and second harmonic of the motion frequency, f_s .

Figure 5.8 shows portions of the time record of the lift coefficient with the relative spectra, for three frequency ratios, in order to compare different behaviours happening around the “reference” frequency ratios considered ($r = 1$, $r = 0.5$, $r = 2$). The lock-out condition is not considered as it has been presented already (in Section 5.1), as well as the general lock-in behaviour in details. For the sake of clarity, only 3 seconds of simulated time are shown, after the wake has well developed. Time is expressed dimensionless. Frequencies have been normalised with the static vortex shedding frequency,

giving a non-dimensional frequency: $f^* = f/f_{v0}$. At a frequency ratio $r = 0.9$ the vortex shedding frequency is locked-in to the first harmonic of excitation: Fig. 5.8(a) shows the lift coefficient time trace which is periodic with a dominant frequency. This dominant frequency can be clearly seen in Fig. 5.8(b) at $f^* = 0.9$, where also higher harmonics are present (smaller peaks at $f^* = 1.8$ and $f^* = 2.7$). A vortex shedding frequency at $f^* = 1$ (highlighted by a dash-dot line as a reference) would occur if the airfoil was static. Figures 5.8(c) and 5.8(d) show respectively the time trace and the spectrum of the case of lock-in to the second harmonic of excitation, for $r = 0.55$. It can be seen that the second harmonic is dominant over the odd ones, at $f^* = 1.1$. Figures 5.8(e) and 5.8(f) show the case of $r = 2.1$, which means that the motion frequency is around twice the static vortex shedding frequency. This behaviour may be addressed as pseudo-lock-in. The time trace of the lift coefficient is clearly periodic, usually associated with the lock-in case. But the frequency content presents also a sub-harmonic, at $f^* = 1.05$ (half of the motion frequency) and a peak at $3/2f_s$ ($3/2$ of the motion frequency) which invalidates the criterion adopted for the lock-in assessment. Nonetheless, the vortex shedding frequency and the excitation frequency appear to be coalesced; therefore it would not make sense to call it locked-out, hence the “pseudo” label.

Figure 5.9 shows the vortex street (i.e. instantaneous vorticity field) behind the airfoil for the three different cases considered above (Fig. 5.8), at $\alpha_{mean} = 140^\circ$. The wake synchronised to the first harmonic of the motion frequency is shown in Fig. 5.9(a): the vortex street is well organised in an anti-symmetric structure. This is due to the action of a strongly dominant frequency, as the vortex shedding and the motion frequencies coalesce. As a comparison, the effect of the synchronisation to the second harmonic of motion frequency can be seen in Fig. 5.9(b), where the wake is still periodic but couples of vortices seem grouping together rather than forming a uniform lined-up vortex street. This is due to the second harmonic dominating over the odd ones (see Fig. 5.8(d)). Figure 5.9(c) shows a well organised vortex street for $r = 2.1$ too, due to the periodicity of the lift coefficient and to the highly dominating frequency which corresponds to the apparently coalesced vortex shedding and motion frequencies (Fig. 5.8(f)).

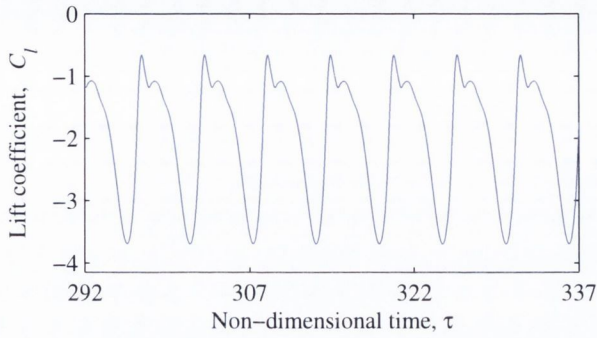
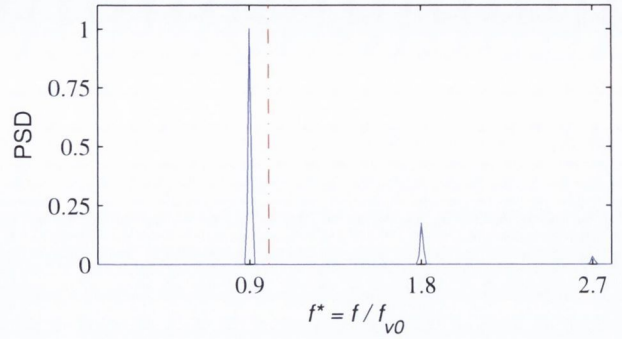
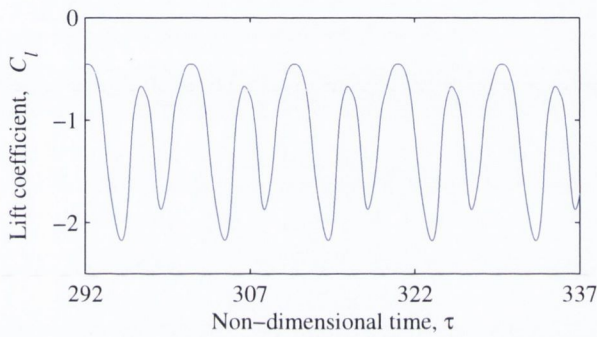
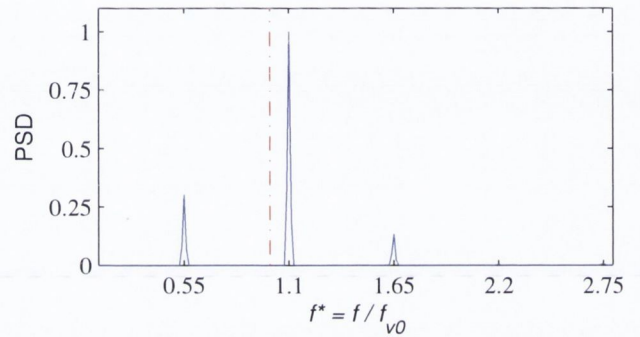
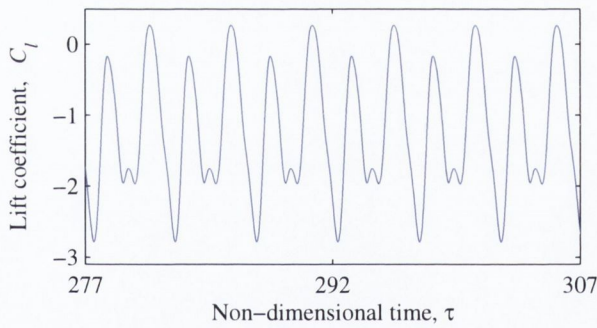
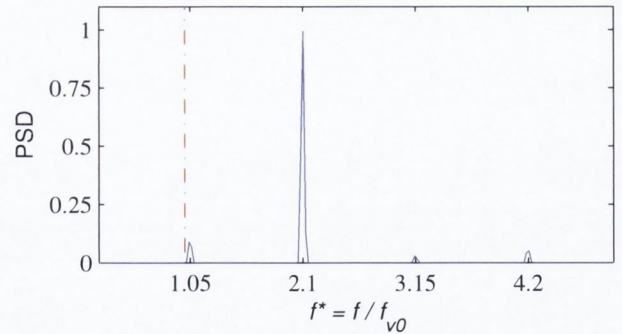
(a) $r = 0.9$ (Lock-in to the 1st harmonic),(b) $r = 0.9$ (Lock-in to the 1st harmonic),(c) $r = 0.55$ (Lock-in to the 2nd harmonic),(d) $r = 0.55$ (Lock-in to the 2nd harmonic),(e) $r = 2.1$ (Pseudo-lock-in; periodicity),(f) $r = 2.1$ (Pseudo-lock-in; with sub-harmonic).

Figure 5.8: Detail of the time record (a, c, e) and spectrum (b, d, f) of the lift force coefficient for stream-wise motion at $\alpha_{mean} = 140^\circ$ and different frequency ratios. PSD arbitrarily scaled. Dash-dot line indicates $f^* = 1$, corresponding to the static case.

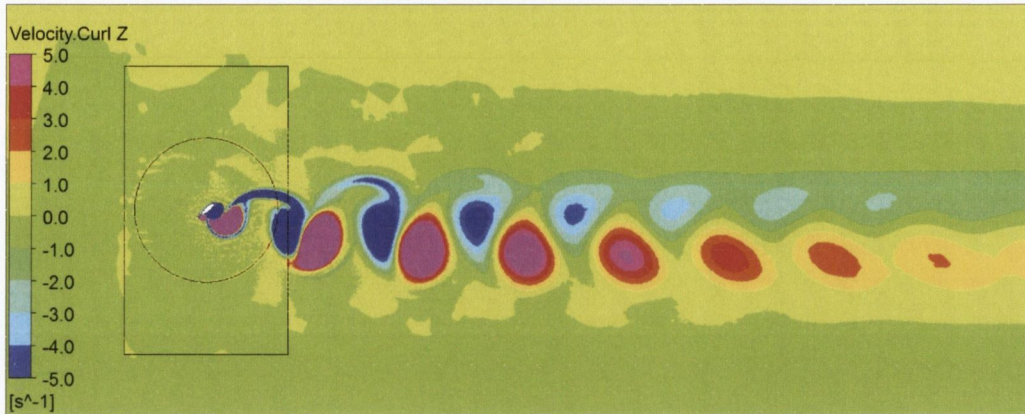
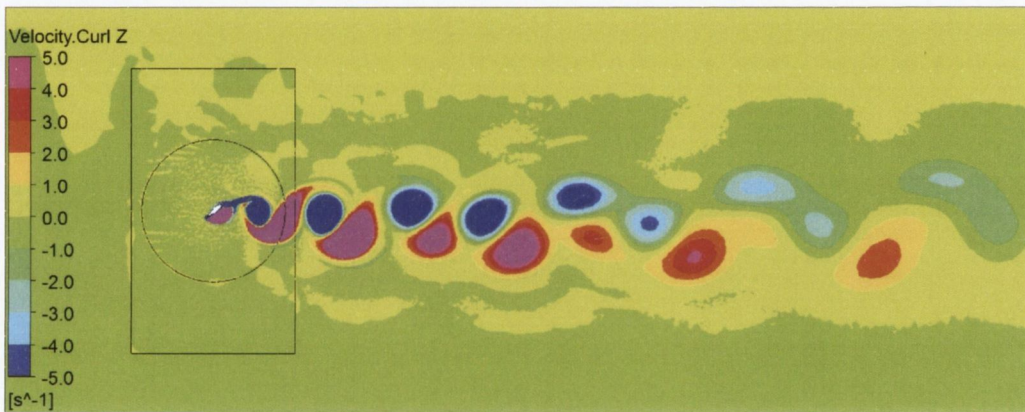
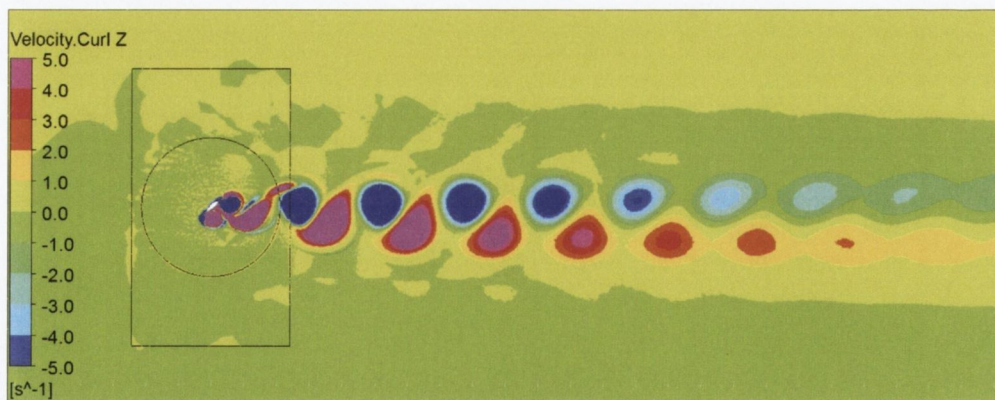
(a) $\alpha_{mean} = 140^\circ$; $r = 0.9$. Locked-in to the 1st harmonic of excitation,(b) $\alpha_{mean} = 140^\circ$; $r = 0.55$. Locked-in to the 2nd harmonic of excitation,(c) $\alpha_{mean} = 140^\circ$; $r = 2.1$. Pseudo lock-in with sub-harmonics.

Figure 5.9: Instantaneous vorticity field for stream-wise motion at different conditions, $\alpha_{mean} = 140^\circ$. ■, counter-clockwise (positive) vorticity; ■, clockwise (negative) vorticity.

The lock-in behaviour of vortex-shedding in the presence of stream-wise translating motion at $A_s = 0.25c$ are summarised in Fig. 5.10. The synchronisation regions over the entire angle of attack and frequency ranges are presented in different colors indicating

whether the vortex shedding frequency has locked-in to the first or to the second harmonic of the motion frequency (area between $r = 1$ and $r = 0.5$), or indicating the presence of sub-harmonics (area around $r = 2$), leading to a pseudo-lock-in condition. The lock-in condition is not present for the entire incidence range. As can be clearly seen, synchronisation to the first harmonic occurs when the airfoil presents a smaller characteristic length, i.e. in a range around $\alpha_{mean} = 40^\circ$ and $\alpha_{mean} = 140^\circ$. What is observed for $\alpha_{mean} = 35^\circ$, $\alpha_{mean} = 40^\circ$, $\alpha_{mean} = 45^\circ$, $\alpha_{mean} = 145^\circ$ was unexpected. That is, lock-in takes place for a frequency ratio range which does not extend to $r = 1$: in fact, lock-in does not occur in the vicinity of $r = 1$. Though, this behaviour is not consistent for all the angular positions. Regarding the lock-in condition to the second harmonic of excitation, the synchronisation region is limited to a very narrow frequency ratio close to $r = 0.5$, involving only few angles of attack with the trailing edge in the upwind position, and the extreme case of vertical position to the flow direction. What is suggested, is that the second harmonic synchronisation occurs when the upwind separation point is well defined. A discontinuity on this behaviour is present at $\alpha_{mean} = 130^\circ$; this may be just a peculiar result of the non-linear interaction between the fluid and the moving body.

The region which seems to be more prone to synchronisation is the one around $r = 2$, and this is consistent with findings in the literature about stream-wise VIV (see Chapter 2). This region is concentrated in a small range of incidences, $70^\circ \leq \alpha_{mean} \leq 110^\circ$, i.e. when the airfoil is almost vertical to the flow direction (the characteristic length is around its maximum). As per Figs. 5.8(e) and 5.8(f), this region is not characterised by a usual lock-in condition, albeit periodicity of the lift coefficient is present and synchronisation of the vortex shedding with the motion frequency appears to occur. For $r = 2.1$, this pseudo-lock-in condition extends to $\alpha_{mean} = 140^\circ$. A discontinuity is present for $\alpha_{mean} = 130^\circ$, again, as in the case of $r = 0.5$ mentioned above. This may confirm the fact that at this incidence some particular non-linear fluid-body interaction occurs. Furthermore, $\alpha_{mean} = 130^\circ$ is the specular incidence of $\alpha_{mean} = 50^\circ$ with respect to the vertical position to the flow ($\alpha_{mean} = 90^\circ$). In Chapter 4 has been mentioned already that $\alpha_{mean} = 50^\circ$ is a particular incidence, since a dramatic change in behaviour has been observed between $\alpha_{mean} = 40^\circ$ and $\alpha_{mean} = 50^\circ$, for the static airfoil case. It can be seen that this is true also for the moving case (Figs. 5.3, 5.10).

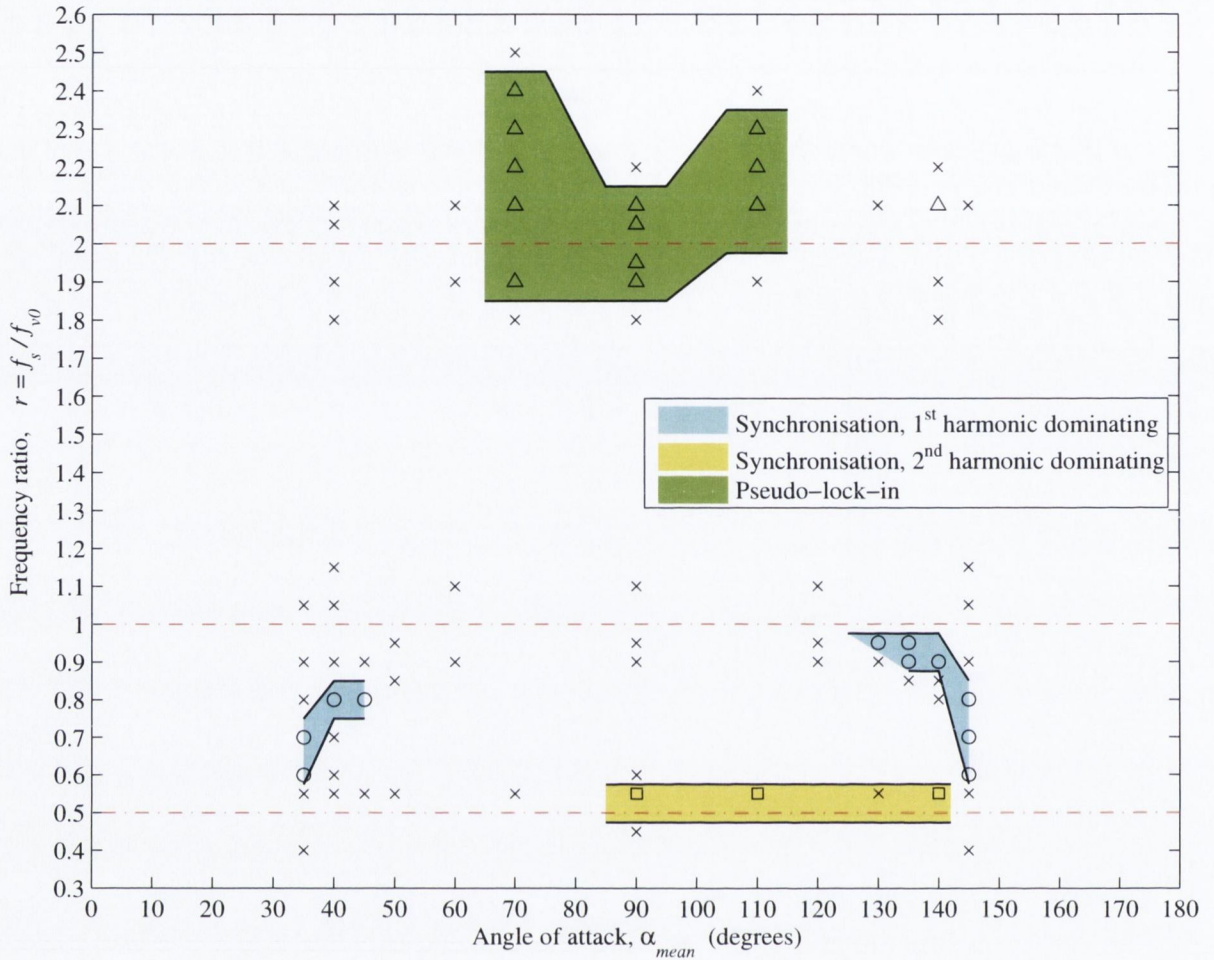


Figure 5.10: Synchronisation map for positive angles of attack, stream-wise motion at $A_s = 0.25c$: \circ , lock-in to the first harmonic of excitation; \square , lock-in to the second harmonic of excitation; \triangle , pseudo-lock-in (periodicity with sub-harmonics); \times , lock-out.

5.2.2 Stream-wise amplitude effect

The effect of the oscillation amplitude on the lock-in has been assessed for angles $\alpha_{mean} = 40^\circ$ and $\alpha_{mean} = 140^\circ$, around $r = 1$, for which the synchronisation boundaries are proposed respectively in Figs. 5.11(a) and 5.11(b). The purpose of this analysis is twofold: 1) actually investigate the amplitude effect, 2) try to explain the unexpected lock-out behaviour seen in Fig. 5.10 for some incidences close to $r = 1$.

It would be expected that the extent of the frequency lock-in range increases if the oscillation amplitude is augmented. Instead, results showed in Fig. 5.11(a) do not always match the expected behaviour typical of generic bluff bodies. In fact, it seems that, for some cases, increasing the motion amplitude will lead to lock-in suppression. Now, let us

compare Figs. 5.11(a) and Fig. 5.11(b). First of all it can be seen that these two cases present different synchronisation boundaries. For $\alpha_{mean} = 140^\circ$ a larger amplitude (with respect to $\alpha_{mean} = 40^\circ$) is sufficient to achieve a lock-out condition within a frequency range very close to $r = 1$. Moreover, the overall extent of the frequency ratio lock-in range is smaller at every amplitude considered. This different behaviour between $\alpha_{mean} = 40^\circ$ and $\alpha_{mean} = 140^\circ$ could be attributed to: 1) different camber and 2) different shape of the upwind edge (round or sharp). To eliminate one of these two options, the amplitude effect assessment has been conducted also for $\alpha_{mean} = -40^\circ$, presented in Fig. 5.11(c). It can be seen that the behaviour is identical to the case of $\alpha_{mean} = 40^\circ$ (Fig. 5.11(a)), meaning that the different camber is not much significant on this matter. Therefore, this suggests that a sharp leading edge (i.e. upwind well defined separation point for $\alpha_{mean} = 140^\circ$) affects the lock-in behaviour, reducing the risk of synchronisation (consistent with findings present in the literature). In general, note that an increase in motion amplitude does not change the overall behaviour on the post-coincidence region ($r > 1$), which remains always not synchronised.

Regarding the unexpected lock-out behaviour seen in Fig. 5.10 for some incidences close to $r = 1$, Fig. 5.11(a) may help to explain that. Or at least, the behaviour appears consistent for such order of magnitude amplitudes. Thus, it may be useful to compare two amplitudes, $A_s = 0.0625c$ (lock-in case) and $A_s = 0.5c$ (lock-out case) at the same incidence $\alpha_{mean} = 40^\circ$ and same frequency ratio $r = 0.9$. Figure 5.12 shows the instantaneous vorticity field over an oscillation cycle for these two cases; the freestream velocity sense is from left to right. The main feature to point out is that for $A_s = 0.0625c$ the leading edge vortex forms, elongates, and eventually detaches when the opposite trailing edge vortex forms and dominates the near wake region (following the conventional behaviour of generic bluff bodies). For $A_s = 0.5c$ instead, when the airfoil is moving in the same sense of the stream ($0^\circ < \phi < 90^\circ$), the leading edge vortex appears to remain over the airfoil (i.e. the airfoil keeps up with the formed vortex). This different behaviour is due to the path travelled by the airfoil in the direction of the convection stream, which does not allow the vortex to actually detach. The vortex separation occurs thanks to the path in the sense downstream-to-upstream ($-x$, opposite to the freestream direction). It seems that this unusual behaviour leads to lock-out as amplitude is increased.

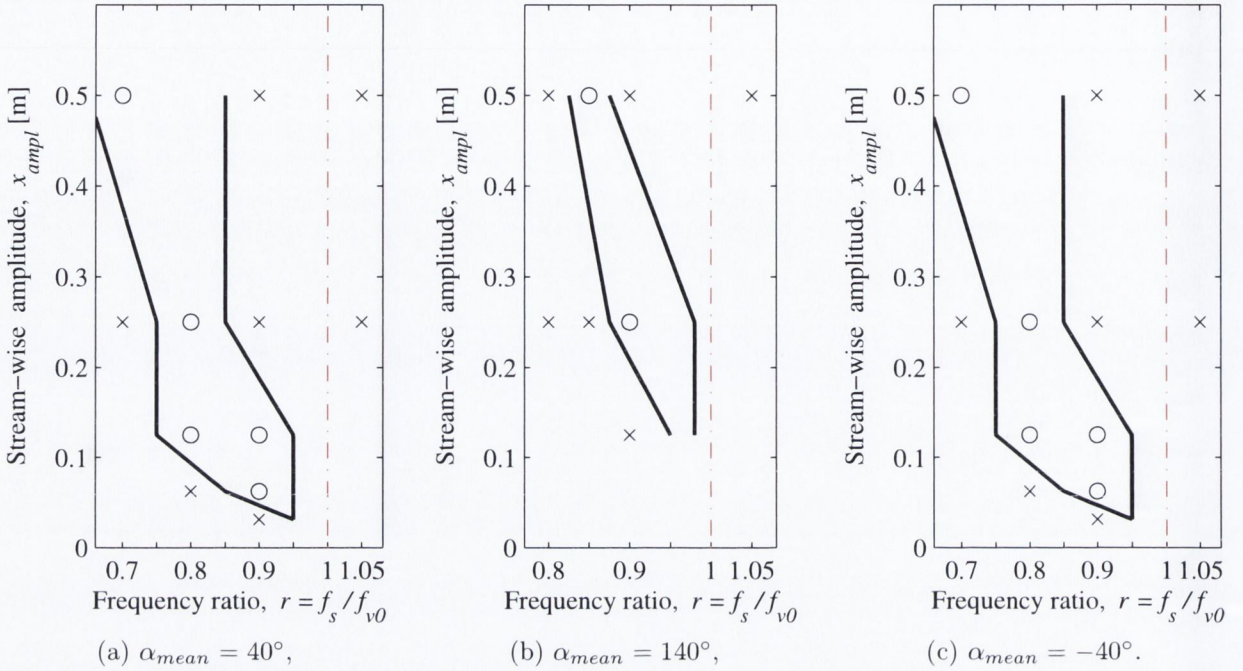


Figure 5.11: Proposed synchronisation boundaries for stream-wise motion amplitude effect at three incidences: o, lock-in; x, lock-out.

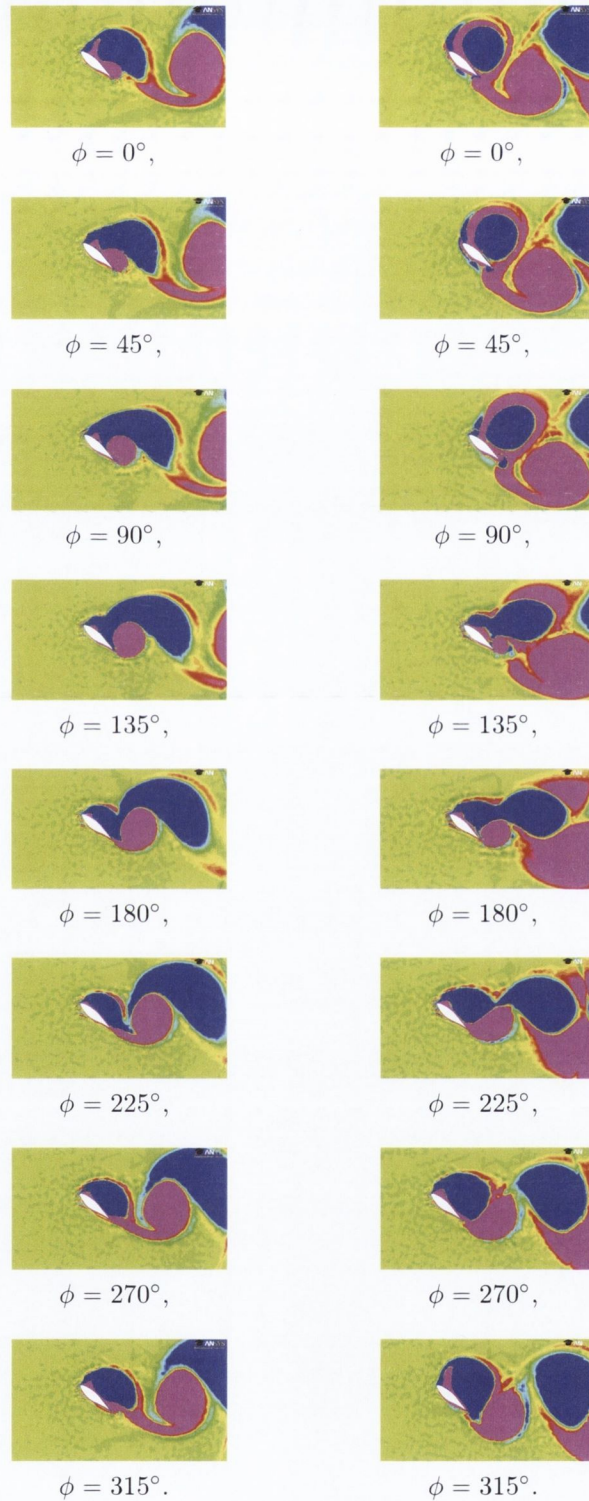


Figure 5.12: Close-up of the instantaneous vorticity field over an oscillation cycle at $\alpha_{mean} = 40^\circ$, $r = 0.9$. Stream-wise amplitude effect comparison: left column, $A_s = 0.00625c$ (lock-in); right column, $A_s = 0.5c$ (lock-out). ■, counter-clockwise (positive) vorticity; ■, clockwise (negative) vorticity.

5.3 Transverse oscillation motion

A series of two-dimensional unsteady simulations of the flow around the NREL S809 airfoil moving in the transverse direction (y), have been performed, at first for one oscillation amplitude only, $A_t = 0.25c$, for a range of frequency ratios around $r = 1$. This amplitude value has been chosen arbitrarily, appearing reasonable for the purpose of this study, which is not industry-oriented. The aim is to investigate the lock-in behaviour of the oscillating airfoil in transverse motion from a generic research perspective. Also, it is consistent with the amplitude used for the stream-wise motion study. For the transverse motion, the frequency ratio, r , is defined by the transverse frequency, f_t , as follows:

$$r = \frac{f_t}{f_{v0}} \quad (5.7)$$

In addition, the effect of the transverse amplitude has been examined for angular positions at which the synchronisation appears to be more significant.

The fluid domain is the same used for the stream-wise motion (Fig. 5.7), as well as the deforming mesh approach. The motion law applied via a compiled User Defined Function (UDF) is described in Eq. 5.8:

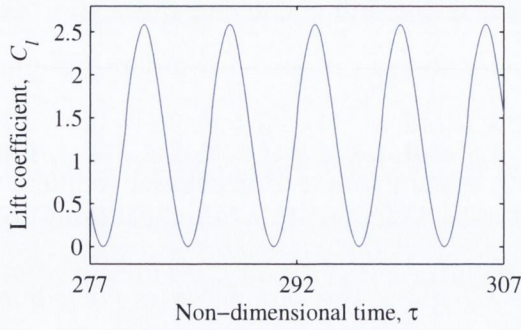
$$y(t) = A_t \sin(2\pi f_t t) \quad (5.8)$$

5.3.1 Synchronisation at fixed transverse amplitude

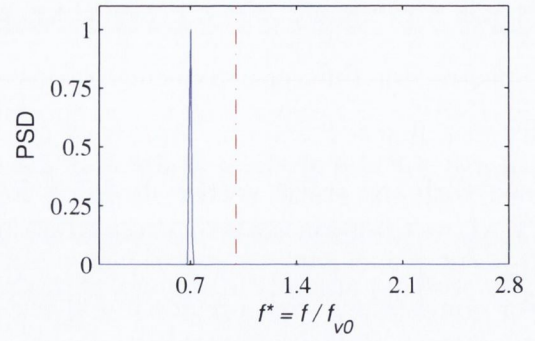
As done in Sections 5.1 and 5.2 for the pitching and stream-wise motions, different cases are presented to show different vortex shedding behaviours for the transverse motion of the airfoil. In Section 5.1 for the pitching motion, the lock-in and the lock-out have been presented. In Section 5.2 for the stream-wise motion, a new behaviour has been introduced, the pseudo-lock-in (lift coefficient periodicity with sub-harmonics). In this Section for the transverse motion, another behaviour is introduced for some incidences (at relatively shallow characteristic length) and frequency ratios, here named as “transitional behaviour”.

Figure 5.13 shows portions of the time record of the lift coefficient with the relative spectra, for different frequency ratios and incidences, in order to compare different vortex shedding behaviours. Time is expressed dimensionless. Frequencies have been normalised with the static vortex shedding frequency, giving a non-dimensional frequency: $f^* = f/f_{v0}$.

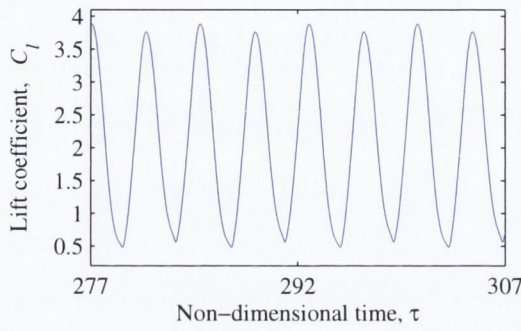
For consistency with previous analysis in this Chapter, the sample cases considered are again $\alpha_{mean} = 40^\circ$ or $\alpha_{mean} = 140^\circ$. For $\alpha_{mean} = 40^\circ$ at a frequency ratio $r = 0.7$ the vortex shedding frequency is clearly locked-in: Fig. 5.13(a) shows the periodic lift coefficient time trace, with its relative spectrum (Fig. 5.13(b)). A pseudo lock-in condition, already introduced in Section 5.2, for $\alpha_{mean} = 40^\circ$ at $r = 1.1$ is presented in Fig. 5.13(c) showing the periodic lift coefficient time trace and in Fig. 5.13(d) showing the relative spectrum. The logarithmic scale for the y axis has been used to facilitate the visualization of the sub-harmonic, at $f^* = 0.55$. The dominant frequency appears to correspond to the motion and vortex shedding frequencies coalesced, at $f^* = 1.1$. Increasing the frequency ratio at $r = 1.2$ (for $\alpha_{mean} = 40^\circ$), an unexpected behaviour has been observed. Figure 5.13(e) shows the time trace of the lift coefficient: it is not periodic. But it can be said that, periodically, there is a cycle where no positive vorticity is shed (with a negative value more accentuated). It seems indeed an odd behaviour, and will be discussed further under other views, explaining why it has been addressed as “transitional”. For this case, in Fig. 5.13(f) two peaks can be seen (again in logarithmic scale for the sake of clarity), first and second harmonic of the motion frequency, along with a “broad-band noise”. The pseudo-lock-in condition illustrated in Figs. 5.13(c) and 5.13(d) is compared to another pseudo-lock-in case in Figs. 5.13(g) and 5.13(h) for a different angle of attack, $\alpha_{mean} = 140^\circ$, at $r = 0.7$. It can be seen that the time trace of the lift coefficient in Fig. 5.13(g) still presents a periodic pattern, yet with a more significant harmonic content than the case shown in Fig. 5.13(c). The relative spectrum in Fig. 5.13(h) in fact, shows a dominant peak at $f^* = 1.05$, which is $3/2f_t$. This is the main difference compared to Fig. 5.13(d), where the dominant peak is the actual f_t , that makes appear the time traces of the lift coefficient so different (Figs. 5.13(c) and 5.13(g)).



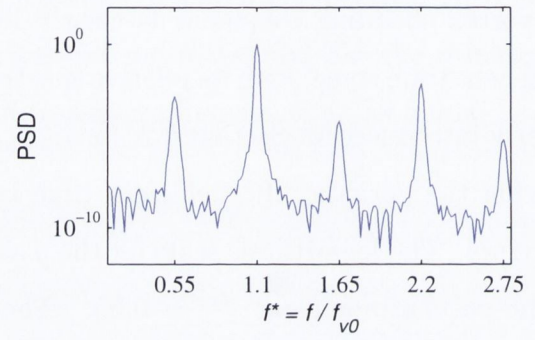
(a) $r = 0.7$ (Lock-in),



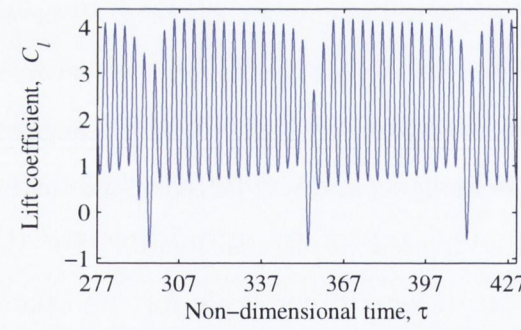
(b) $r = 0.7$ (Lock-in),



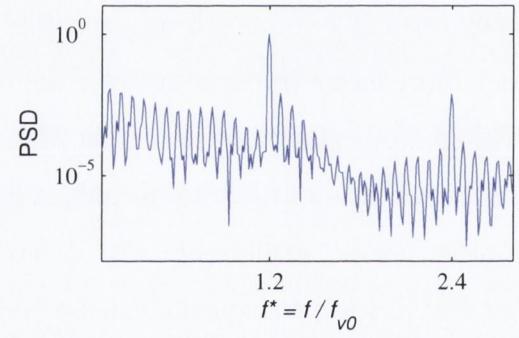
(c) $r = 1.1$ (Pseudo-lock-in; periodicity),



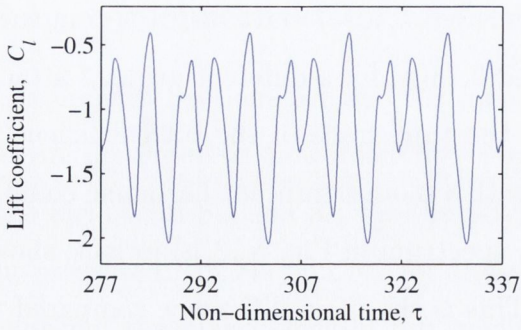
(d) $r = 1.1$ (Pseudo-lock-in; sub-harmonic),



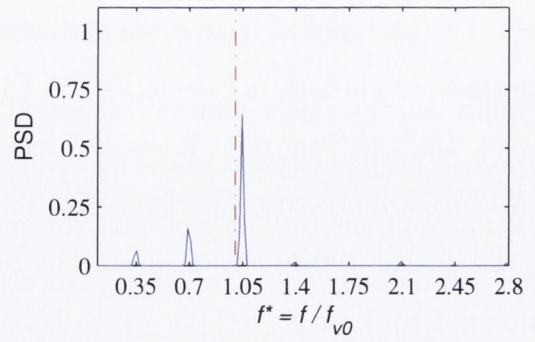
(e) $r = 1.2$ ("Transitional behaviour").



(f) $r = 1.2$ ("Broad-band noise").



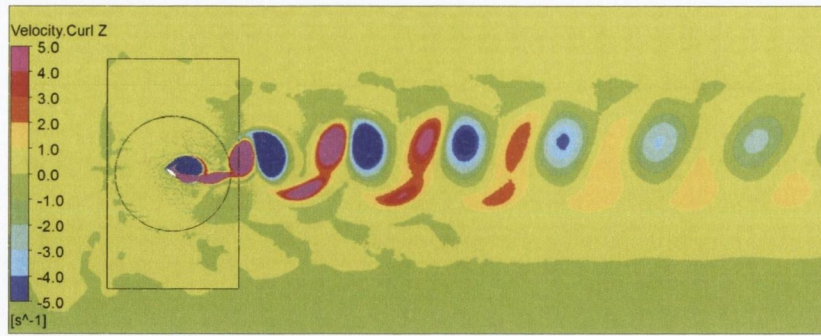
(g) $r = 0.7$ (Pseudo-lock-in; periodicity).



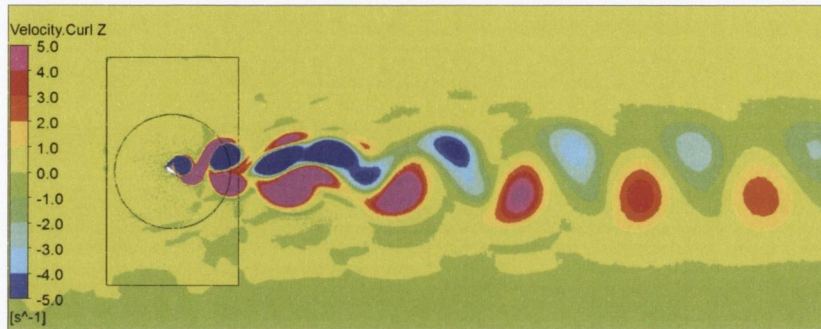
(h) $r = 0.7$ (Pseudo-lock-in; sub-harmonic).

Figure 5.13: Detail of the time record (a, c, e, g) and spectrum (b, d, f, h) of the lift force coefficient for transverse motion at $\alpha_{mean} = 40^\circ$ (a, b, c, d, e, f) and at $\alpha_{mean} = 140^\circ$ (g, h); different frequency ratios. PSD arbitrarily scaled, logarithmic for (d, f). Dash-dot line indicates $f^* = 1$, corresponding to the static case.

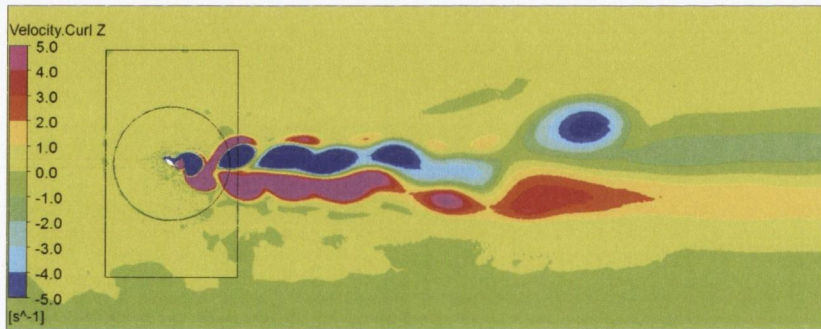
These four cases are illustrated in Fig. 5.14, showing the vortex street behind the translating airfoil. The lock-in condition is shown in Fig. 5.14(a) with a well organised wake. The counter-clockwise (positive) vortex per cycle is actually formed by two vortices. This is illustrated in Fig. 5.15 over an oscillation cycle; the freestream velocity sense is from left to right. It can be seen that after the counter-clockwise (positive) vortex is formed, it does not detach as it would expect. The downward vertical motion of the trailing edge keeps the vortex attached and causes a sort of elongation. Eventually, this elongation is cut by the counter-vorticity of the clock-wise (negative) vortex (Fig. 5.15(b)) letting the vortex to detach completely. As the vortex travels further, the viscous dissipation separates the elongated counter-clockwise vortex into two distinct vortices, hence appearing as a pair. Figure 5.14(b) shows the wake of the pseudo-lock-in case for $\alpha_{mean} = 40^\circ$ at $r = 1.1$. The presence of frequencies which are non integer multiples of f_t prevents the wake being organised, but in the far field a periodic vortices appears to occur, due to the dominant frequency which corresponds to the motion one (see Fig. 5.13(d)). As previously presented, this could lead to a pseudo-lock-in condition. At $r = 1.2$ the “transitional behaviour” wake is shown in Fig. 5.14(c). It can be seen that, for few cycles, the vortices of the two streets are almost blended together. Figure 5.14(d) shows the wake for the other pseudo-lock-in case ($\alpha_{mean} = 140^\circ$ at $r = 0.7$), to be compared with Fig. 5.14(b). These are both pseudo-lock-in conditions, but the wake structures are quite different, being the one in Fig. 5.14(d) not organised, resembling a lock-out condition. This difference can be explained with Figs. 5.13(d) and 5.13(h). The disorganisation of the wake in Fig. 5.14(d) is the effect of the dominant frequency which is $3/2f_t$, i.e. a non integer multiple of f_t (Fig. 5.13(h)).



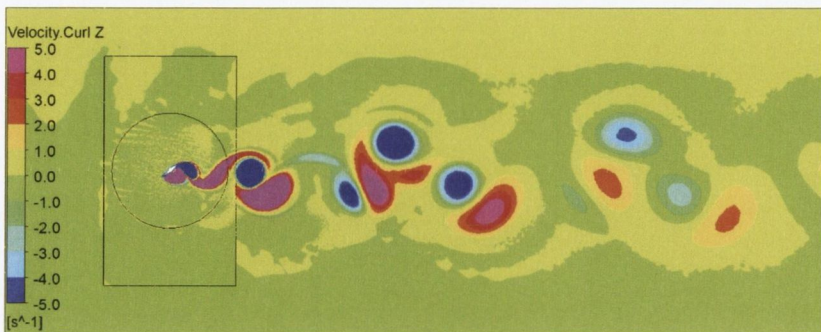
(a) $\alpha_{mean} = 40^\circ$; $r = 0.7$. Lock-in,



(b) $\alpha_{mean} = 40^\circ$; $r = 1.1$. Pseudo-lock-in with sub-harmonics,



(c) $\alpha_{mean} = 40^\circ$; $r = 1.2$. "Transitional behaviour",



(d) $\alpha_{mean} = 140^\circ$; $r = 0.7$. Pseudo-lock-in with sub-harmonics.

Figure 5.14: Instantaneous vorticity field for transverse motion at different conditions, $\alpha_{mean} = 40^\circ$ (a, b, c) and $\alpha_{mean} = 140^\circ$ (d). ■, counter-clockwise (positive) vorticity; ■, clockwise (negative) vorticity.

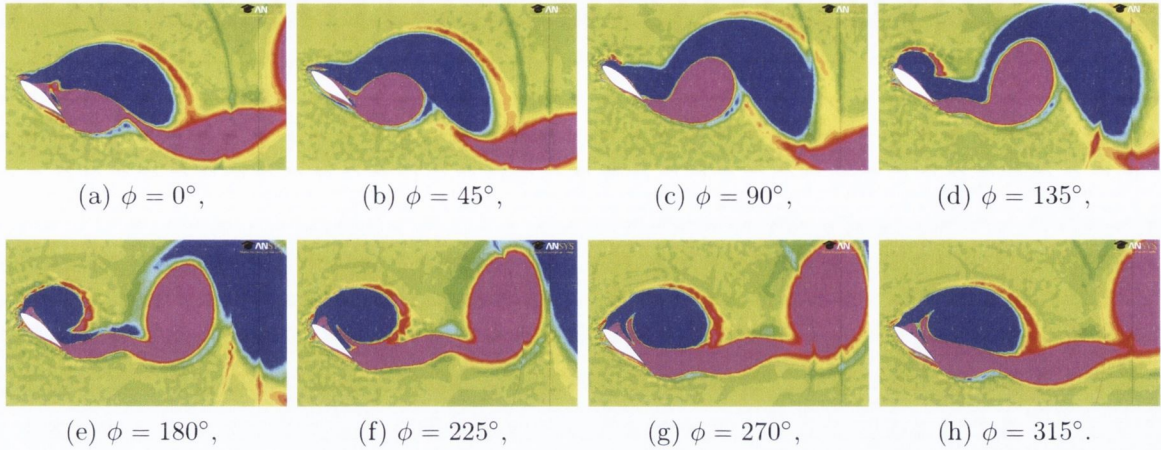


Figure 5.15: Close-up of the instantaneous vorticity field over a transverse oscillation cycle at $\alpha_{mean} = 40^\circ$, $r = 0.7$; lock-in condition. ■, counter-clockwise (positive) vorticity; ■, clockwise (negative) vorticity.

The lock-in behaviour of vortex-shedding in the presence of transverse motion at $A_t = 0.25c$ can be summarised over the entire angle of attack and frequency ranges around $r = 1$, shown in Fig. 5.16. The lock-in condition is not present for the entire angle of attack range. The lock-in range is more significant when the airfoil presents a smaller characteristic length (i.e. in the regions around $\alpha_{mean} = 40^\circ$ and $\alpha_{mean} = 140^\circ$), in the pre-coincidence area ($r < 1$). Conversely, in the post-coincidence area ($r > 1$), the risk of synchronisation is more significant in the region around $\alpha_{mean} = 90^\circ$, when the characteristic length is larger. It can be seen that $\alpha_{mean} = 50^\circ$ and $\alpha_{mean} = 130^\circ$ represent a sort of breaking-down behaviour for this type of motion too (as seen already in Sections 5.1 and 5.2). Perhaps the most curious behaviour observed for the transverse motion is this “transitional” one (symbolised \otimes in Fig. 5.16). The name “transitional behaviour” given in this work simply comes from an observation of the synchronisation map (Fig. 5.16). It is not a reference to the state of the boundary layer. It can be seen that this condition is present for incidences with smaller characteristic length ($\alpha_{mean} = 35^\circ$, $\alpha_{mean} = 40^\circ$, $\alpha_{mean} = 140^\circ$, $\alpha_{mean} = 145^\circ$), as a transition between lock-in and pseudo-lock-in, or between pseudo-lock-in and lock-out conditions. This behaviour may be interpreted as a struggle of the vortex shedding frequency to synchronise, eventually succeeding or not, as the frequency ratio varies. It may not be a coincidence that this behaviour happens only for angles of attack close to the limit at which periodic vortex shedding has been

observed (see Chapter 4; no periodic vortex shedding has been observed for $\alpha_{mean} < 35^\circ$ and $\alpha_{mean} > 145^\circ$). Hence, at these incidences for some conditions, the interaction between the fluid and the moving body may be strong enough to suppress the periodic vortex shedding temporarily. It would be interesting to prove if this behaviour remains consistent in a 3-D configuration.

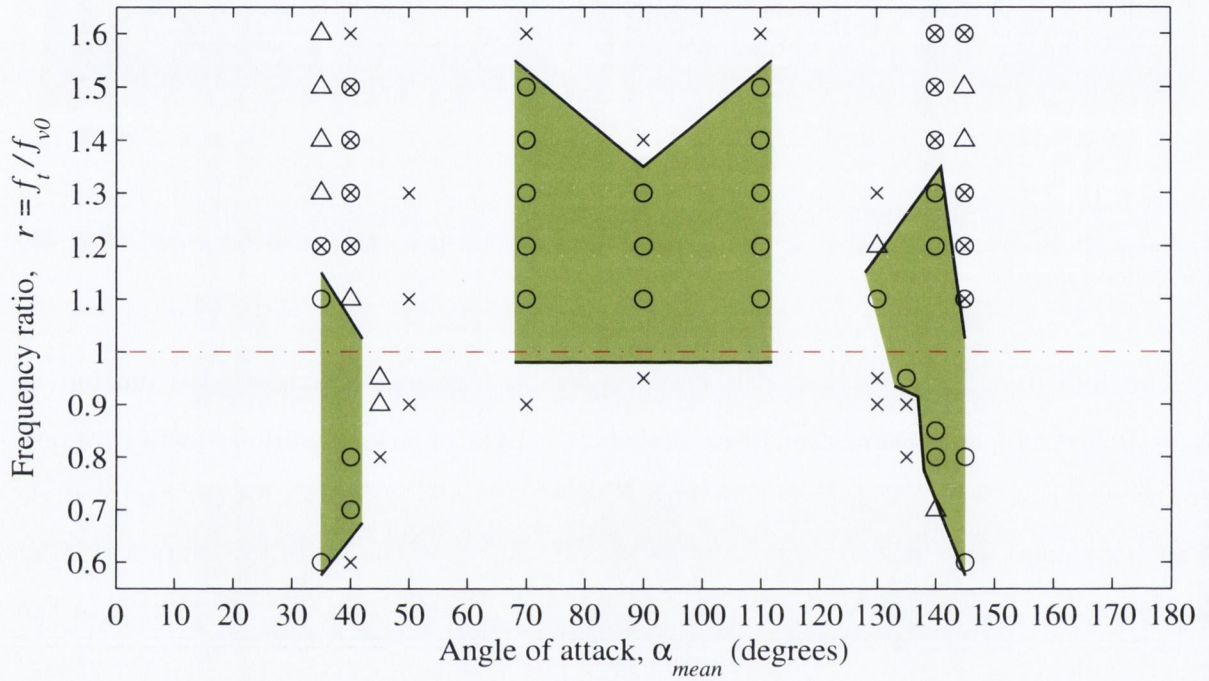


Figure 5.16: Synchronisation map for positive angles of attack, transverse motion at $A_t = 0.25c$: \circ , lock-in; \triangle , pseudo-lock-in (periodicity with sub-harmonics); \times , lock-out; \otimes , “transitional behaviour”.

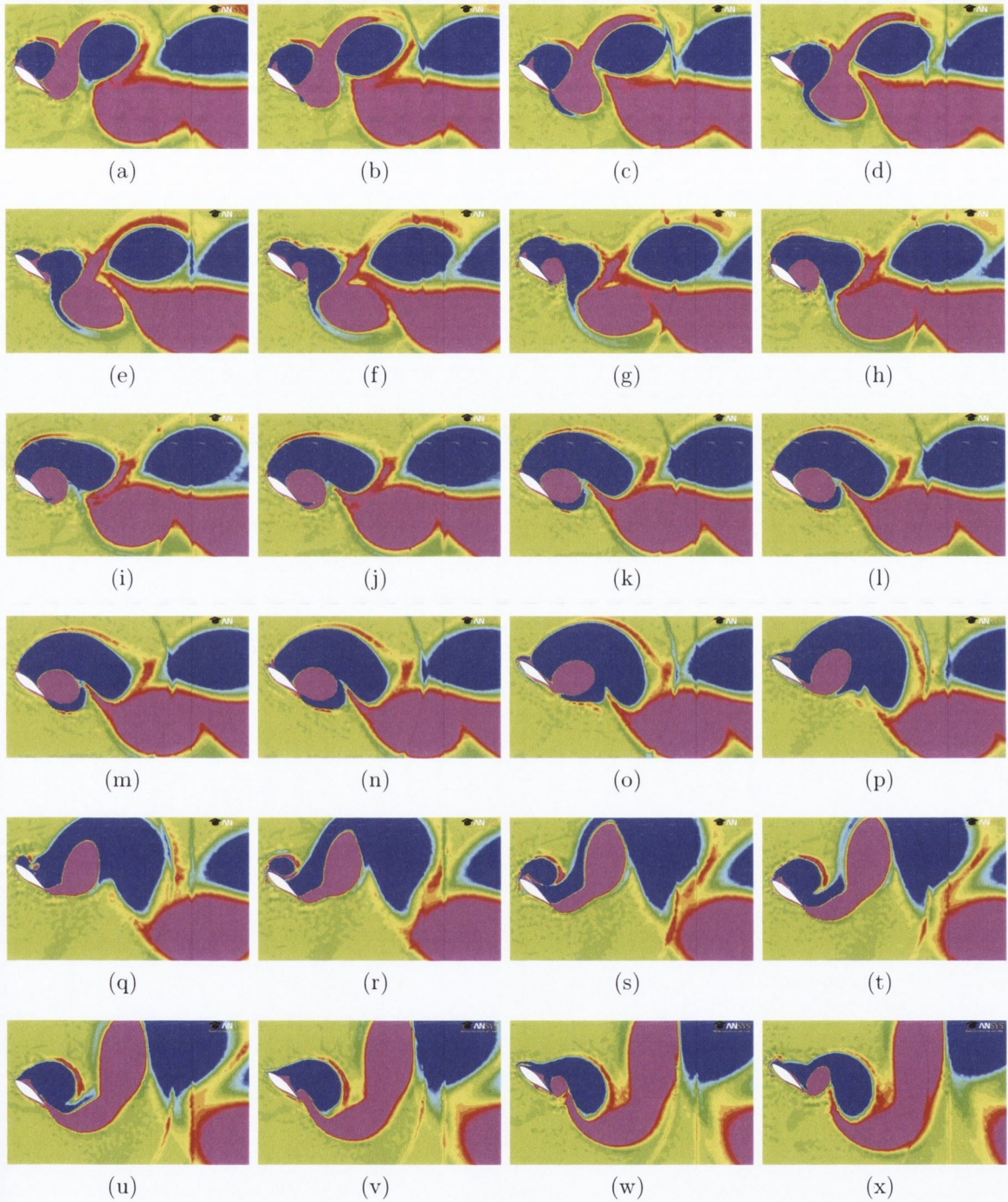


Figure 5.17: Close-up of the instantaneous vorticity field over a portion of time history ($\tau = [234 \rightarrow 243]$) for transverse motion, $\alpha_{mean} = 40^\circ$, $r = 1.2$; “transitional behaviour” condition. ■, counter-clockwise (positive) vorticity; ■, clockwise (negative) vorticity.

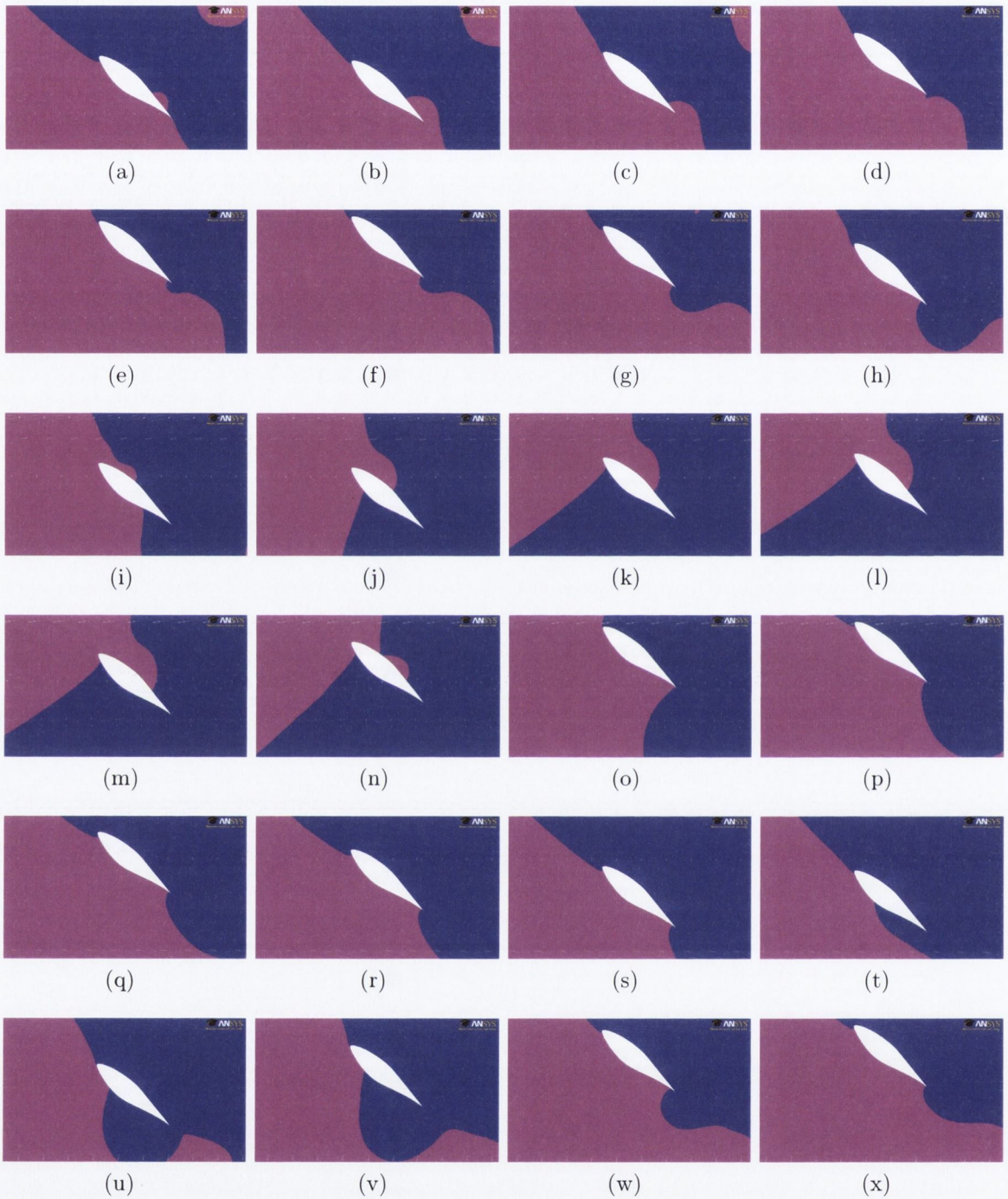
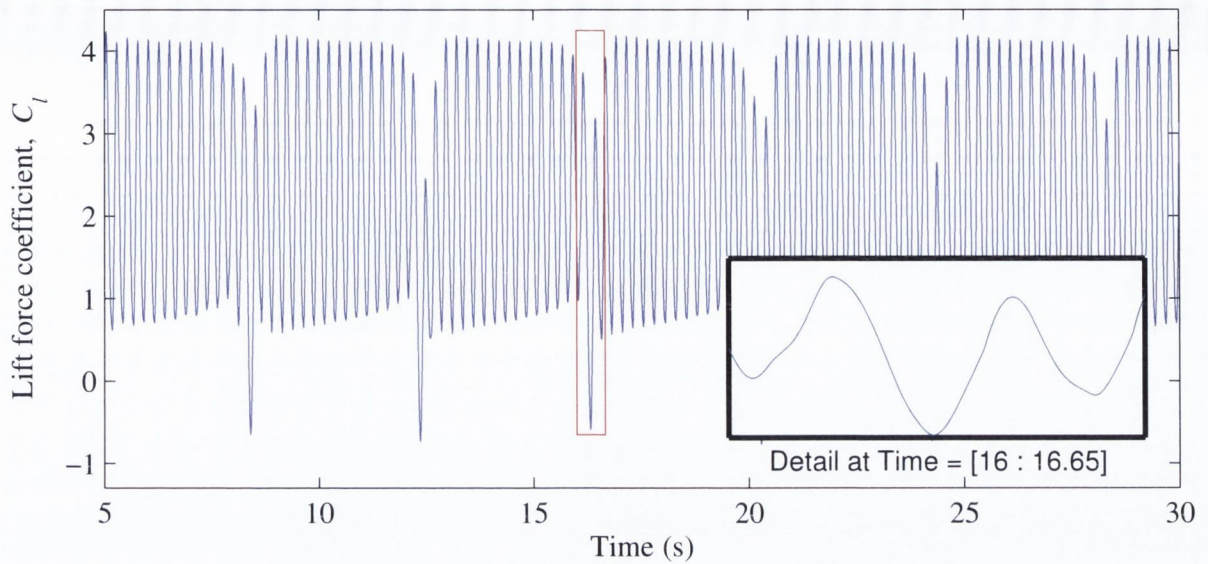
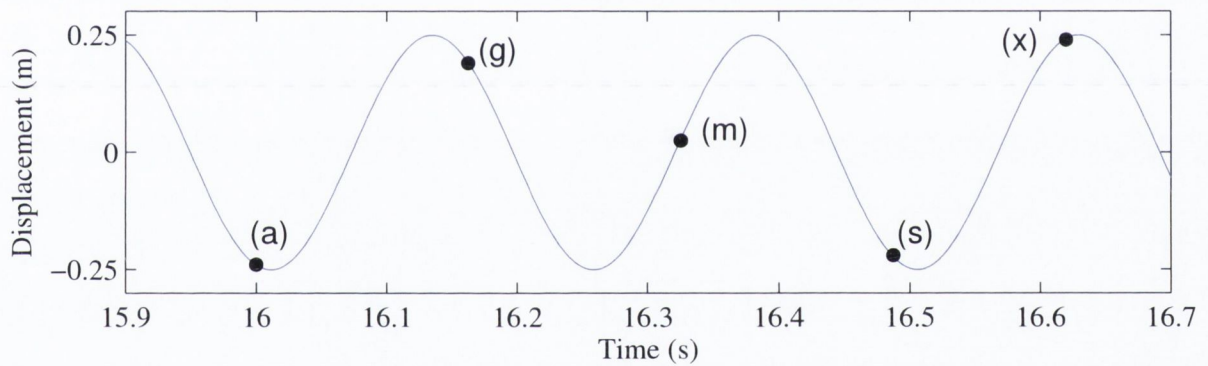


Figure 5.18: Close-up of the instantaneous pressure field over a portion of time history ($\tau = [234 \rightarrow 243]$) for transverse motion, $\alpha_{mean} = 40^\circ$, $r = 1.2$; “transitional behaviour” condition. ■, higher pressure; ■, lower pressure.



(a) Lift force coefficient time trace,



(b) Displacement time trace.

Figure 5.19: Portion of the time history used in Figs. 5.17 and 5.18: (a), lift force coefficient time trace with a zoom-in of the history portion; (b) displacement for zoom window, points labelled with letters correspond to the airfoil positions in Figs. 5.17 and 5.18.

Figures 5.17 and 5.18 may help to interpret the observed “transitional behaviour”, showing respectively the instantaneous vorticity and pressure fields in the vicinity of the airfoil, over a portion of the time history ($\tau = [234 \rightarrow 243]$). Figure 5.19 shows details of the airfoil motion over the considered time history: lift force coefficient in Fig. 5.19(a) and displacement in Fig. 5.19(b), with labelled positions corresponding to letters in Figs. 5.17 and 5.18. At some point, the clockwise (negative) vorticity starts growing in an unusual fashion ending up to inglobate the counter-clockwise vorticity, Figs. 5.17(i) \rightarrow (p). This odd behaviour can be found also looking at the pressure field around the airfoil, which normally presents a higher pressure on the lower side. It can be

seen that part of those instantaneous vorticity stages correspond to instantaneous lower pressure conditions on the lower side of the airfoil (Figs. 5.18(k) \rightarrow (n) in particular). Eventually the usual pressure field is restored with a higher pressure on the lower side of the airfoil (Fig. 5.18(o)). Correspondingly, it can be seen in Fig. 5.17(o) that the counter-clockwise (positive) vorticity starts to grow again, pushing the clockwise vortex further which eventually detaches (Fig. 5.17(t)).

5.3.2 Transverse amplitude effect

The effect of the transverse oscillation amplitude on the lock-in around $r = 1$ has been assessed for angles $\alpha_{mean} = 40^\circ$ and $\alpha_{mean} = 140^\circ$, for which the synchronisation boundaries are proposed respectively in Figs. 5.20(a) and 5.20(b). For $\alpha_{mean} = 140^\circ$ it has been easier to define a sort of boundary (Fig. 5.20(b)), while for $\alpha_{mean} = 40^\circ$ the lock-in post-coincidence region is uncertain to assess (Fig. 5.20(a)); hence the choice to leave it without boundary. It is interesting to note that, for both the incidences analysed, the “transitional behaviour” is present only for $A_t = 0.25c$. As the amplitude increase, that condition evolves to a lock-out or to a pseudo-lock-in. This may suggest that the motion amplitude chosen for the parametric study is a particular value that, acting with certain incidences and motion frequencies, leads to this peculiar non-linear behaviour. As a general comment, these results are typical of VIV, i.e. the susceptibility to synchronising increases with increasing oscillation amplitude.

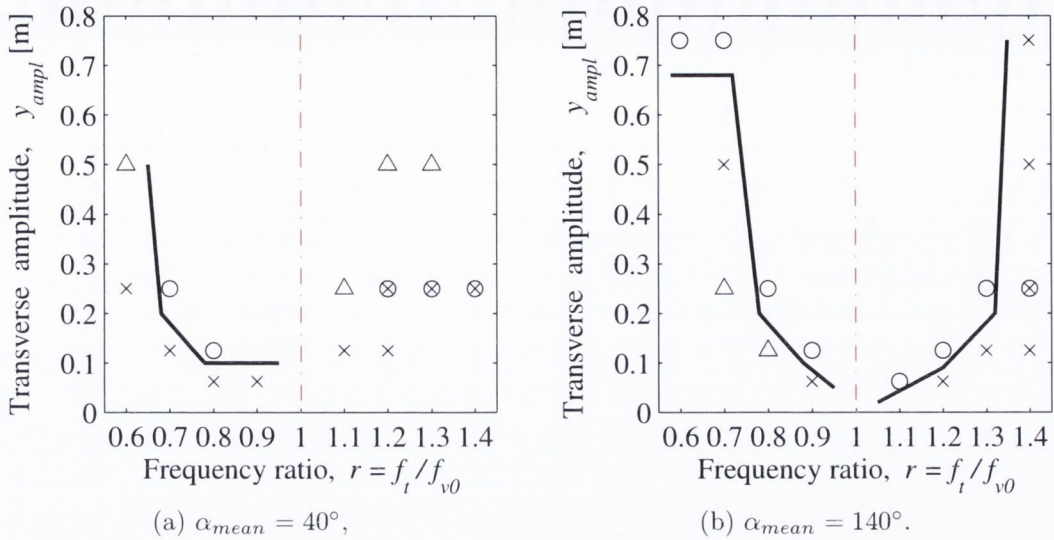


Figure 5.20: Proposed synchronisation boundaries for transverse motion amplitude at two incidences: \circ , lock-in; \triangle , pseudo-lock-in (periodicity with sub-harmonics); \times , lock-out; \otimes , “transitional behaviour”.

5.4 Summary

It has been found that a NREL S809 wind turbine blade section subjected to a 1-degree of freedom motion (periodic pitching, stream-wise and transverse oscillation) at high mean angles of attack may exhibit vortex shedding synchronisation when the motion frequency does not coincide with the nominal vortex shedding frequency.

- **PITCHING MOTION.** It has been found that the wake is more susceptible to lock-in when the airfoil is at incidences presenting shallower characteristic length ($\alpha_{mean} \approx 40^\circ, 140^\circ$). This is true whether the sharp trailing edge is upstream or downstream of the blunt leading edge.

The effect of the oscillation amplitude has also been investigated. The behaviour observed was expected, i.e. the extent of the lock-in frequency range decreases as the motion amplitude is reduced. Moreover, it has been observed that a sharp trailing edge in upstream position seems to slightly reduce the risk of lock-in.

- **STREAM-WISE MOTION.** It has been found that the wake is more susceptible to lock-in to the first harmonic of motion frequency when the blade profile is at shallower angles ($\alpha_{mean} \approx 40^\circ, 140^\circ$), for a frequency ratio in a range of $0.5 < r < 1$.

This is true whether the sharp trailing edge is upstream or downstream of the round leading edge. Synchronisation to the second harmonic of the motion frequency seems to occur only when the sharp trailing edge is in upstream position. This is observed in the vicinity of $r = 0.5$ only. The region around $r = 2$ seems to be more prone to lock-in, as it would be expected for the stream-wise motion, for incidences presenting larger characteristic length (around the vertical position to the flow). The behaviour observed in this region is not a pure synchronisation, as sub-harmonics are present. Nonetheless, the lift coefficient time trace presents periodicity, and its spectrum does not show the nominal vortex shedding frequency as it appears to be coalesced with the stream-wise motion frequency. Hence, this behaviour has been labelled as “pseudo-lock-in”.

The effect of the oscillation amplitude has also been investigated. The behaviour observed is not completely expected as in some cases (depending on the motion frequency and the freestream velocity), an increase in motion amplitude leads to the suppression of lock-in. It is suggested that this is due to a significant path travelled by the airfoil in the same freestream sense preventing the leading edge vortex to really separate.

- **TRANSVERSE MOTION.** It has been observed a different synchronisation behaviour depending on the pre- or post-coincidence region. For $r < 1$, the lock-in range is more significant when the airfoil presents a smaller characteristic length, as observed for the pitching motion. For $r > 1$, the risk of synchronisation is more significant in the region around the vertical position to the flow, when the characteristic length is larger.

For the particular fixed motion amplitude investigated, $A_t = 0.25c$, a peculiar behaviour has been observed, in configuration at incidences with smaller characteristic length, for some frequency ratios. It has been named “transitional behaviour”, as it plays a sort of transition between lock-in and pseudo-lock-in, or between pseudo-lock-in and lock-out conditions. The lift coefficient time trace is not periodic, and the wake presents, periodically, a missing vortex shed (positive or negative depending on the incidence, respectively if $\alpha_{mean} < 90^\circ$ or $\alpha_{mean} > 90^\circ$).

The effect of the oscillation amplitude has also been investigated. As seen for the pitching motion, the susceptibility to synchronising increases augmenting the oscillation amplitude, as expected. The “transitional behaviour” is not observed for amplitudes different from $A_t = 0.25 c$.

Note that the lock-in map boundaries presented in this work ($\alpha_{mean} = 35^\circ, 145^\circ$) are directly related to the results for this particular CFD model set-up and are not to be considered as absolute lock-in references. Further verifications could show how much these boundaries depend on the model settings.

In the next Chapter, a lumped parameter model for VIV of airfoils, based on the wake oscillator model, is proposed for the pitching and transverse motions.

Chapter 6

Lumped parameter model

In this Chapter, a lumped parameter model is proposed for a single degree of freedom VIV of airfoils in pitching and transverse oscillation.

An extensive review on the mathematical models used to investigate VIV of cylinders has been presented by Gabbai & Benaroya [105]. The idea of using a van der Pol type oscillator to represent the oscillating force on a cylinder due to vortex shedding is credited to Bishop & Hassan [106]. A representation of fluctuating lift behaviour in terms of a proposed wake-oscillator is presented by Hartlen & Currie [107], demonstrating the potential of the wake-oscillator concept for future VIV studies. This wake oscillator is self-excited and it is subject to a coupling term proportional to the transverse cylinder velocity. They succeeded in qualitatively capturing experimental behaviour, for example a large cylinder oscillation amplitude resonance region when the vortex shedding frequency is near the natural frequency of the cylinder. Facchinetti *et al.* [108] examined three different types of coupling (displacement, velocity, acceleration), i.e. the action of the structure on the fluid wake oscillator. It was found that the acceleration coupling best succeeded in qualitatively modelling the VIV features considered, although no substantial physical explanation for this was advanced. The VIV wake oscillator model proposed in this Chapter for oscillating airfoils is based on the model by Facchinetti *et al.* [108].

The goal of this approach is to qualitatively reproduce the lock-in behaviour observed with URANS simulations (see Sections 5.1 and 5.3), but with much less computational effort. This would allow vortex shedding to be incorporated into a structural response model. The pitching and transverse motions are investigated respectively in Sections 6.2 and 6.3.

6.1 Implementation

6.1.1 Set-up

The model presented here is based on the wake oscillator proposed by Facchinetti *et al.* [108], which in turn is based on the classical van der Pol oscillator. The wake is modelled as a non-linear oscillator:

$$\ddot{q} + \varepsilon \Omega_f (q^2 - 1) \dot{q} + \Omega_f^2 q = F \quad (6.1)$$

where q is the dimensionless wake variable (overdots mean derivative with respect to the dimensionless time), ε is effectively a damping parameter, Ω_f is the vortex shedding angular frequency, F models the effect of the structure motion on the near wake by providing coupling with structural dynamics. The wake variable, q , is here associated with the fluctuating lift coefficient. The coupling term is based on the acceleration of the structure as recommended by Facchinetti *et al.* [108]:

$$F = (A/D) \ddot{s} \quad (6.2)$$

where \ddot{s} is a generic (i.e. not specific to a particular degree of freedom) acceleration of the structure, A is the coupling parameter, D is the characteristic length (e.g. cylinder diameter). Note that Facchinetti *et al.* [108] presented a coupled 2-DOF system as the structure was free to vibrate. In this work, only the wake oscillator is considered, since the acceleration is imposed (the structure motion is prescribed as per Eqs. 5.4 and 5.8). Note that the 2-DOF system used by Facchinetti *et al.* is composed of the 1-DOF structural motion and the 1-DOF wake model (i.e. it is not a 2-DOF motion of the cylinder). In the present work, only one equation accounting for the 1-DOF of the wake model is used; the equation for the structural motion is not needed as the vibration is prescribed (as done in Chapter 5 for the CFD study).

6.1.2 Verification

Figure 6.1 shows the lock-in region for a cylinder compared with the parameters specified by Facchinetti *et al.* [108]. The lock-in behaviour obtained from the current model implementation compares well with the lock-in boundaries presented by Facchinetti *et al.* [108], offering confidence in the current implementation.

As the wake oscillator model is a semi-empirical model, some of its parameters require empirical data to be quantified. In the current study, due to the apparent lack of experimental data on VIV of oscillating airfoils at high angle of attack and high Reynolds number, the “empirical” data used are the lock-in boundaries obtained from CFD simulations presented in Sections 5.1 and 5.3. The parameters to be defined are ε and A . A harmonic balance method was used initially for two sample cases ($\alpha = 40^\circ$ and $\alpha = 140^\circ$), using the harmonics coefficients obtained from the study of vortex shedding of the static NREL S809 (see Chapter 4). However, the prediction of lock-in boundaries did not compare well with the dynamic CFD results. This suggests that maybe it is not possible to obtain an universal set of parameters for a VIV model of airfoil at different angles of attack.

Another approach has been used: estimating A for each angle of attack, keeping ε constant. The rationale for this approach is that the sensitivity of the model predictions to these parameters suggests A is more significant. A sensitivity analysis of ε and A has been conducted using the model proposed by Facchinetti *et al.* [108] for a cylinder ($m^* = 4$). It can be clearly seen in Fig. 6.2(a) that the reduced velocity range for lock-in is not affected by changing the ε value (at least for the considered variation of $\pm 100\%$). In contrast, Fig. 6.2(b) shows that a variation of A significantly affects the system behaviour.

For every angle of attack two estimates of A are obtained: one for the post-coincidence boundary, the other for the pre-coincidence boundary (from Figs. 5.3 and 5.16). The proposed values of A is the mean of these estimates. The ε value used is 0.45 based on the mean of ε obtained with the initial harmonic balance approach for the sample cases of $\alpha = 40^\circ$ and $\alpha = 140^\circ$. For comparison, the ε value used by Facchinetti *et al.* [108] for a cylinder is 0.3.

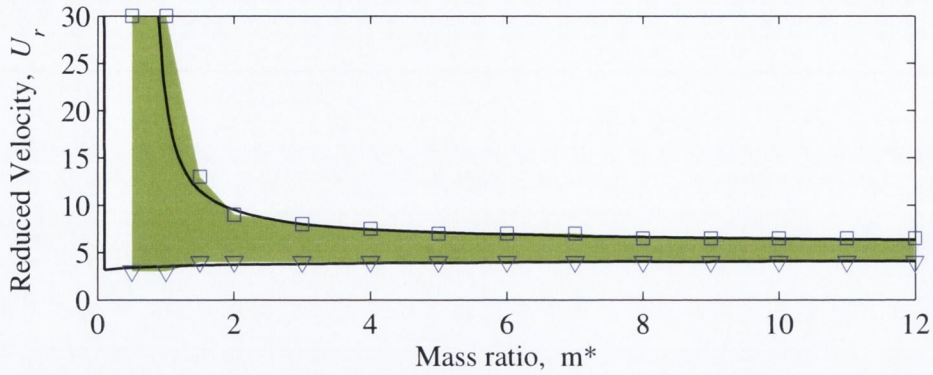
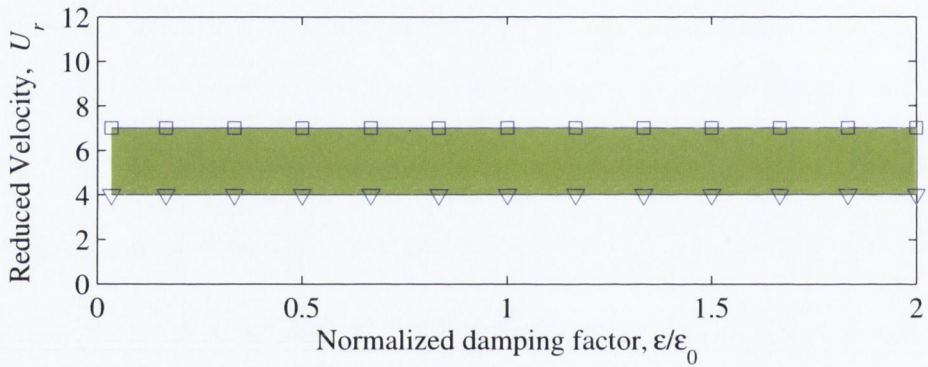
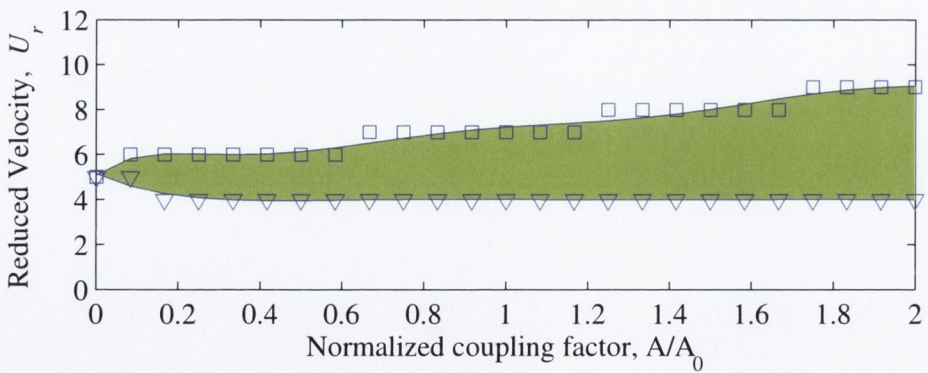


Figure 6.1: Comparison of predicted lock-in boundaries for a circular cylinder: □, upper boundary (current implementation); ▽, lower boundary (current implementation); ■, synchronization region (current implementation); —, [108].



(a) Sensitivity analysis of the damping parameter, ε , with reduced velocity, U_r , for $m^* = 4$,



(b) Sensitivity analysis of the coupling parameter, A , with reduced velocity, U_r , for $m^* = 4$.

Figure 6.2: Sensitivity of the VIV model of a circular cylinder by Facchinetti *et al.* [108] to parameter values. Lock-in region: □, upper boundary; ▽, lower boundary; ■, synchronization region.

6.2 Pitching motion VIV model

The dynamic behaviour of the wake system for pitching motion has been investigated for the whole range of angles of attack considered for the CFD analysis in Section 5.1. The aim is to match the synchronization results obtained from the CFD model, in order to propose a set of parameters (i.e. ε, A) to be used for a preliminary VIV risk assessment at each angle of attack.

For the airfoil in pitching motion, the wake oscillator equation has been reformulated as:

$$\ddot{q} + \varepsilon(2\pi f_{v0})(q^2 - 1)\dot{q} + (2\pi f_{v0})^2 q = (A/L)\ddot{\alpha} \quad (6.3)$$

where q, ε, A are defined in the same way as in Eq. 6.1; $f_{v0} = S_t U_\infty / L$ is the static vortex shedding frequency, L is the characteristic length of the airfoil, $\ddot{\alpha}$ is the angular acceleration. Note that if the mean angle of attack varies, so does the characteristic length as it is defined to be the vertical projection of the chord with respect to the flow direction (see Chapter 4).

The pitching motion acceleration can be derived by Eq. 5.4, yielding:

$$\ddot{\alpha}(t) = -(2\pi f_p)^2 \alpha_{ampl} \sin(2\pi f_p t) \quad (6.4)$$

6.2.1 Results

Figure 6.3 shows the time record and its relative spectrum of the wake variable, q , for a sample lock-in case. The particular conditions for this case are $\alpha = 40^\circ$, $r = 0.7$. As seen in Chapter 5, for the lock-in condition the wake variable (or lift coefficient) presents a periodic time trace with a dominant frequency (Fig. 6.3(a)). Figure 6.3(b) shows the spectrum, with the presence of the dominant frequency and its odd harmonics only, as the model has a cubic behaviour (see Eq. 6.1). Remember that q is effectively a normalised lift coefficient. Thus, the absence of a peak in the spectrum around $r = 1$ (i.e. the static vortex shedding frequency at $f^* = 1$) indicates that the wake frequency has locked-in to the pitching motion frequency.

As discussed above, an estimate of A for each α_{mean} can be obtained. Figure 6.4 shows the variation of the coupling parameter, A , with angle of attack over the whole range considered, for a constant value of pitching amplitude, $\alpha_{ampl} = 7^\circ$. For comparison,

the value proposed by Facchinetti *et al.* [108] for a cylinder ($A = 12$) is indicated with a dash-dot line. It can be concluded that a generic value of $A \approx 1$ might be used in the range of ($45^\circ \leq \alpha \leq 140^\circ$), from a qualitative point of view. At incidences $\alpha = 35^\circ, 40^\circ, 145^\circ$ higher values are present, consistent with the larger frequency lock-in range observed in the CFD study.

Figure 6.5 shows the proposed lock-in boundaries obtained from the wake oscillator model, superimposed on the synchronization region obtained from the CFD model (see Fig. 5.3), referring to $\alpha_{ampl} = 7^\circ$. It can be seen that, qualitatively speaking, the VIV model reproduces the CFD results. This is perhaps not surprising, as the model has been tuned with CFD data for this pitching amplitude. Moreover, in the range of ($45^\circ \leq \alpha \leq 140^\circ$), a good match is achieved quantitatively. For incidences $\alpha = 35^\circ, 40^\circ, 145^\circ$ the wake oscillator model overestimates the lock-in frequency range, due to a higher value of A .

An analysis of the effect of the pitching amplitude has also been conducted, at the same incidences considered for the CFD model in Section 5.1, shown in Fig. 6.6 using the value of A from Fig. 6.4. The proposed lock-in boundaries are superimposed on the synchronization region obtained from the CFD model (shown in detail in Fig. 5.6). Results indicate that the wake oscillator model follows the expected behaviour (i.e. lock-in range decreasing with amplitude reduced). However, while there is reasonable qualitative agreement, a dedicated tuning of the A value would be needed for every amplitude to achieve a close quantitative match with the CFD results.

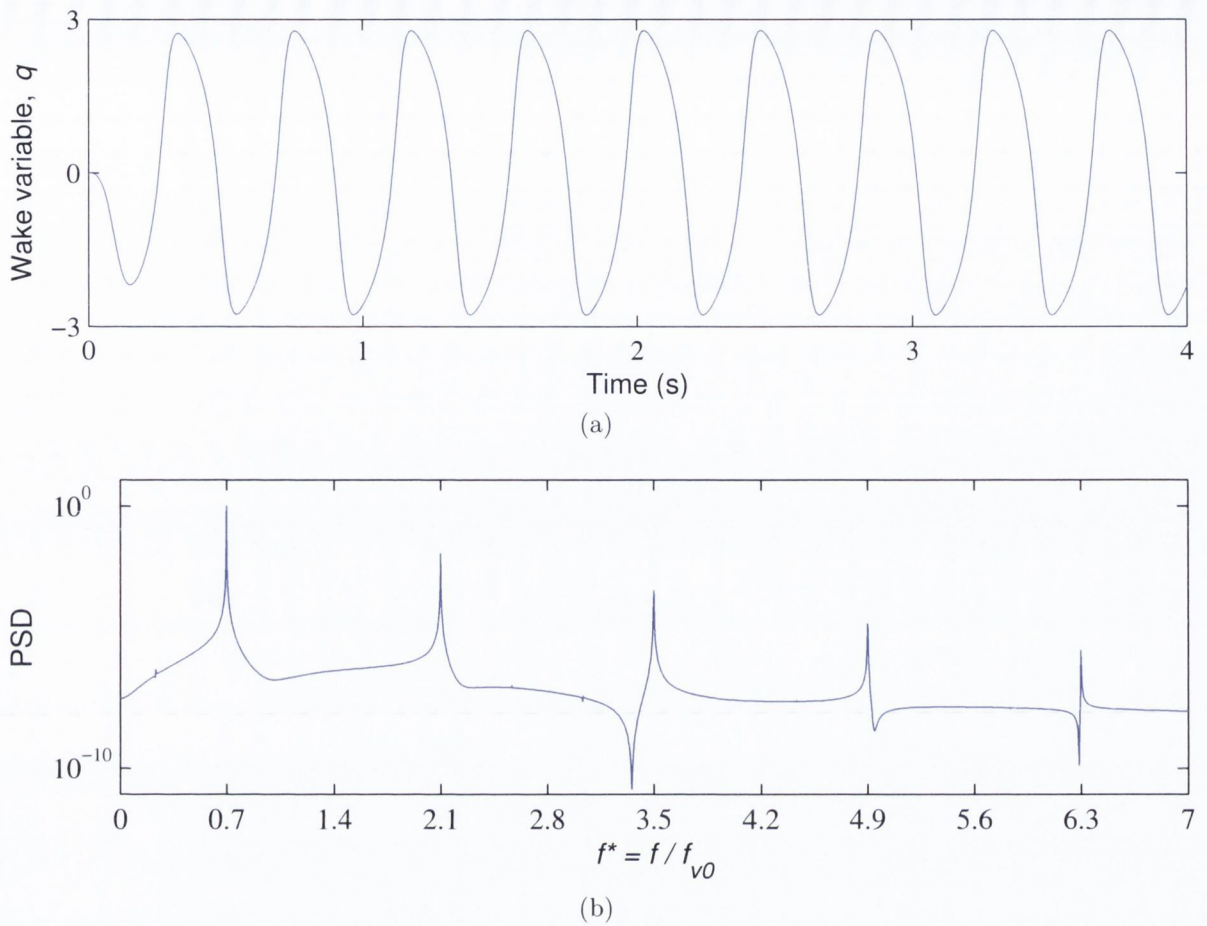


Figure 6.3: Detail of the time record (a) and spectrum (b) of the wake variable, q , for $\alpha = 40^\circ$ at $r = 0.7$; lock-in condition. Cubic behaviour with odd harmonics only.

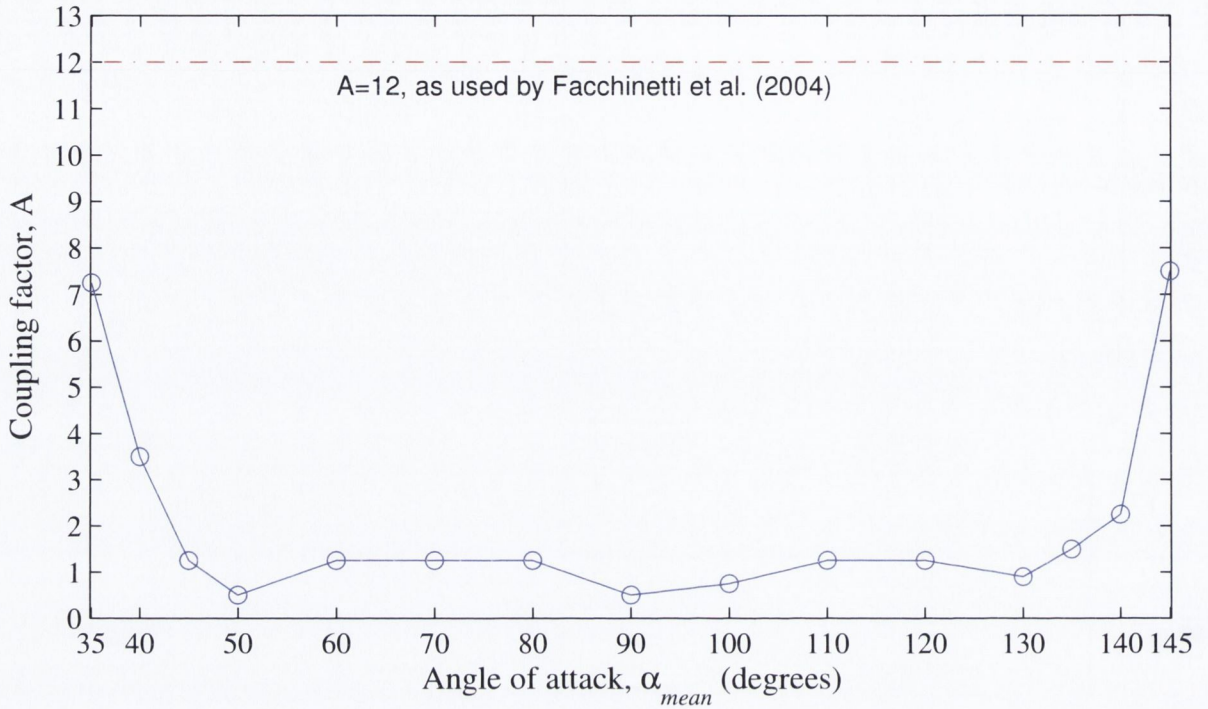


Figure 6.4: Variation of the coupling factor, A , with angle of attack, for pitching motion at $\alpha_{ampl} = 7^\circ$. Dash-dot line indicates the value used by [108] for a cylinder.

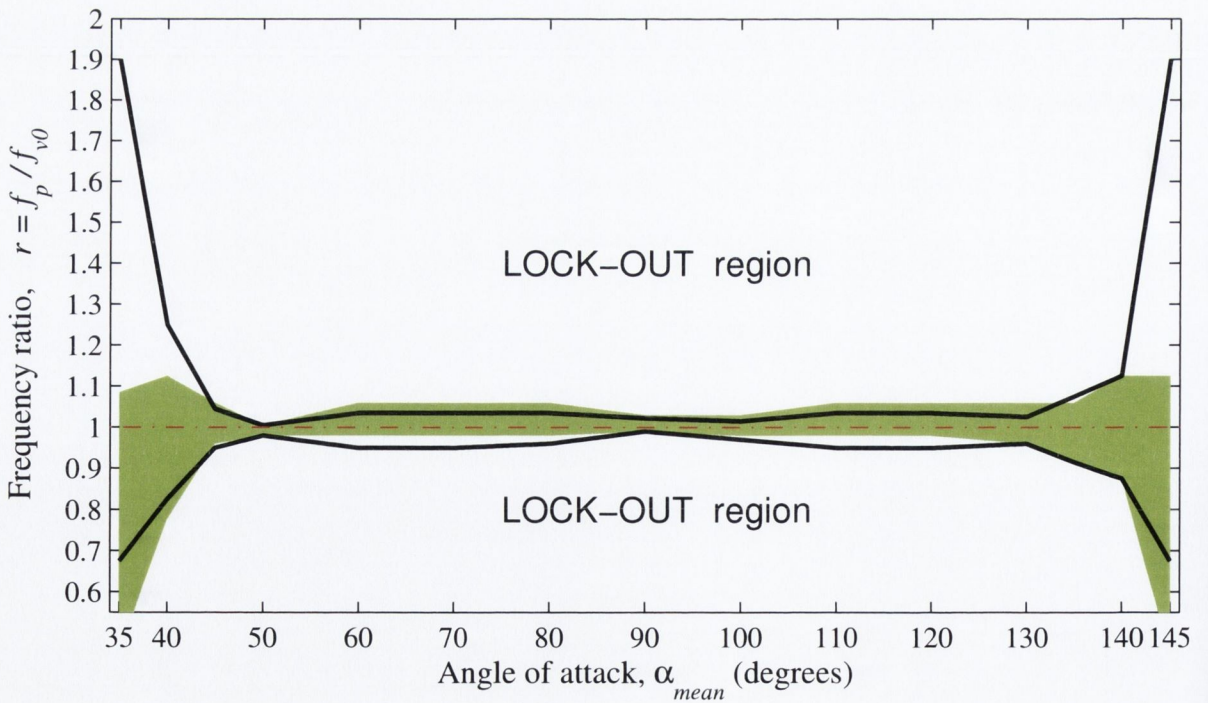


Figure 6.5: Proposed synchronization boundaries for pitching motion at $\alpha_{ampl} = 7^\circ$: —, VIV model; ■, CFD model.

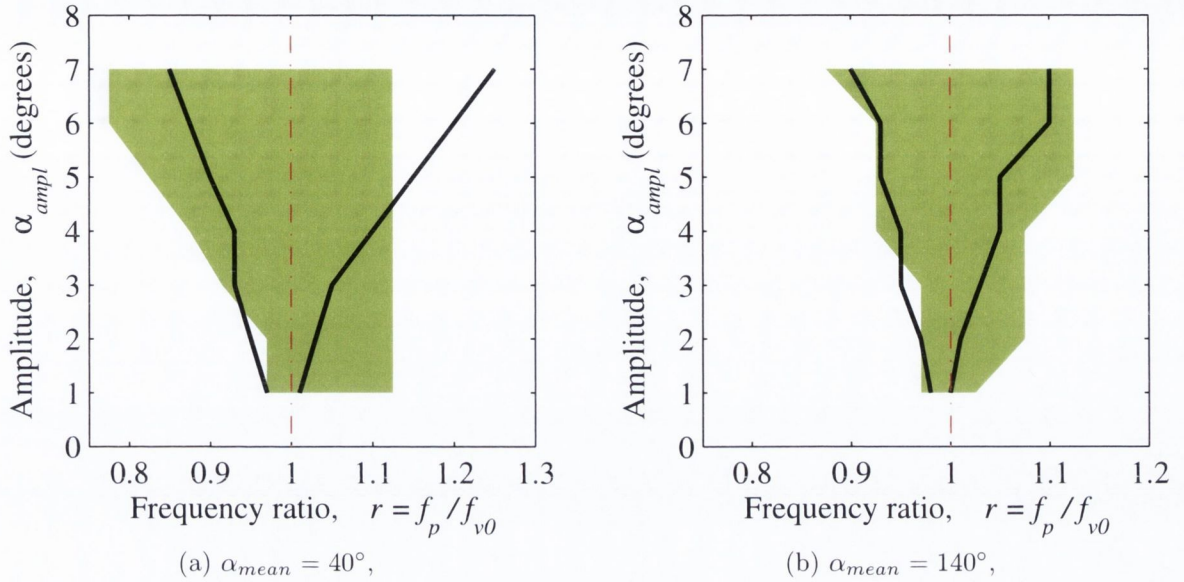


Figure 6.6: Proposed synchronization boundaries for pitching amplitude effect at two incidences: —, VIV model; ■, CFD model.

6.3 Transverse motion VIV model

The dynamic behaviour of the wake system for transverse motion has been investigated for the whole range of angles of attack considered for the CFD analysis in Section 5.3. The aim is to match the synchronization results obtained from the CFD model, in order to propose a set of parameters (i.e. ε , A) to be used for a preliminary VIV risk assessment at each angle of attack.

For the airfoil in transverse motion, the wake oscillator equation has been reformulated as:

$$\ddot{q} + \varepsilon(2\pi f_{v0})(q^2 - 1)\dot{q} + (2\pi f_{v0})^2 q = (A/L)\ddot{y} \quad (6.5)$$

where q , ε , A are defined in the same way as in Eq. (6.1); $f_{v0} = S_t U_\infty / L$ is the static vortex shedding frequency, L is the characteristic length of the airfoil, \ddot{y} is the acceleration.

The transverse motion acceleration can be derived by Eq. (5.8), yielding:

$$\ddot{y}(t) = -(2\pi f_t)^2 A_t \sin(2\pi f_t t) \quad (6.6)$$

6.3.1 Results

Figure 6.7 shows the variation of the coupling parameter with angle of attack over the whole range considered, for a constant value of transverse oscillation amplitude, $A_t = 0.25c$. For comparison, the value proposed by Facchinetti *et al.* [108] for a cylinder ($A = 12$) is indicated with a dash-dot line. It can be concluded that a generic value of $A \approx 2$ might be used in the range of ($40^\circ \leq \alpha \leq 140^\circ$), from a qualitative point of view. At incidences $\alpha = 35^\circ, 145^\circ$ higher values are present, consistent with the larger frequency lock-in range observed in the CFD study, albeit lower compared to the pitching motion behaviour (Fig. 6.4).

Figure 6.8 shows the proposed lock-in boundaries obtained from the wake oscillator model, superimposed on the synchronization region obtained from the CFD model (see Fig. 5.16), referring to $A_t = 0.25c$. It can be seen that, contrary to what was obtained for the pitching motion (Section 6.2), the model fails to reproduce the trend of the CFD results even qualitatively. An overestimation of the lock-in frequency range is present for incidences $\alpha = 35^\circ, 40^\circ, 140^\circ, 145^\circ$, where the value of A is higher. The failure of the qualitative prediction of the lock-in occurs in particular when the characteristic length is around its maximum ($70^\circ \leq \alpha \leq 110^\circ$); the model does not capture the biased behaviour in the post-coincidence regime.

An analysis of the effect of the transverse motion amplitude has also been conducted, at the same incidences considered for the CFD model in Section 5.3, shown in Fig. 6.9, using the value of A from Fig. 6.7. The proposed lock-in boundaries are superimposed on the synchronization region obtained from the CFD model (shown in detail in Fig. 5.20). Results indicate that the wake oscillator model follows the expected behaviour (i.e. lock-in range decreasing with amplitude reduced). As seen for the pitching motion in Section 6.2, a dedicated tuning of the A value would be needed for every amplitude to achieve a close quantitative match with the CFD results.

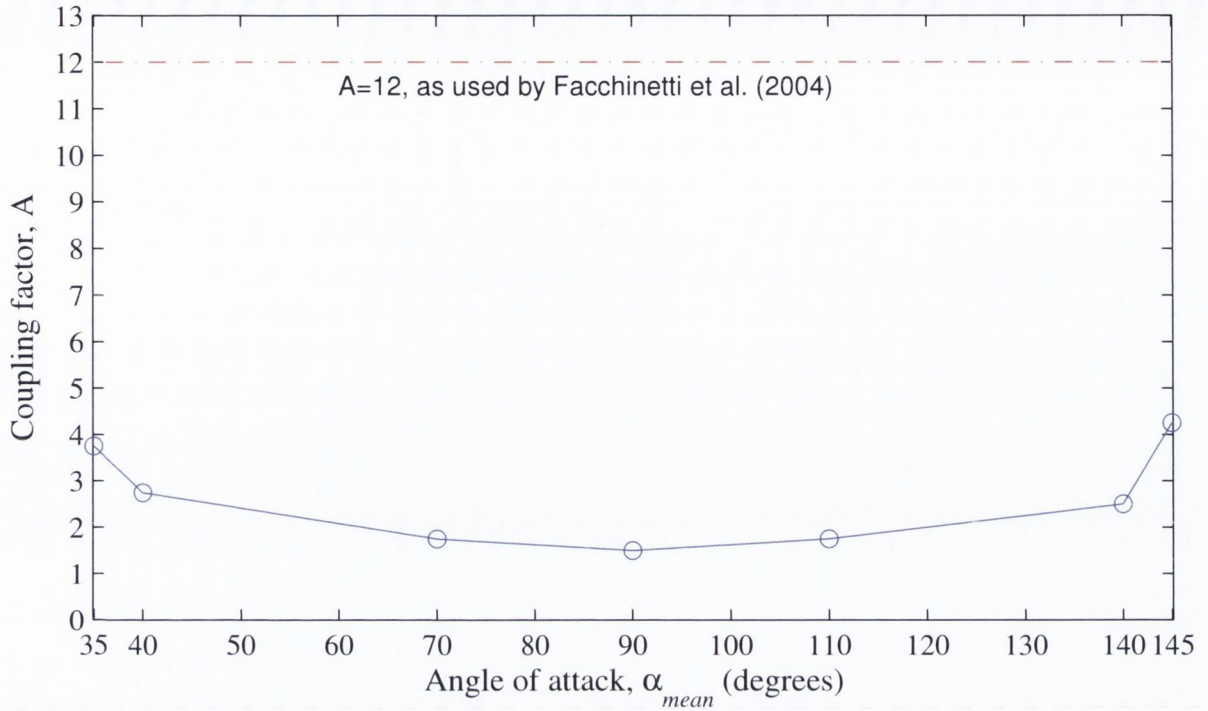


Figure 6.7: Variation of the coupling factor, A , with angle of attack, for transverse motion at $A_t = 0.25c$. Dash-dot line indicates the value used by [108] for a cylinder.

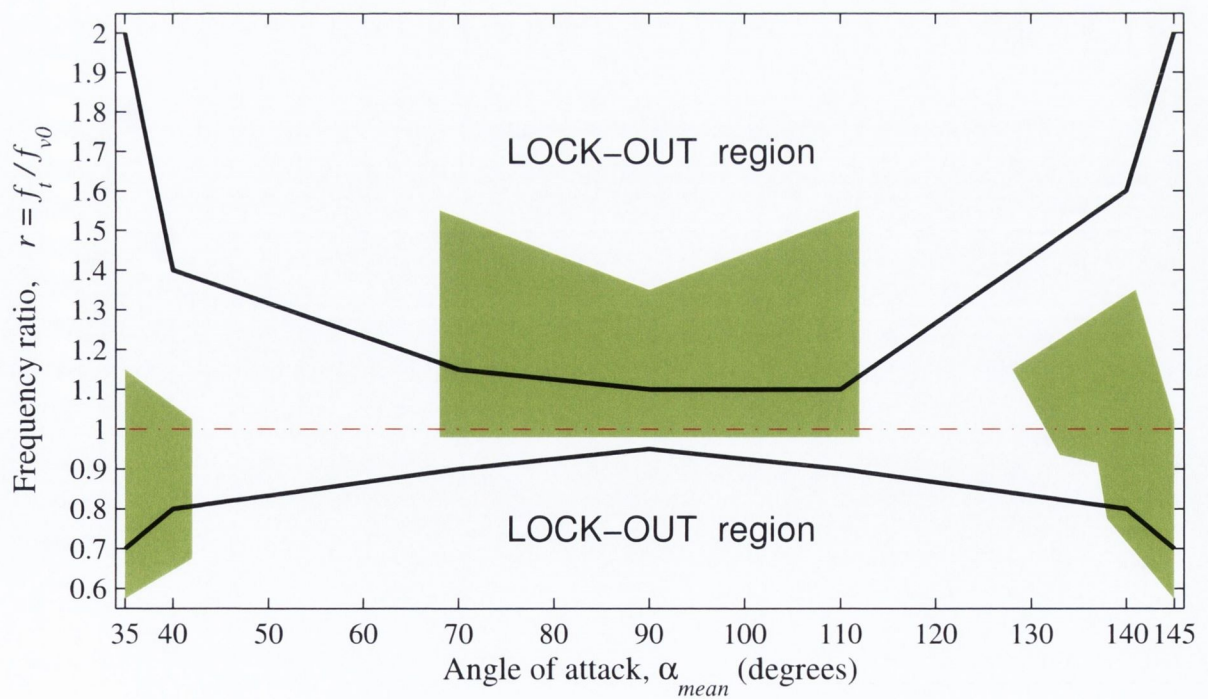


Figure 6.8: Proposed synchronization boundaries for transverse motion at $A_t = 0.25c$: —, VIV model; ■, CFD model.

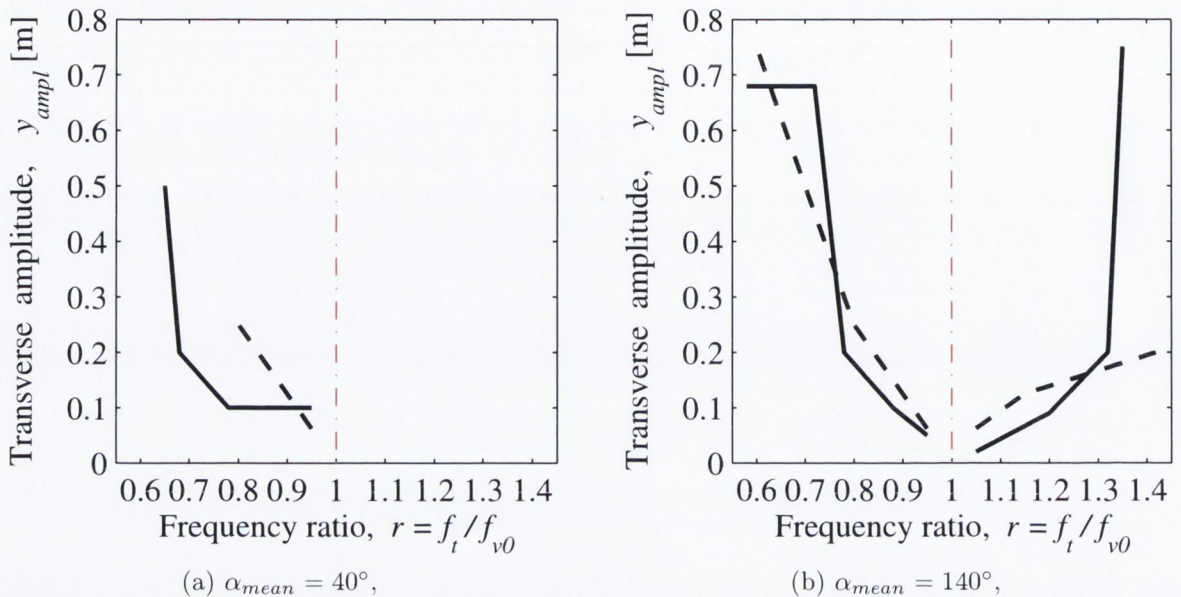


Figure 6.9: Proposed synchronization boundaries for transverse amplitude effect at two incidences: $- -$, VIV model; $-$, CFD model.

6.4 Summary

A lumped parameter VIV model (wake oscillator model) has been proposed for oscillating airfoils in 1-degree of freedom pitching and transverse motion. The lock-in boundaries qualitatively match the overall results obtained with the CFD model. To obtain a quantitative prediction too, it is necessary to tune the coupling factor for each angle of attack and perhaps, each amplitude.

The model shows some success in predicting the lock-in behaviour for the pitching motion, qualitatively. The quantitative failure is more significant for smaller characteristic lengths. Generally, it seems that a universal coupling parameter cannot be used, as it is strictly dependent on the geometric configuration.

Moreover, the model does not seem to be applicable for the transverse motion, as the model fails in the prediction of lock-in even from a qualitative perspective. This is in contrast with findings for a cylinder (in transverse oscillation) [108]. It is apparent that the importance of the geometry, which is not taken into account by the model itself, plays a fundamental role in the case of an airfoil compared to a cylinder. This is not surprising: for an airfoil the flow separation points are not at the same stream-wise position (except

for a very small range of characteristic length, i.e. around the vertical position with respect to the flow) as it happens for a cylinder. This means that an interaction occurs between the vortex (shed at the upwind edge) and the near surface region while it travels away.

It can be concluded that the adoption (and its manipulation) of the wake oscillator model (as proposed for a cylinder by Facchinetti *et al.* [108]) to be adapted and used for an airfoil does not represent a sensible mean to assess the risk of VIV. Some qualitative agreement with the CFD results appear encouraging, but it is clear that, even for 1-DOF motion, more complex modelling is needed. However, these initial results for the lumped parameter wake model are not encouraging for applications to a 2-DOF structural motion.

In the next Chapter, CFD simulations for two combinations of the three types of single degree of freedom motion will be presented: coupled stream-wise/transverse and stream-wise/pitching motions.

Chapter 7

Case 3: 2-DOF moving airfoil

Previously (Chapter 5), the behaviour of the NREL S809 has been investigated for the three single degrees of freedom in isolation. In this Chapter two coupled types of motion are considered. The analysis of the single DOF motion suggests that it is sensible to investigate the effect of the stream-wise motion on the transverse and the pitching lock-in. Note that this kind of investigation on a cylinder has been executed experimentally by Jauvtis & Williamson [71] (see Chapter 2). The stream-wise motion seems to present the most different behaviour compared to the others, especially in the post-coincidence regime, where no synchronisation has been observed (see Chapter 5). Hence, the objective is to investigate two configurations where synchronisation is present for the transverse and the pitching motion, while it does not occur for the stream-wise one. These two sample cases are the incidences $\alpha_{mean} = 40^\circ$ and $\alpha_{mean} = 140^\circ$, both at the frequency ratio $r = 1.1$ (see the synchronisation maps in Figs. 5.3, 5.10, 5.16). This means that the frequency of oscillation is the same for both of the coupled motions. The parametric study is now based on an “amplitude ratio” (of the oscillation amplitudes of the two coupled motions), rather than a “frequency ratio” (as done in Chapter 5), and on the phase angle between the two motions. The couplings are then stream-wise/transverse and stream-wise/pitching and the study is effectively a motion amplitude analysis. For both of the couplings two phase angles are considered, $\phi = 0^\circ$ and $\phi = 90^\circ$. For the sake of clarity, Tabs.7.1 and 7.3 summarise all the combinations considered for the parametric study.

Three interconnected questions can be posed:

- what is the amount of transverse or pitching motion amplitude needed to cause

vortex shedding synchronisation where it is not occurring with a pure stream-wise motion?

- to what amplitude extent is the stream-wise motion preventing the transverse or the pitching motion to cause vortex shedding synchronisation?
- what is the stream-wise amplitude needed to suppress lock-in occurring for a pure transverse or pitching motion?

The aim is to investigate how much one or the other motion of the coupling affects the most the global vortex shedding behaviour of the system. For this reason the discussion is now focused on the motion amplitude rather than the frequency.

7.1 Coupled stream-wise/transverse motion

A series of two-dimensional unsteady simulations of the flow around the NREL S809 airfoil moving in a coupled stream-wise/transverse direction (translations x, y) have been performed, for $\alpha_{mean} = 40^\circ$ and $\alpha_{mean} = 140^\circ$, in order to investigate the effect the stream-wise motion has on the transverse lock-in behaviour. The sample case used is the frequency ratio $r = 1.1$ for both of the two angles of attack, i.e. using a unique motion frequency value, $f_s = f_t$, at which synchronisation does not occur for the stream-wise motion while it does for the transverse one.

The deforming mesh approach used is the same as per Section 5.2 and 5.3, i.e. for translational motions (Fig. 5.7). The motion function in the UDF includes both laws of motion presented in Eqs. 5.6 and 5.8. Also for the general simulation settings, the turbulence model and time-step remain the same as used in the study presented in Chapter 5.

For the coupled translational motions (stream-wise/transverse), the amplitude ratio, R_A , is defined as:

$$R_A = \frac{A_s}{A_t} \quad (7.1)$$

Three amplitude ratios are considered: stream-wise motion (constant amplitude of $0.25c$ as used in Section 5.2) being equal, double and half of the transverse motion, both for positive and negative direction $\pm x$ (see Tab. 7.1 for the all conditions simulated). Two

phases relative to stream-wise motion are considered ($\phi = 0^\circ$ and $\phi = 90^\circ$). To give a clear sense of the coupled stream-wise/transverse motion, the trajectories followed by the airfoil are specified in Tab.7.2. The trajectories are shown schematically in Fig. 7.1. The oscillation path shape will be the same for both the leading edge (LE) and trailing edge (TE), since only translational motions are involved.

Coupling	Motion amplitudes		Amplitude ratio $R_A = A_s/A_t$	Phase
	Stream-wise	Transverse		
Stream-wise/Transverse	$A_s = 0.25c$	$A_t = 0.25c$	$R_A = 1$	$\phi = 0^\circ$
Stream-wise/Transverse	$A_s = 0.25c$	$A_t = 0.25c$	$R_A = 1$	$\phi = 90^\circ$
Stream-wise/Transverse	$A_s = 0.25c$	$A_t = 0.5c$	$R_A = 0.5$	$\phi = 0^\circ$
Stream-wise/Transverse	$A_s = 0.25c$	$A_t = 0.5c$	$R_A = 0.5$	$\phi = 90^\circ$
Stream-wise/Transverse	$A_s = 0.25c$	$A_t = 0.125c$	$R_A = 2$	$\phi = 0^\circ$
Stream-wise/Transverse	$A_s = 0.25c$	$A_t = 0.125c$	$R_A = 2$	$\phi = 90^\circ$
Stream-wise/Transverse	$A_s = -0.25c$	$A_t = 0.25c$	$R_A = -1$	$\phi = 0^\circ$
Stream-wise/Transverse	$A_s = -0.25c$	$A_t = 0.25c$	$R_A = -1$	$\phi = 90^\circ$
Stream-wise/Transverse	$A_s = -0.25c$	$A_t = 0.5c$	$R_A = -0.5$	$\phi = 0^\circ$
Stream-wise/Transverse	$A_s = -0.25c$	$A_t = 0.5c$	$R_A = -0.5$	$\phi = 90^\circ$
Stream-wise/Transverse	$A_s = -0.25c$	$A_t = 0.125c$	$R_A = -2$	$\phi = 0^\circ$
Stream-wise/Transverse	$A_s = -0.25c$	$A_t = 0.125c$	$R_A = -2$	$\phi = 90^\circ$

Table 7.1: Combinations of motion amplitude and phase for the coupled stream-wise/transverse motion.

Amplitude ratio	Phase	Trajectory
Positive	$\phi = 0^\circ$	South-West/North-East path (see Fig. 7.1(a))
Negative	$\phi = 0^\circ$	South-East/North-West path (see Fig. 7.1(b))
Positive	$\phi = 90^\circ$	Clockwise loop (see Fig. 7.1(c))
Negative	$\phi = 90^\circ$	Counter-clockwise loop (see Fig. 7.1(d))

Table 7.2: Trajectories followed by the airfoil for the coupled stream-wise/transverse motion.

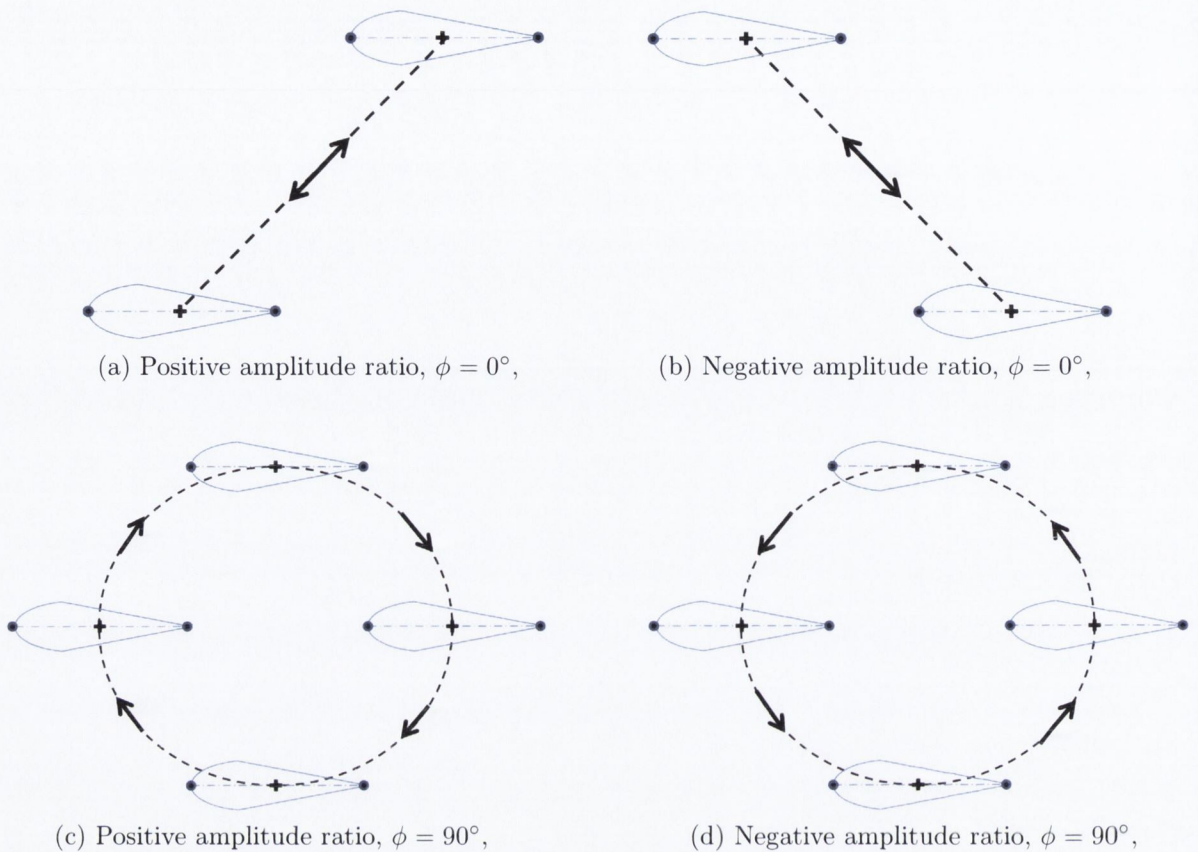


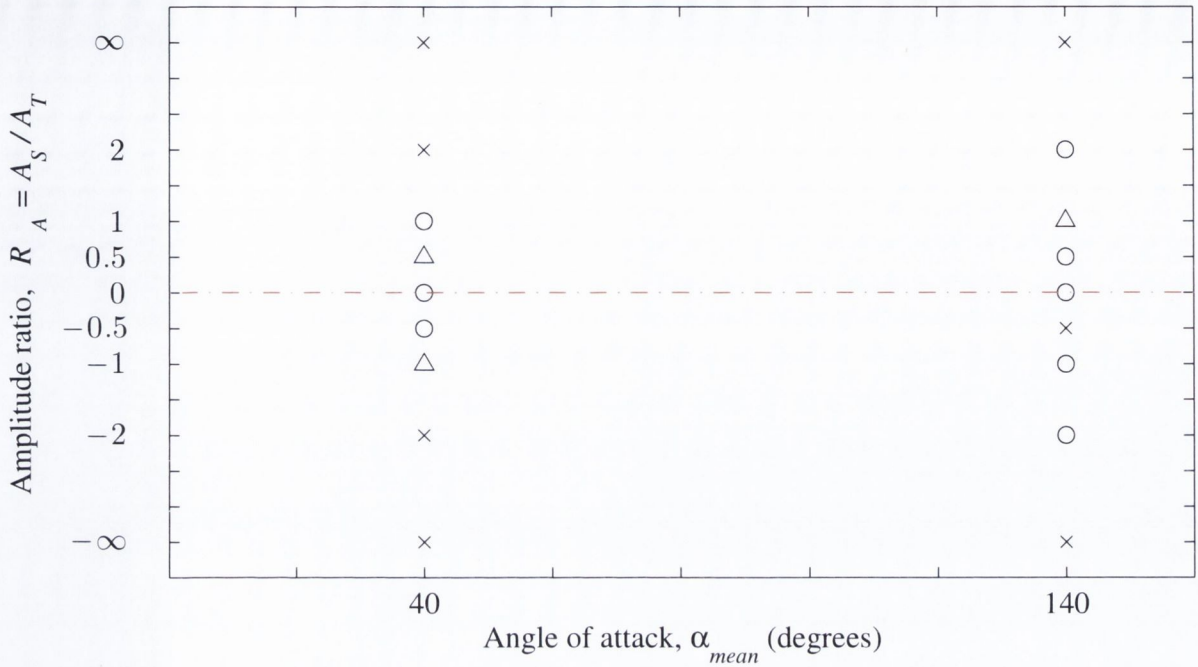
Figure 7.1: Trajectories followed by the airfoil (arbitrary configuration) for the coupled stream-wise/transverse motion, for different sign of the amplitude ratio and different phase angle.

The effect the stream-wise motion has on the transverse lock-in behaviour is illustrated in Fig. 7.2, for $\alpha_{mean} = 40^\circ$ and $\alpha_{mean} = 140^\circ$, for both $\phi = 0^\circ$ (Fig. 7.2(a)) and $\phi = 90^\circ$ (Fig. 7.2(b)). The conditions for $R_A = 0$ and $R_A = \pm\infty$ are taken from Figs. 5.10 and 5.16, being respectively a pure transverse motion (locked-in) and a pure stream-wise motion (locked-out). It can be seen that, in general, the stream-wise motion effect is more significant for $\alpha_{mean} = 40^\circ$. Or conversely, the transverse lock-in behaviour is more resilient from being affected by the stream-wise motion for $\alpha_{mean} = 140^\circ$. This seems to be due to the leading trailing edge being a fixed flow separation point. In fact the stream-wise motion on the configuration at $\alpha_{mean} = 40^\circ$ enhances the movement of the flow separation point/flow reattachment point on the rounded leading edge (upper side of the airfoil), limiting the vortex shedding synchronisation to happen. This is mostly true for $R_A = \pm 2$. Other than compare the two incidences considered, one can look at the difference in behaviour caused by the phase between the two motions. Broadly, it

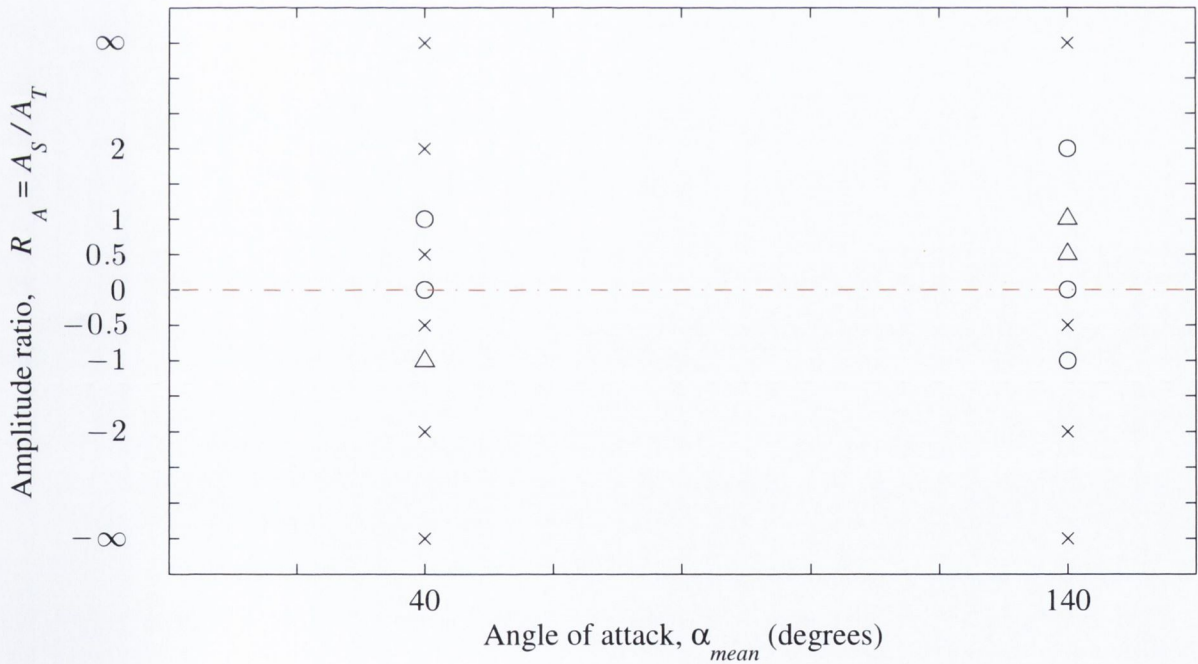
can be seen that for $\phi = 90^\circ$ the risk of synchronisation is slightly reduced, especially for $\alpha_{mean} = 40^\circ$. Again, this could be related to a more significant movement of the flow separation point on the leading edge (caused by the “circular” motion associated with $\phi = 90^\circ$).

Comparisons of the flow field can be made between different cases simulated to understand the different behaviour/oscillation caused by combinations of different motion amplitude, sense, direction and phase. For example, a sensible comparison could be made for four $\alpha_{mean} = 140^\circ$ cases: $R_A = \pm 2$ for both $\phi = 0^\circ$ (see Fig. 7.2(a)) and $\phi = 90^\circ$ (see Fig. 7.2(b)). Figure 7.3 shows the instantaneous vorticity field corresponding to these four sample cases. Figures 7.3(a), 7.3(b) and 7.3(c) illustrate all lock-in conditions. The wake structure is organised, yet presenting differences in pattern due to the different path travelled by the airfoil. Comparing Figs. 7.3(a) and 7.3(c), it can be seen that the phase $\phi = 90^\circ$ makes the first few pairs of vortices slightly more aligned. Figure 7.4 shows a close-up of the vorticity in the near field, over an oscillation cycle, of the three lock-in cases seen in Fig. 7.3: the left column corresponds to Fig. 7.3(a), the middle column corresponds to Fig. 7.3(b) and the right column corresponds to Fig. 7.3(c). Comparing the first and the third column, it can be seen that for $\phi = 90^\circ$, a sort of entrainment of the counter-clockwise vortex into the clockwise one occurs, until it is eventually released and travels further. This is due to the “circulatory” oscillation of the airfoil driven by the phase $\phi = 90^\circ$ between the stream-wise and the transverse motions. Comparing Figs. 7.3(a) and 7.3(b), the negative sign on the stream-wise motion ($R_A = -2$) causes the vortex street to be wider, with vortices less aligned and more distant. This behaviour is explained by the opposite sense of oscillation in the x direction: $R_A = 2$ (Fig. 7.3(a)) means that the airfoil is moving on a trajectory along its chord, while for $R_A = -2$ (Fig. 7.3(b)) the airfoil is moving on a trajectory perpendicularly to its chord. This leads to a movement that “elongates” (during the backward/upward stroke) and “pushes” (during the forward/downward stroke) the formed vortex, in particular the clockwise (negative) one. Hence, the overall wider effect seen in Fig. 7.3(b). Details in the near flow field of this behaviour can be seen in Fig. 7.4 (looking at the left and middle columns). The wake of a lock-out condition is illustrated in Fig. 7.3(d). As seen already for other examples in Chapter 5, the vortex street structure is not organised/periodic. The irregularity of the

vortex shedding can be seen in Fig. 7.5, showing a close-up of the vorticity in the near field over a portion of the time history. Figure 7.6 shows details of the airfoil motion over the considered time history: lift force coefficient in Fig. 7.6(a) and displacement in Fig. 7.6(b), with labelled positions corresponding to letters in Figs. 7.5). The main difference with the other three lock-in cases seen above, is that the counter-clockwise (positive) vortex is formed when the airfoil is moving both backward and forward (while for the three lock-in cases the counter-clockwise (positive) vortex is formed always when the airfoil is moving backward). The “pushing down” action (for example Figs. 7.5(m), 7.5(n), 7.5(o)) while the vortex at the trailing edge is forming may be the explanation for this difference in behaviour, i.e. preventing the generation of a periodic vortex shedding pattern.

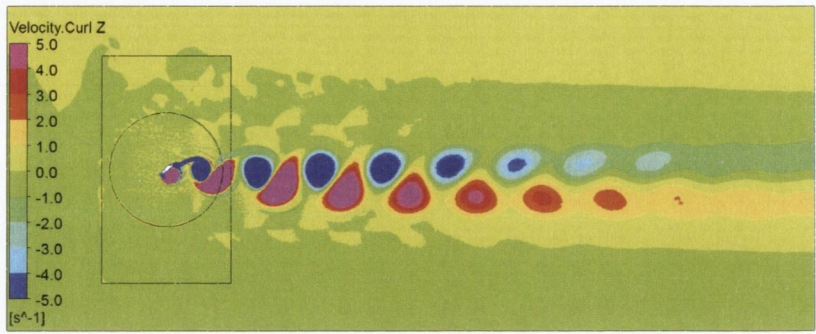


(a) Phase angle, $\phi = 0^\circ$,

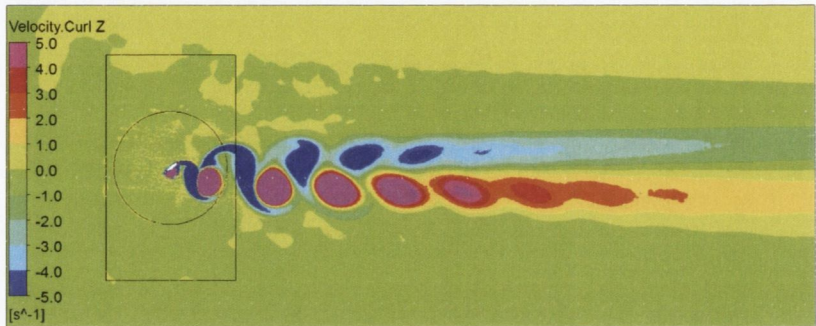


(b) Phase angle, $\phi = 90^\circ$.

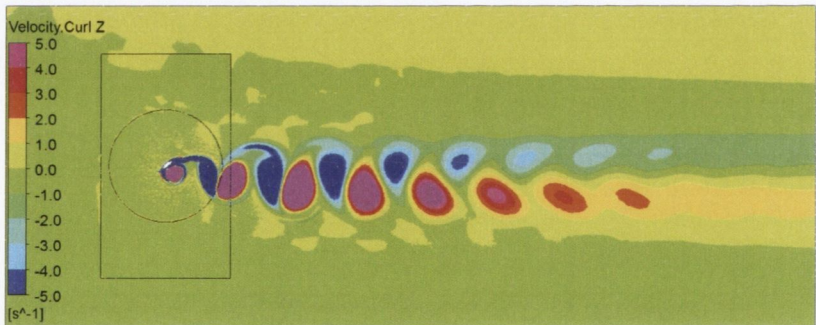
Figure 7.2: Synchronisation map for positive angles of attack, coupled stream-wise/transverse motion at $A_s = \pm 0.25c$ for two phase angles: ○, lock-in; △, pseudo-lock-in (periodicity with sub-harmonics); ×, lock-out.



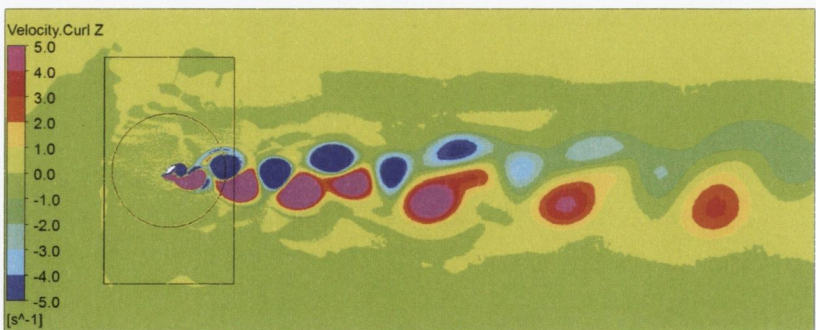
(a) $R_A = 2, \phi = 0^\circ$. Lock-in,



(b) $R_A = -2, \phi = 0^\circ$. Lock-in,



(c) $R_A = 2, \phi = 90^\circ$. Lock-in,



(d) $R_A = -2, \phi = 90^\circ$. Lock-out.

Figure 7.3: Instantaneous vorticity field for the coupled stream-wise/transverse motion at different amplitude ratio and phase, $\alpha_{mean} = 140^\circ, r = 1.1$. ■, counter-clockwise (positive) vorticity; ■, clockwise (negative) vorticity.

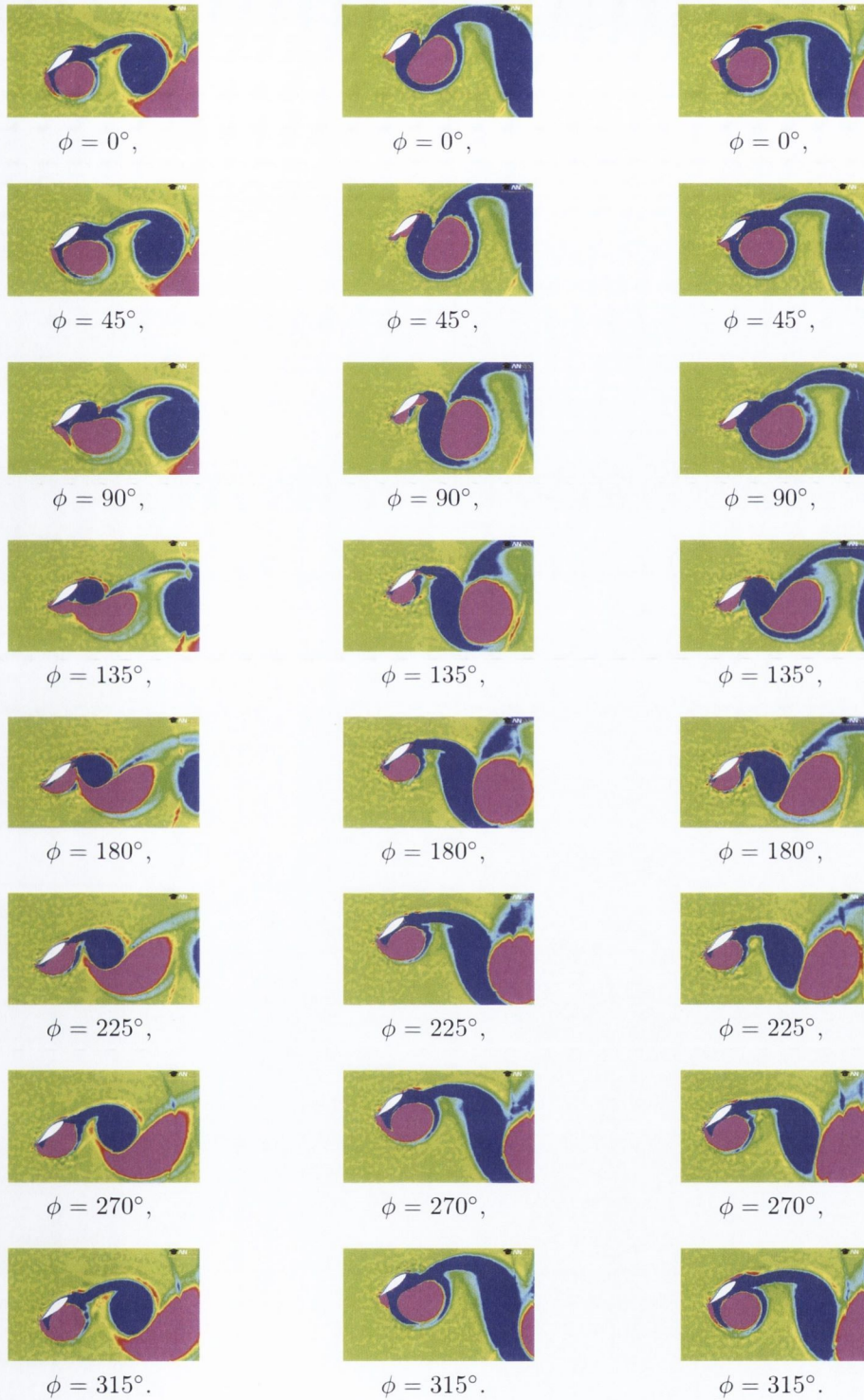


Figure 7.4: Close-up of the instantaneous vorticity field for coupled stream-wise/transverse motion over an oscillation cycle at $\alpha_{mean} = 140^\circ$, $r = 1.1$. Different paths of motion, lock-in conditions: left column, $R_A = 2$, $\phi = 0^\circ$; middle column, $R_A = -2$, $\phi = 0^\circ$; right column, $R_A = 2$, $\phi = 90^\circ$. ■, counter-clockwise (positive) vorticity; ■, clockwise (negative) vorticity.

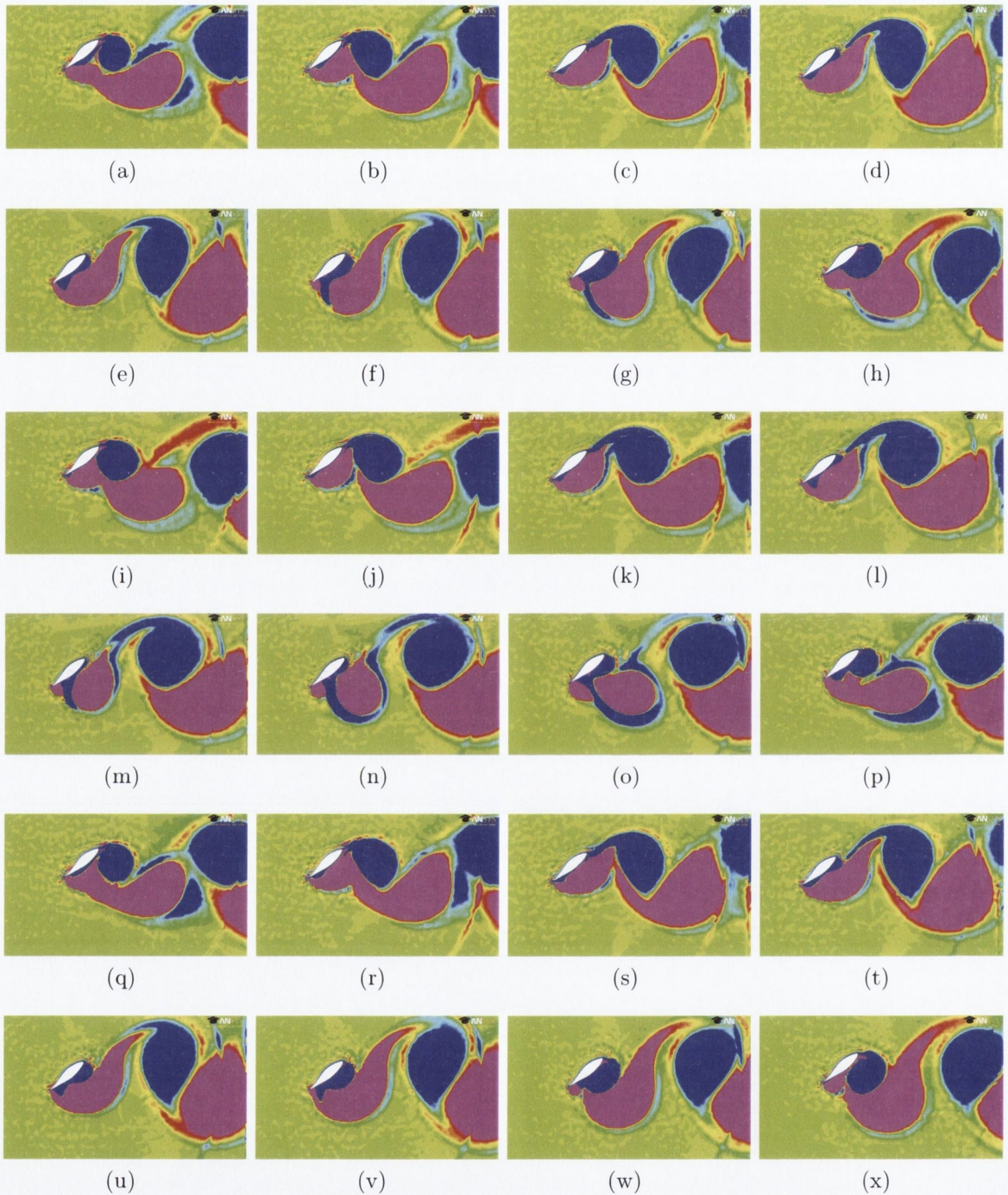
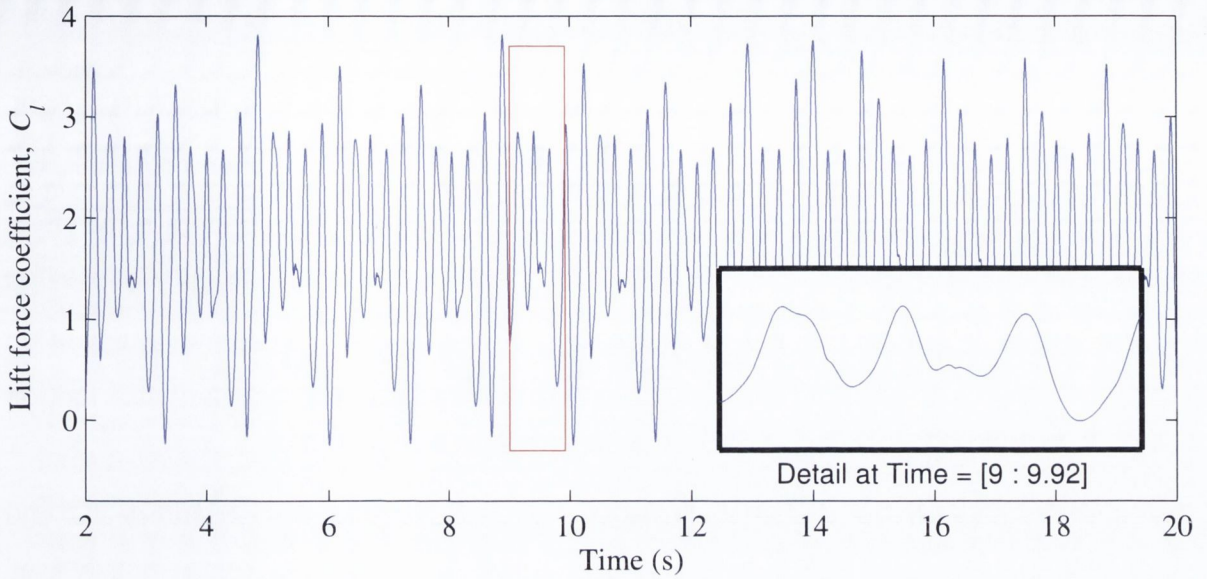
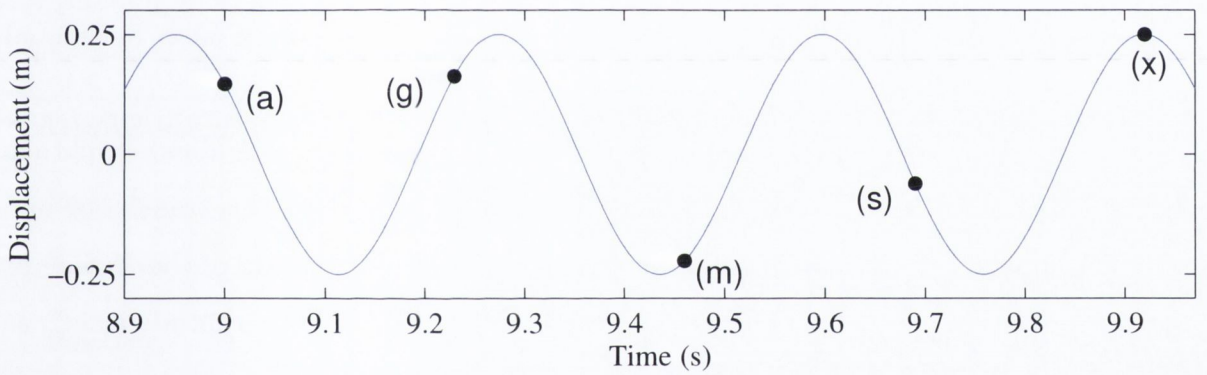


Figure 7.5: Close-up of the instantaneous vorticity field coupled stream-wise/transverse motion over a portion of time history ($\tau = [131 \rightarrow 145]$), $\alpha_{mean} = 140^\circ$, $r = 1.1$; lock-out condition, $R_A = -2$, $\phi = 90^\circ$. ■, counter-clockwise (positive) vorticity; ■, clockwise (negative) vorticity.



(a) Lift force coefficient time trace,



(b) Displacement time trace.

Figure 7.6: Portion of the time history used in Fig. 7.5: (a), lift force coefficient time trace with a zoom-in of the history portion; (b) displacement for zoom window, points labelled with letters correspond to the airfoil positions in Figs. 7.5.

7.2 Coupled stream-wise/pitching motion

A series of two-dimensional unsteady simulations of the flow around the NREL S809 airfoil moving in a coupled stream-wise/pitching motion (translation, x and rotation, α), have been performed, for $\alpha_{mean} = 40^\circ$ and $\alpha_{mean} = 140^\circ$, in order to investigate the effect the stream-wise motion has on the pitching lock-in behaviour. The sample case used is the frequency ratio $r = 1.1$ for both of the two angles of attack, i.e. using a unique motion frequency $f_s = f_p$ at which synchronisation does not occur for the stream-wise motion while it does for the pitching one.

The motion function in the UDF includes both laws of motion presented in Eqs. 5.6 and 5.4. As a rotational motion is involved (pitching motion), the fluid domain previously used in Section 5.1 is adopted (see Fig. 3.2). This is to facilitate rotational motion of the inner circular zone (as per the pitching motion in Section 5.1, with a sliding mesh technique) while it translates stream-wise (deforming mesh technique).

For the coupled stream-wise/pitching motion, it is not sensible to talk about amplitude ratio in the same way as stream-wise/transverse motion (Eq. 7.1), since a translation and a rotation are involved. Nonetheless, considering the rotational motion of the leading or trailing edge as a reference point, it is still meaningful to define an “amplitude ratio”, as follows:

$$R_A = \frac{A_s}{c|\alpha_{ampl}|} \quad (7.2)$$

where the stream-wise amplitude is normalised with the chord of the airfoil, and $c|\alpha_{ampl}|$ is twice the translational amplitude of the leading/trailing edge due to the pitching motion (α_{ampl} is expressed in radians).

Two amplitude ratios are considered. The stream-wise amplitude, $|A_s| = 0.25c$, is kept constant (as done in Section 7.1) for positive and negative values; the pitching amplitude considered is 7° (as used in Section 5.1) and 3.5° (see Tab. 7.3). The phase between the two different motions is considered, $\phi = 0^\circ$ and $\phi = 90^\circ$. To give a clear sense of the coupled stream-wise/pitching motion, the trajectories followed by the airfoil are specified in Tab. 7.4 and illustrated schematically in Fig. 7.7. The oscillation path is distinguished,

when needed, between leading edge (LE) and trailing edge (TE), since a rotational motion is involved.

Coupling	Motion amplitudes		Amplitude ratio $R_A = A_s/(c \alpha_{ampl})$	Phase
	Stream-wise	Pitching		
Stream-wise/Pitching	$A_s = 0.25c$;	$\alpha_{ampl} = 7^\circ$	$R_A = 2.05$	$\phi = 0^\circ$
Stream-wise/Pitching	$A_s = 0.25c$;	$\alpha_{ampl} = 7^\circ$	$R_A = 2.05$	$\phi = 90^\circ$
Stream-wise/Pitching	$A_s = 0.25c$;	$\alpha_{ampl} = 3.5^\circ$	$R_A = 4.1$	$\phi = 0^\circ$
Stream-wise/Pitching	$A_s = 0.25c$;	$\alpha_{ampl} = 3.5^\circ$	$R_A = 4.1$	$\phi = 90^\circ$
Stream-wise/Pitching	$A_s = -0.25c$;	$\alpha_{ampl} = 7^\circ$	$R_A = -2.05$	$\phi = 0^\circ$
Stream-wise/Pitching	$A_s = -0.25c$;	$\alpha_{ampl} = 7^\circ$	$R_A = -2.05$	$\phi = 90^\circ$
Stream-wise/Pitching	$A_s = -0.25c$;	$\alpha_{ampl} = 3.5^\circ$	$R_A = -4.1$	$\phi = 0^\circ$
Stream-wise/Pitching	$A_s = -0.25c$;	$\alpha_{ampl} = 3.5^\circ$	$R_A = -4.1$	$\phi = 90^\circ$

Table 7.3: Combinations of motion amplitudes and phase for the coupled stream-wise/pitching motion.

Amplitude ratio	Phase	Trajectory
Positive	$\phi = 0^\circ$	LE: parabolic upward path (see Fig. 7.7(a))
Negative	$\phi = 0^\circ$	LE: parabolic downward path (see Fig. 7.7(b))
Positive	$\phi = 90^\circ$	LE: counter-clockwise loop TE: clockwise loop (see Fig. 7.7(c))
Negative	$\phi = 90^\circ$	LE: clockwise loop TE: counter-clockwise loop (see Fig. 7.7(d))

Table 7.4: Trajectories followed by the airfoil for the coupled stream-wise/pitching motion.

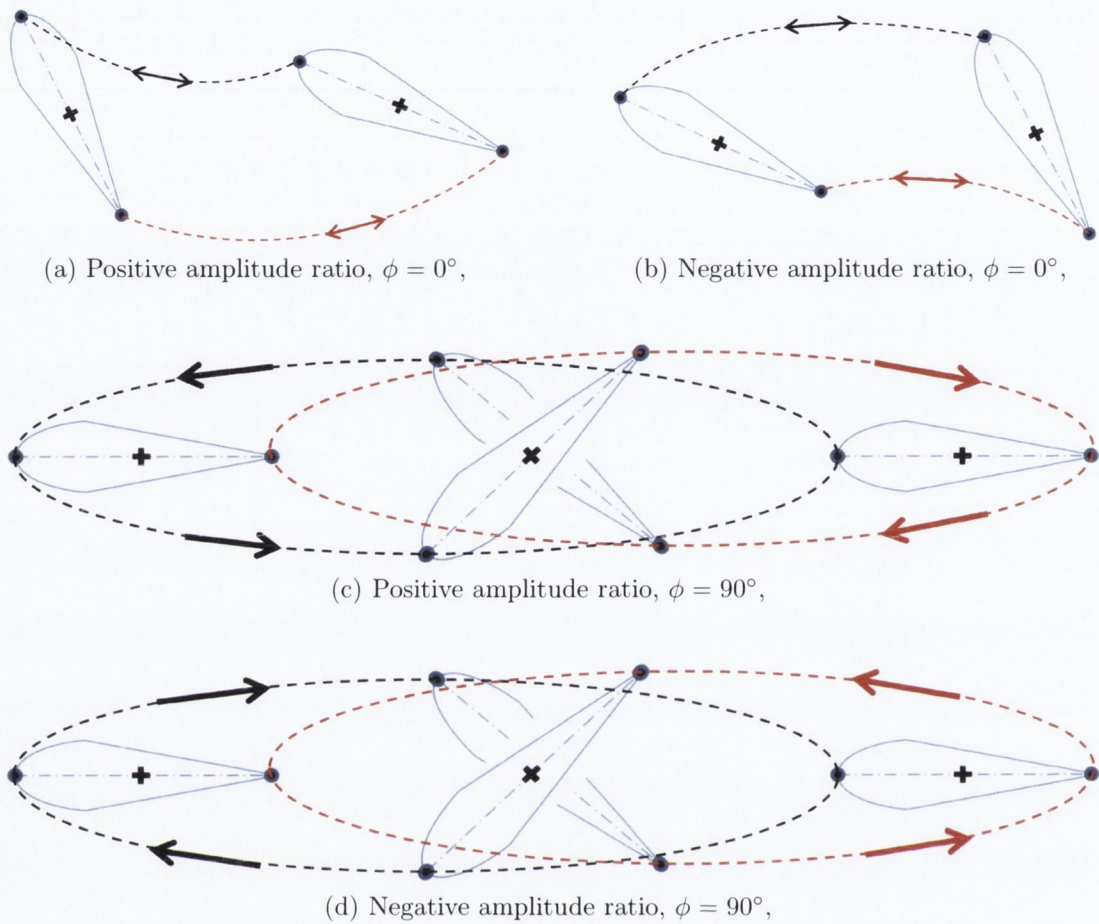
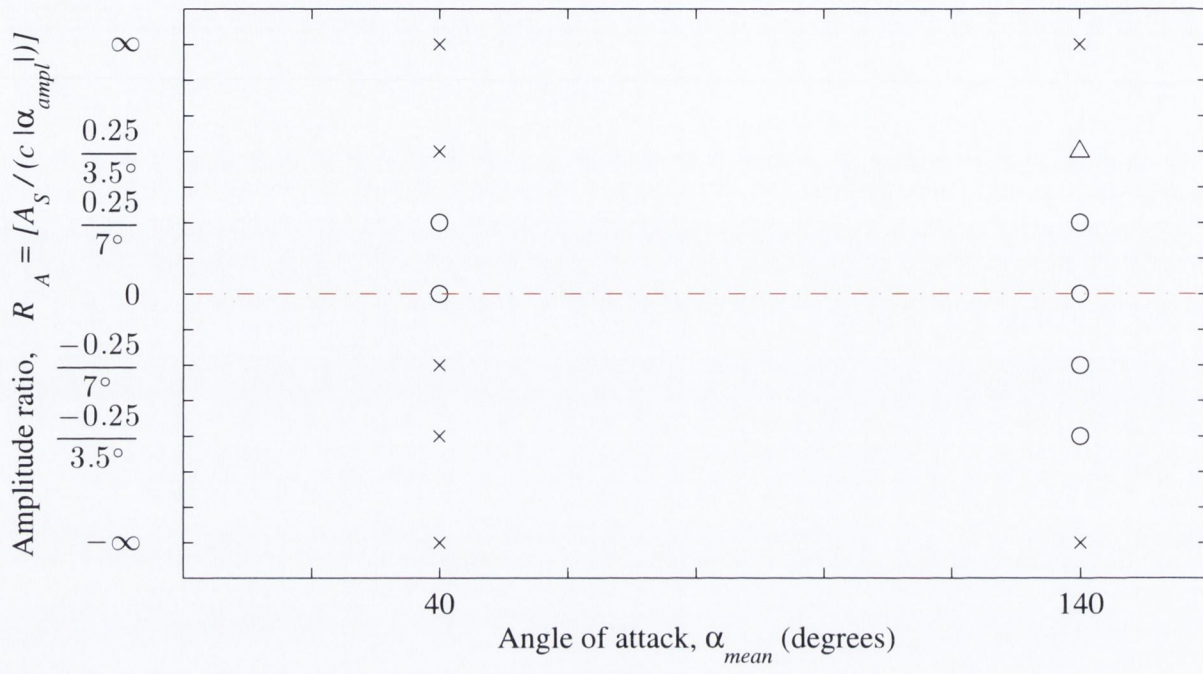


Figure 7.7: Trajectories followed by the airfoil (arbitrary configuration) for the coupled stream-wise/pitching motion, for different sign of the amplitude ratio and different phase angle. --, LE trajectory; - -, TE trajectory.

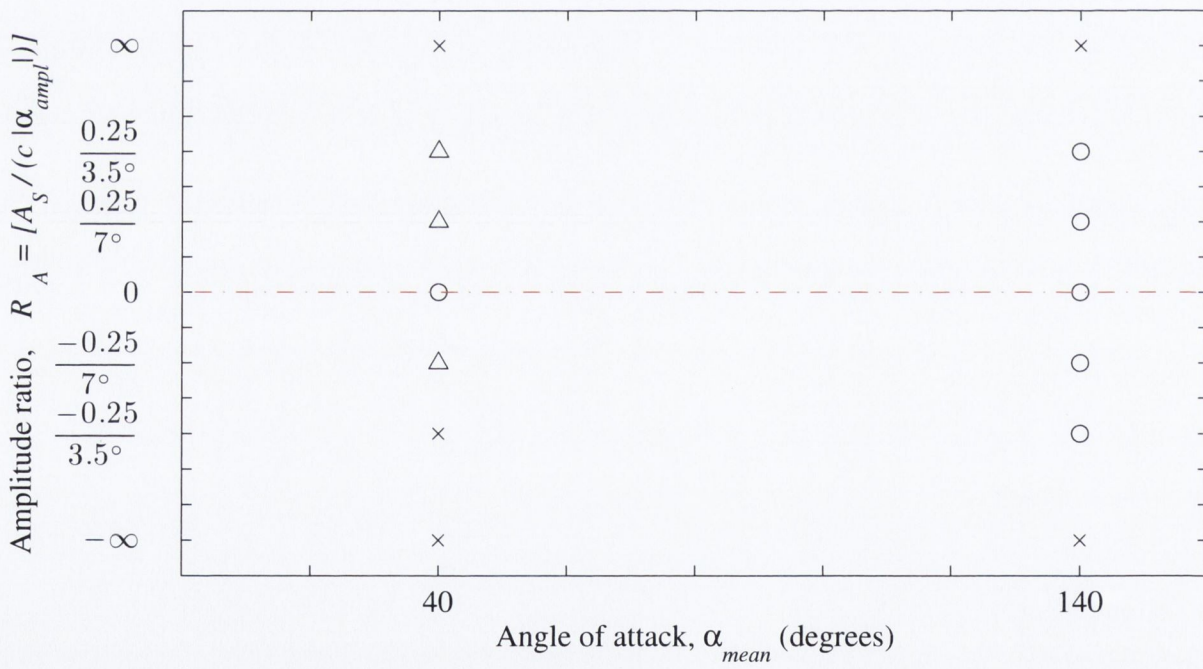
The effect the stream-wise motion has on the pitching lock-in behaviour is illustrated in Fig. 7.8, for $\alpha_{mean} = 40^\circ$ and $\alpha_{mean} = 140^\circ$, for both $\phi = 0^\circ$ (Fig. 7.8(a)) and $\phi = 90^\circ$ (Fig. 7.8(b)). The conditions for $R_A = 0$ and $R_A = \pm\infty$ are taken from Figs. 5.10 and 5.3, being respectively a pure pitching motion (locked-in) and a pure stream-wise motion (locked-out). As seen for the coupled stream-wise/transverse motion in Section 7.1, the pitching lock-in behaviour is more resilient from being affected by the stream-wise motion for $\alpha_{mean} = 140^\circ$. This seems to be due to the leading trailing edge being a fixed flow separation point. As advanced in Section 5.1, for airfoil's configurations with a defined leading edge separation point (i.e. configurations with higher characteristic length or trailing edge upwind) the wake seems to be more resilient against external influences. This may explain why the stream-wise motion effect is less significant in modifying the

lock-in behaviour for $\alpha_{mean} = 140^\circ$ than for $\alpha_{mean} = 40^\circ$. Looking at the phase effect for $\alpha_{mean} = 40^\circ$, contrary to what was observed for the coupled stream-wise/transverse motion in Section 7.1, the $\phi = 90^\circ$ case seems to make the wake more resilient to the stream-wise effect.

Comparisons can be made between different cases simulated to understand the different behaviour caused by combinations of different motion amplitude, sense, direction and phase. For example, a sensible comparison could be made for four $\alpha_{mean} = 40^\circ$ cases: $A_s = \pm 0.25c$ and $\alpha_{ampl} = 7^\circ$, for both $\phi = 0^\circ$ (see Fig. 7.8(a)) and $\phi = 90^\circ$ (see Fig. 7.8(b)). Figure 7.9 shows the instantaneous vorticity field corresponding to these four sample cases. All three observed behaviours are present: lock-in condition (Fig. 7.9(a)), lock-out condition (Fig. 7.9(b)) and pseudo-lock-in condition with sub-harmonics (Figs. 7.9(c) and 7.9(d)). The wakes associated with a pseudo-lock-in condition (Figs. 7.9(c) and 7.9(d)) appear to be different in contrast to the pseudo-lock-in cases seen in Chapter 5. For example, as presented previously in Fig. 5.14(b), the vortex street seems to achieve a sort of periodic pattern in the far field, thanks to the dominant frequency coinciding with the excitation frequency (see Fig. 5.13(d)). In Fig. 5.14(d) the wake resembles a lock-out condition, due to the dominant frequency which is non integer multiple of the excitation frequency (see Fig. 5.13(h)). Figures 7.9(c) and 7.9(d) show vortex streets which are not periodic (neither in the far field), albeit not completely disorganised. What makes these two wakes looking like as a lock-out condition, yet not totally disorganised? Figure 7.10 may help to explain this, showing portions of the time record of the lift coefficient with the relative spectra corresponding to the cases in Figs. 7.9(c) and 7.9(d). Time is expressed dimensionless. Frequencies have been normalised with the static vortex shedding frequency, giving a non-dimensional frequency: $f^* = f/f_{v0}$. In contrast to what is shown in Figs. 5.13(d) and 5.13(h) (presence of one sub-harmonic only), it can be seen that for the case with $A_s = 0.25c$ two sub-harmonics are present (Fig. 7.10(b)) whereas three are present for the case with $A_s = -0.25c$ (Fig. 7.10(d)). The presence of multiple sub-harmonics indicate a high level of complexity in the vortex street. Dissipation denies the convecting wake enough time to establish strong periodicity. Nonetheless, the dominant frequency appears coincident with the excitation frequency, keeping the vortices pairs “together”; hence the wake does not become totally disorganised.

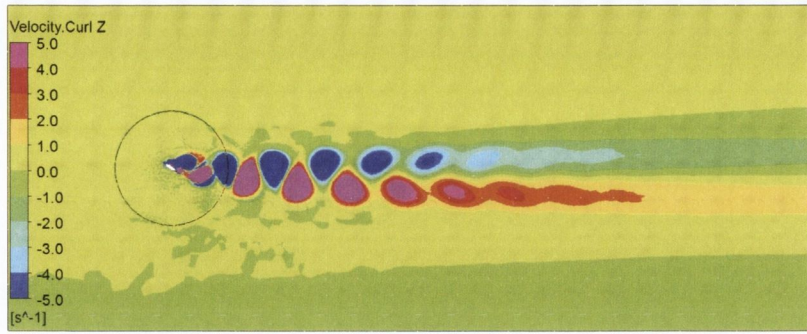


(a) Phase angle, $\phi = 0^\circ$,

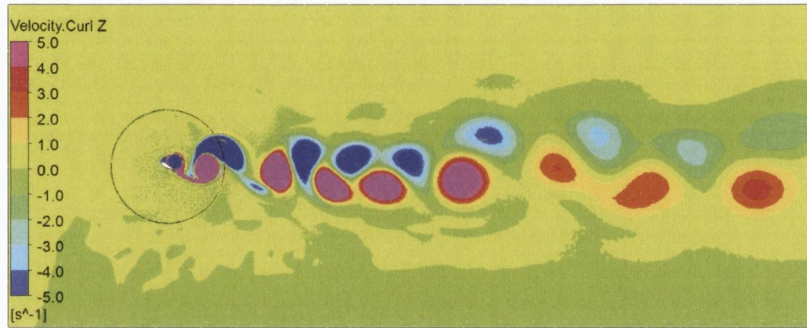


(b) Phase angle, $\phi = 90^\circ$.

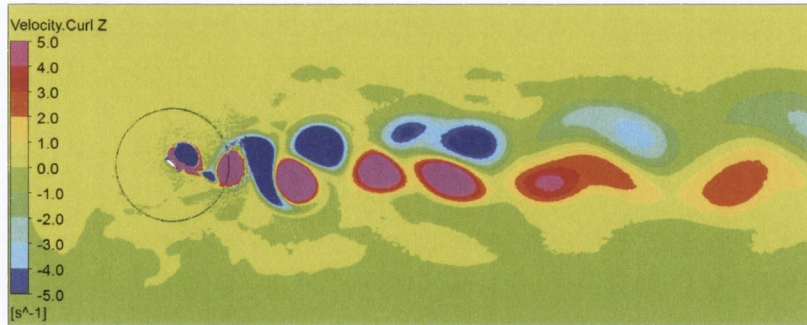
Figure 7.8: Synchronisation map for positive angles of attack, coupled stream-wise/pitching motion at $A_s = \pm 0.25c$: \circ , lock-in; \triangle , pseudo-lock-in (periodicity with sub-harmonics); \times , lock-out.



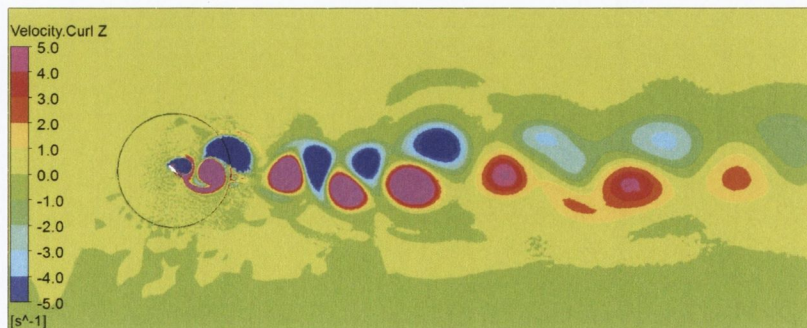
(a) $A_s = 0.25 c$, $\alpha_{ampl} = 7^\circ$, $\phi = 0^\circ$. Lock-in,



(b) $A_s = -0.25 c$, $\alpha_{ampl} = 7^\circ$, $\phi = 0^\circ$. Lock-out,



(c) $A_s = 0.25 c$, $\alpha_{ampl} = 7^\circ$, $\phi = 90^\circ$. Pseudo-lock-in,



(d) $A_s = -0.25 c$, $\alpha_{ampl} = 7^\circ$, $\phi = 90^\circ$. Pseudo-lock-in.

Figure 7.9: Instantaneous vorticity field for coupled stream-wise/pitching motion at different amplitudes and phase, $\alpha_{mean} = 40^\circ$, $r = 1.1$. ■, counter-clockwise (positive) vorticity; ■, clockwise (negative) vorticity.

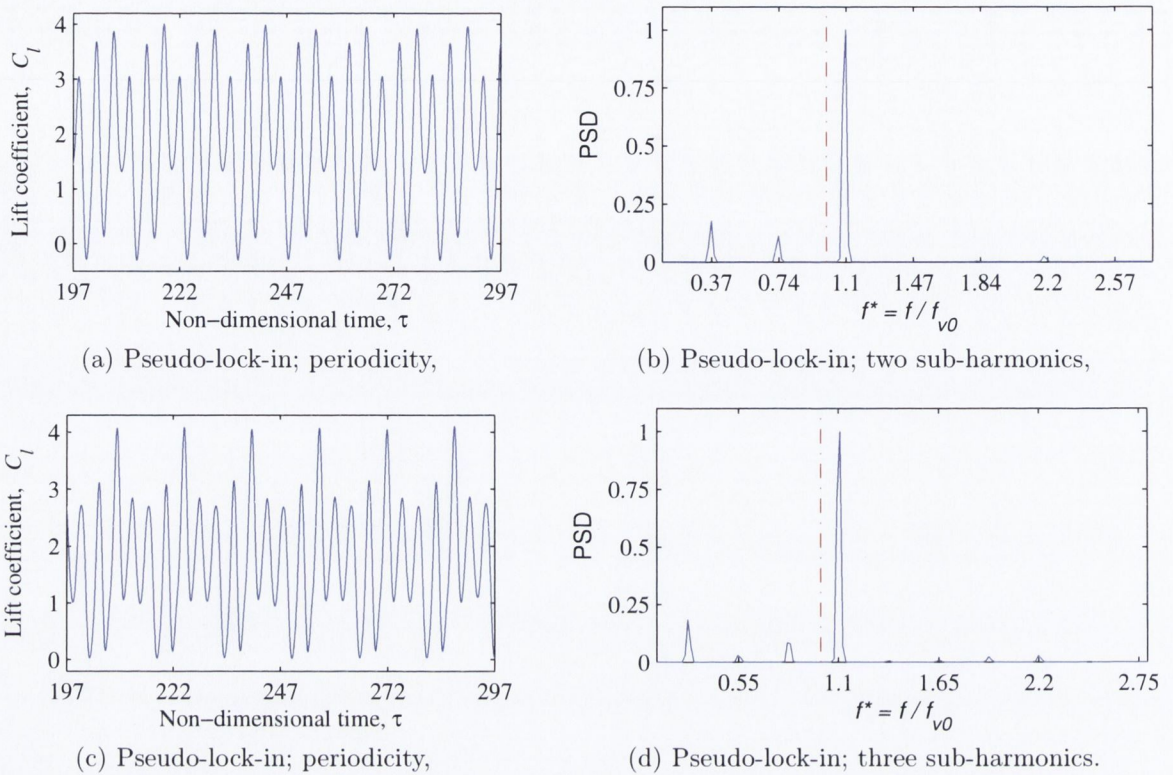


Figure 7.10: Detail of the time record (a, c) and spectrum (b, d) of the lift force coefficient. Coupled stream-wise/pitching motion with phase $\phi = 90^\circ$, for $A_s = 0.25c$ (a, b) and $A_s = -0.25c$ (c, d), at $\alpha_{mean} = 40^\circ$ and $r = 1.1$. PSD arbitrarily scaled. Dash-dot line indicates $f^* = 1$, corresponding to the static case.

Figures 7.11, 7.12, 7.13 and 7.14 show the close-up of the instantaneous vorticity in the near field for the four cases shown in Fig. 7.9. For a more straightforward understanding of these motions while looking at the figures, refer to Tab. 7.4 and Fig. 7.7. Figure 7.15 shows details of the airfoil motion over the considered time history: lift force coefficient in Fig. 7.15(a) (corresponding to the case of Fig. 7.13) and displacement for positive and negative stream-wise sense cases respectively in Figs. 7.15(b) and 7.15(c), with labelled positions corresponding to letters in Figs. 7.12, 7.13 and 7.14. In the lock-in cycle illustrated in Fig. 7.11, the counter-clockwise (positive) vortex at the trailing edge is always formed during the stream-wise motion in the sense downstream-to-upstream ($-x$, opposite to the freestream direction). The clockwise (negative) vortex is formed during the stream-wise downstream-to-upstream & pitching upstroke motions, and detached by the counter vorticity (positive) present near the leading edge during the pitching downstroke. Though it does not travel downstream due to the stream-wise motion upstream-

to-downstream (i.e. the airfoil keeps up with the vortex). Then the stream-wise motion switches to downstream-to-upstream causing the clockwise (negative) vortex to reattach, which finally detaches due to the counter vorticity (positive) formed at the trailing edge. The vortex is able to travel further as the stream-wise motion is downstream-to-upstream (i.e. opposite to the direction of the vortex convection). In the lock-out case illustrated in Fig. 7.12, the basic behaviour is similar to what observed for the lock-in condition above (Fig. 7.11). But the combination of the motions is different: now, the upstream-to-downstream motion is accompanied by the pitching upstroke which leads the trailing edge to dive upstream. As a consequence, some counter-clockwise (positive) vorticity is formed also during the stream-wise motion upstream-to-downstream. In addition, the elongation of the clockwise (negative) vortex during the stream-wise downstream-to-upstream motion is enhanced by the pitching downstroke, for example Figs. 7.12(u) \rightarrow (x). Also, the positive vorticity near the leading edge which tries to detach the negative vortex does not have the same strength every cycle of oscillation, causing the vortex shedding behaviour to be non regular (unlike the lock-in condition in Fig. 7.11). The effect of the phase $\phi = 90^\circ$ brings a new behaviour, illustrated in Fig. 7.13, leading to a pseudo-lock-in condition. In fact it happens that the clockwise (negative) vortex is completely detached by the counter vorticity near the leading edge, and is convected downstream without reattaching back, as illustrated in Figs. 7.13(a) \rightarrow (d). It can be seen that the elongation of the clockwise (negative) vortex is more significant (than what was observed for $\phi = 0^\circ$), as illustrated in Figs. 7.13(k) \rightarrow (w). Another difference with the lock-in scenario is that the positive vorticity experiences a similar process as the negative one. In Figs. 7.13(o) and 7.13(p) it can be seen that the positive vorticity at the trailing edge is detached by the negative vorticity, resulting in an entrainment of the vortex into another. In contrast to the negative vortex, the positive vortex does not travel downstream and it reattaches at the trailing edge. Eventually it experiences elongation during the downstream-to-upstream stream-wise motion, as the trailing edge dives upstream due to the pitching upstroke. This significant amount of positive vorticity created on the upper side of the airfoil enables the detachment and the shedding of the negative vortex from the leading edge, as shown in Figs. 7.13(a) \rightarrow (d). In Fig. 7.14 a similar behaviour can be deduced for the other pseudo-lock-in condition presented above (Fig. 7.9(d)).

On many of the figures presented in Chapters 5 and 7 showing the vorticity flow field, it can be seen that at the inner circular mesh boundary the contour plot is not smooth, appearing discontinuous. This effect is an artefact of the post-processing, as vorticity is a derived quantity. The lower part of Fig. 7.16 shows the instantaneous vorticity record along a horizontal line probe over a portion of the flow field (see the upper part of the figure). A vertical dash-dot line corresponds to the spacial location of the inner circular mesh boundary intersecting the horizontal line probe. This figure shows that the actual vorticity trace is continuous passing through the inner boundary, indicating that the CFD solution is not exhibiting localised distortion due to the meshing scheme.

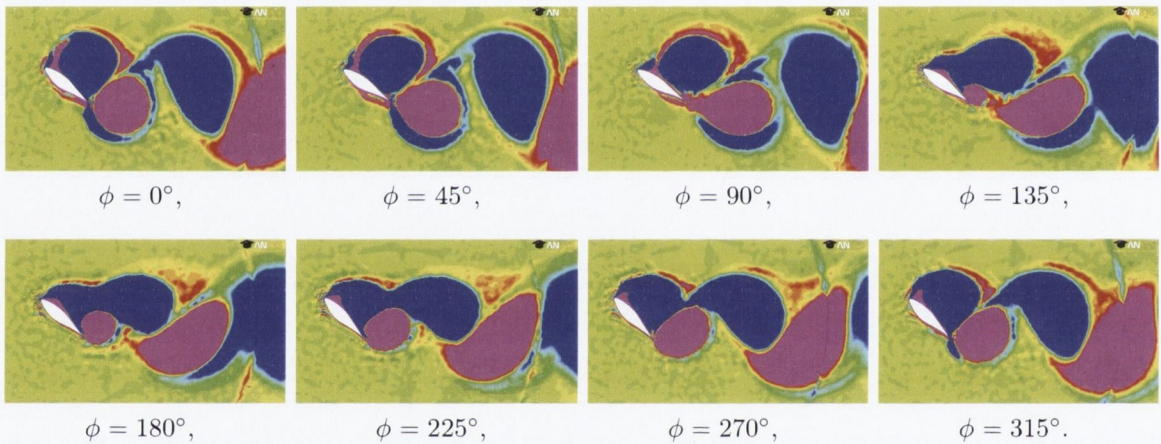


Figure 7.11: Close-up of the instantaneous vorticity field for the coupled stream-wise/pitching motion over an oscillation cycle at $\alpha_{mean} = 40^\circ$, $r = 1.1$. $A_s = 0.25c$, $\alpha_{ampl} = 7^\circ$, $\phi = 0^\circ$; Lock-in condition. ■, counter-clockwise (positive) vorticity; ■, clockwise (negative) vorticity.

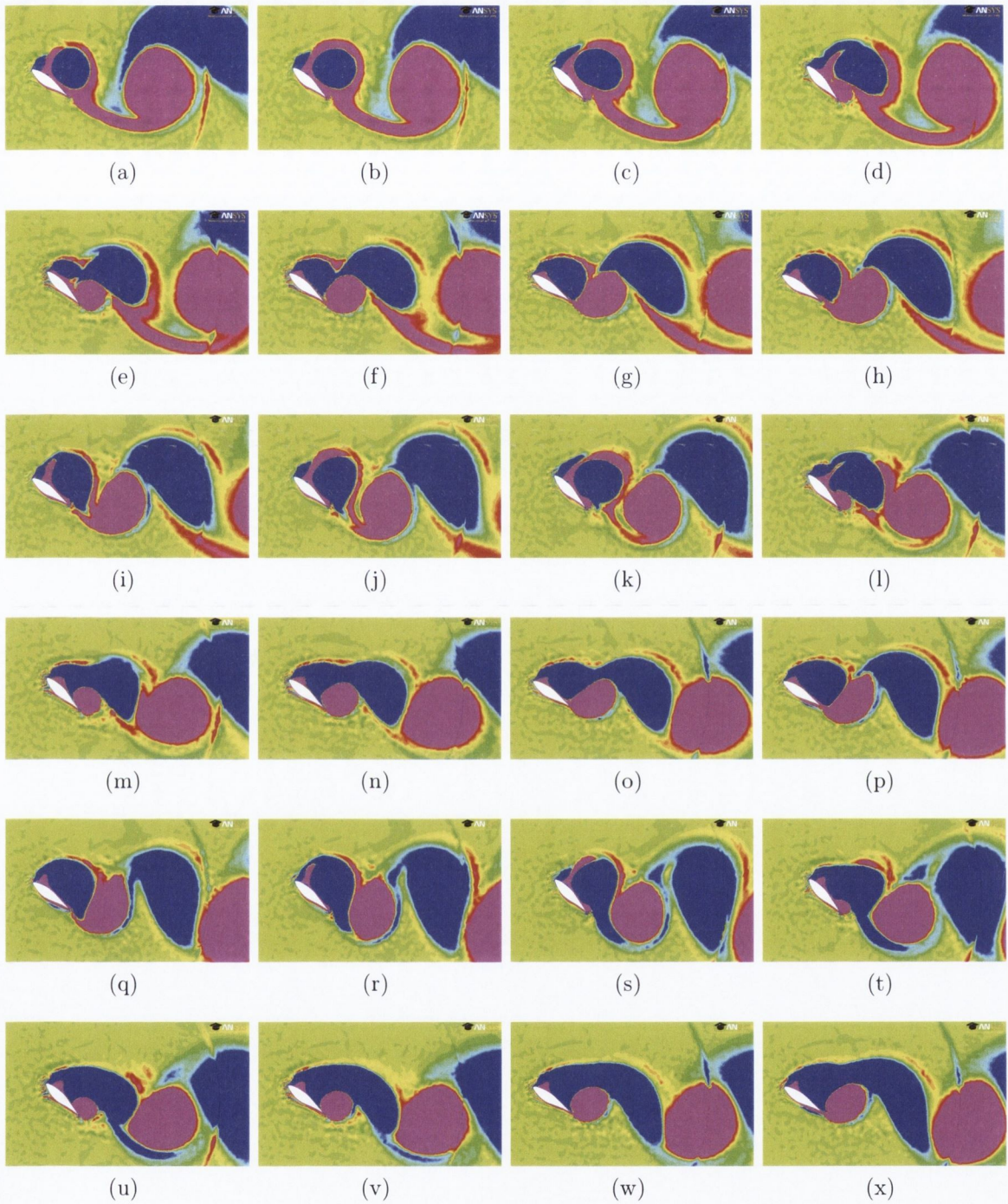


Figure 7.12: Close-up of the instantaneous vorticity field coupled stream-wise/pitching motion over a portion of time history ($\tau = [131 \rightarrow 143]$), $\alpha_{mean} = 40^\circ$, $r = 1.1$. $A_s = -0.25c$, $\alpha_{ampl} = 7^\circ$, $\phi = 0^\circ$; lock-out condition. ■, counter-clockwise (positive) vorticity; ■, clockwise (negative) vorticity.

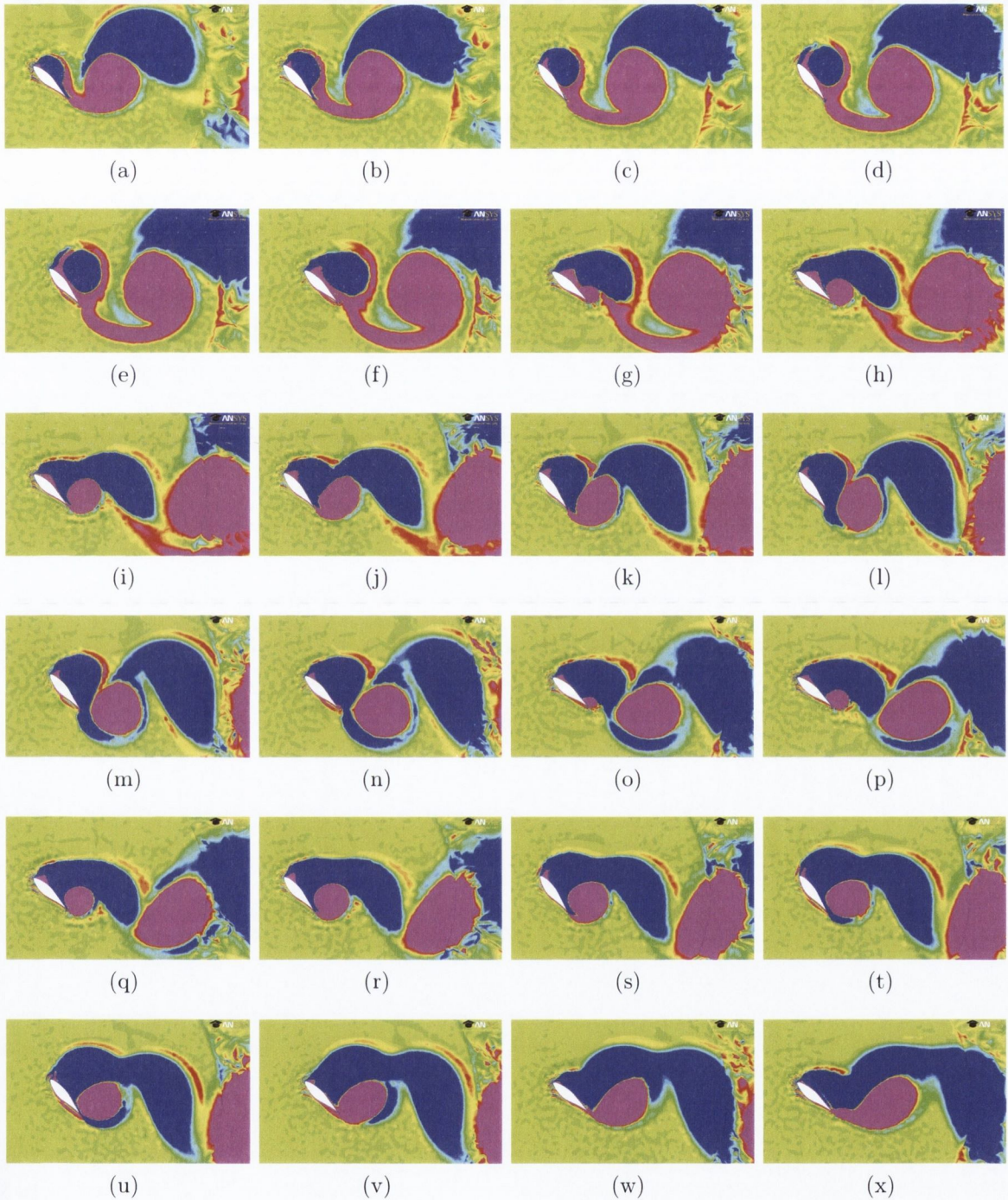
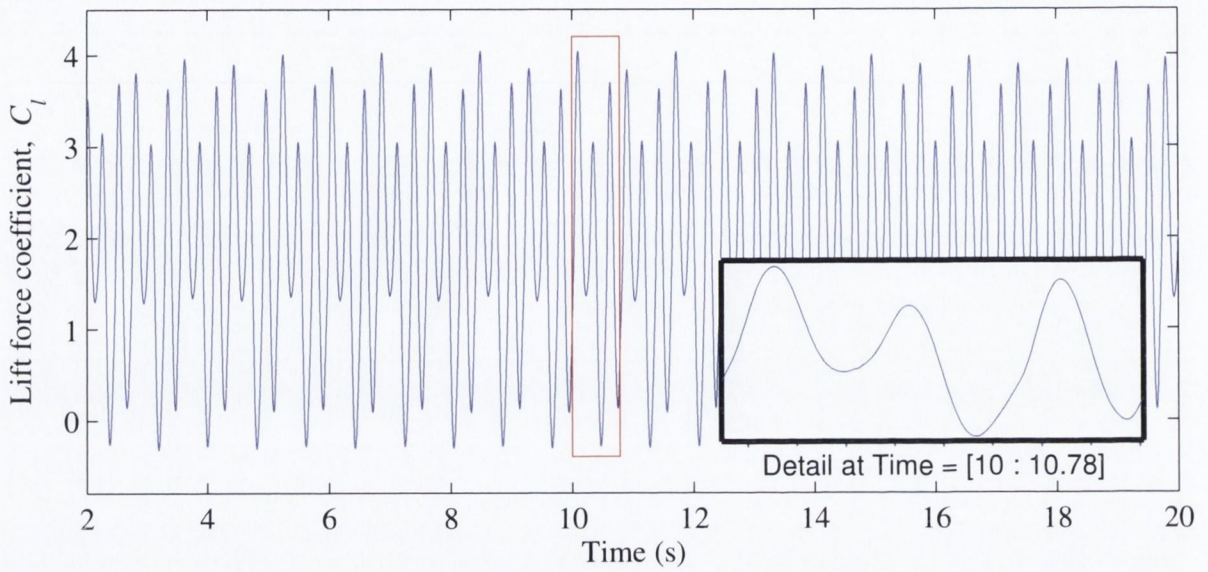
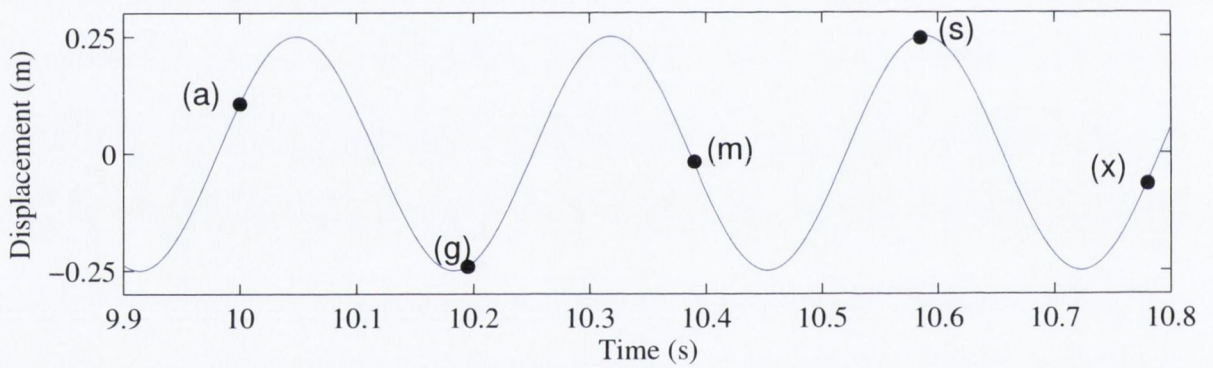


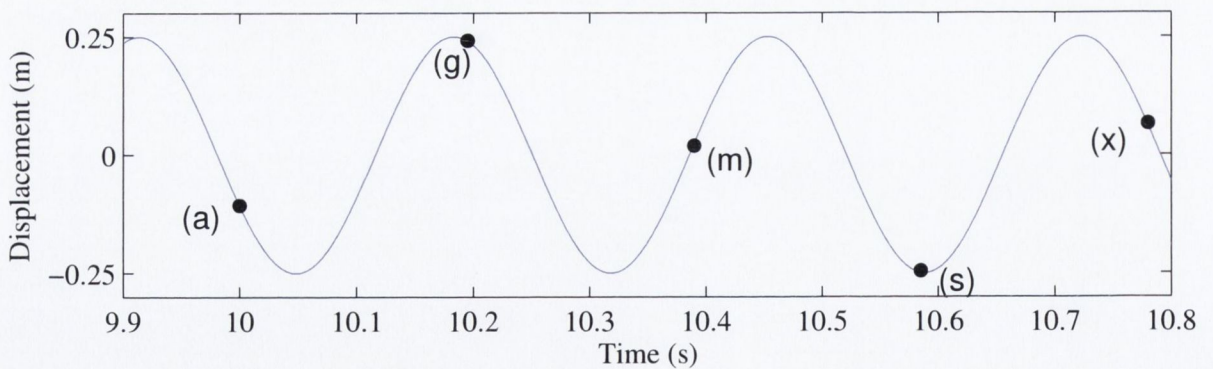
Figure 7.14: Close-up of the instantaneous vorticity field coupled stream-wise/pitching motion over a portion of time history ($\tau = [131 \rightarrow 143]$), $\alpha_{mean} = 40^\circ$, $r = 1.1$. $A_s = -0.25c$, $\alpha_{ampl} = 7^\circ$, $\phi = 90^\circ$; pseudo-lock-in with sub-harmonics condition. ■, counter-clockwise (positive) vorticity; ■, clockwise (negative) vorticity.



(a) Phase angle, $\phi = 0^\circ$,



(b) Displacement time trace, positive A_s ,



(c) Displacement time trace, negative A_s .

Figure 7.15: Portion of the time history used in Figs. 7.12, 7.13 and 7.14: (a), lift force coefficient time trace with a zoom-in of the history portion; (b, c) displacement (respectively for positive and negative stream-wise sense motion) for zoom window, points labelled with letters correspond to the airfoil positions in Figs. 7.12, 7.13 and 7.14.

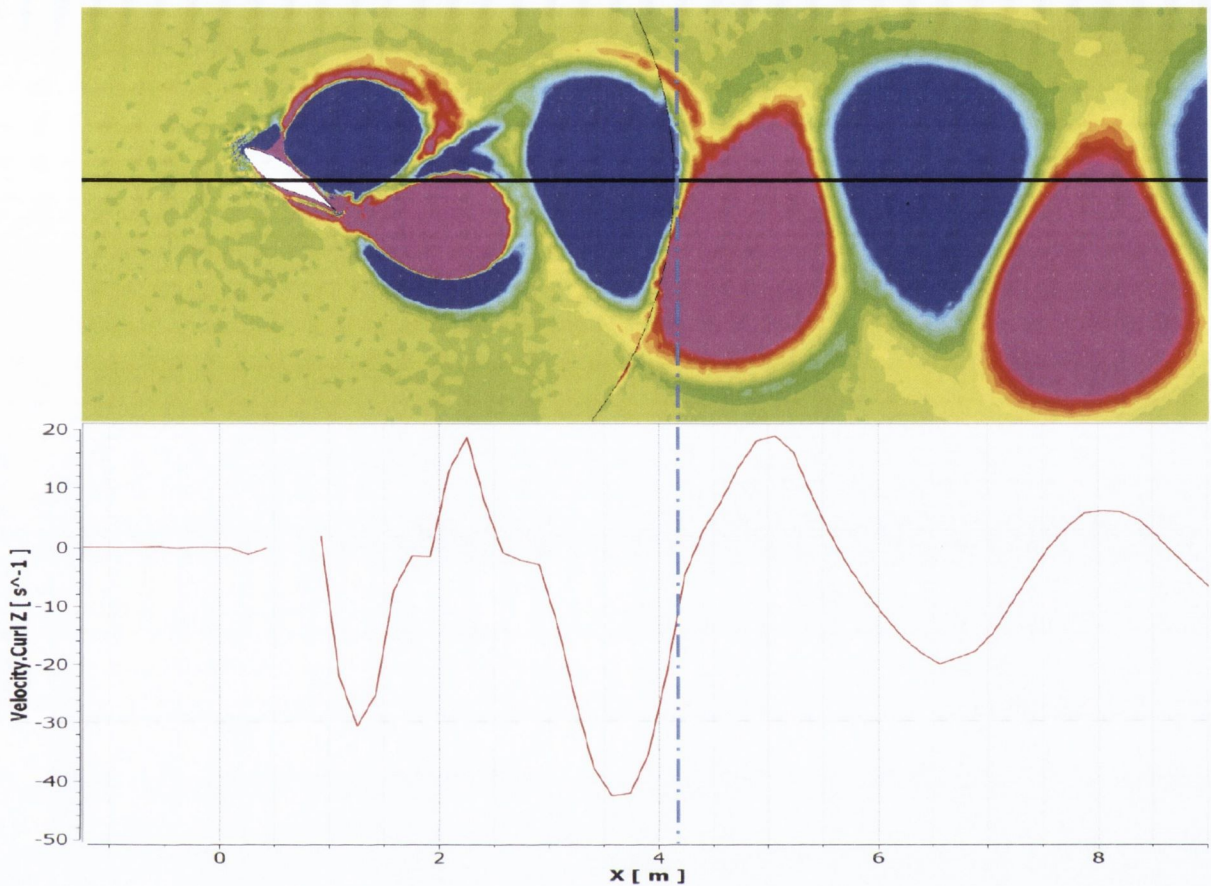


Figure 7.16: Upper figure: instantaneous vorticity over a portion of the flow field; —, horizontal line probe. Lower figure: —, vorticity record along a horizontal line probe.

7.3 Summary

The vortex shedding behaviour of the NREL S809 subject to a 2-degrees of freedom motion has been examined. Two different couplings are considered, stream-wise/transverse and stream-wise/pitching motions. The effect that the stream-wise motion has on the transverse and pitching lock-in behaviour has been studied for two sample angles of attack, $\alpha_{mean} = 40^\circ$ and $\alpha_{mean} = 140^\circ$, with the aim to investigate how much one or the other motion of the coupling affects the most the global vortex shedding behaviour of the system. It has been found that the lock-in behaviour associated with the pure transverse motion is more resilient against the action of the coupled stream-wise motion when the upwind edge is sharp (trailing edge in this case, $\alpha_{mean} = 140^\circ$). This seems to represent a more stable configuration as the flow separation point on the leading edge is well defined. The same behaviour has been observed for the lock-in associated with the pure pitching

motion (coupled with the stream-wise one).

The phase between the coupled motions has been considered, whose effect seems to be more significant when the upwind edge is rounded (leading edge in this case, $\alpha_{mean} = 40^\circ$). At this incidence, the behaviour of the two different couplings appears to be different. It has been observed that for $\phi = 90^\circ$ the risk of synchronisation is slightly reduced in the case of coupled stream-wise/transverse motion; whereas in the case of coupled stream-wise/pitching motion a $\phi = 90^\circ$ seems to make the wake more resilient against the stream-wise effect.

In general, different vortex shedding behaviours have been observed depending on when the counter-clockwise vortex is formed; that is, if the trailing edge is moving in the upstream-downstream direction or vice versa. And also, depending on the manner in which the clockwise vortex detaches; that is, if the detachment is caused more by the counter vorticity or by the airfoil's motion. These two aspects give importance to the action of the local flow velocity with respect to the moving boundaries (airfoil) velocity.

Chapter 8

Conclusions

The unsteady flow around an oscillating airfoil (NREL S809) at high angles of attack has been studied by means of URANS simulations, in order to investigate the vortex shedding behaviour (i.e. frequency lock-in). The types of motion considered are three single degrees of freedom (pitching, stream-wise, transverse) and two 2-degrees of freedom couplings (stream-wise/transverse, stream-wise/pitching); all forced sinusoidal oscillations. It has been observed that:

- synchronisation of the vortex shedding and motion frequencies is present for all the types of motion analysed, albeit with different behaviours (different range of angles of attack, different range of frequency ratios, different harmonics locked-in to);
- the flow separation/reattachment point on the leading edge strongly affects the lock-in behaviour;
- the width of the wake is defined by the near wake flow, which in turn is defined by the flow separation points on the leading and trailing edges.

In addition, some considerations can be advanced:

- if the flow velocity, U_∞ , increases, so does the static vortex shedding, f_{v0} , hence the frequency ratio, r , decreases (with the motion frequency remaining the same). This means that synchronisation is more likely to occur (a lock-out condition for a given frequency ratio on the maps presented in this work for a unique flow velocity may turn into a lock-in condition at the same frequency ratio as the flow velocity is increased);

- a 2-D approach (as used in this work), linked to the RANS method and turbulence model (which in this case is isotropic), represents a strong simplification of the system. A more realistic scenario with 3-dimensionality and fully turbulent flow is likely to cause a more rapid dissipation of the wake and a less periodic/coherent behaviour, due to the span-wise correlation and more significant shear stresses in the wake. The enhanced dissipation process of the vortex shedding may lead to a less pronounced lock-in regime. It is believed that 2-dimensionality and turbulence modelling give rise to behaviours that would not happen in 3-D. For example the observed pseudo-lock-in conditions (in 2-D) is likely to be a lock-out condition in 3-D;
- on the basis of the considerations above, a 2-D approach seems to be sensible, being more pessimistic and, therefore, safer from an engineering point of view;
- on the other hand, a form of carefulness in assessing lock-in is needed. For example, in some cases, obtaining a lock-in or lock-out condition might be more a matter of vortex shedding dissipation rather than motion frequency. It may happen that the CFD model features (e.g. turbulence model, mesh extent) do not allow vortex shedding periodicity even if it exists in a real case, as the dissipation of the vortex pattern occurs before it can replicate itself.

Other than the numerical model (CFD), a lumped parameter model for VIV of airfoils is also proposed, for a single degree of freedom motion (pitching, transverse). The main outcome is that it does not seem possible to obtain an universal set of parameters for VIV of airfoils at different angles of attack, since the geometry is not taken into account. Generally, the possibility of this model to be used for a fully coupled system seems to be remote, as more complex modelling is needed.

8.1 Future Work

From the conclusions drawn in this study, it is apparent that more work is needed, as this study represents an initial step towards a clear understanding of VIV of airfoils at very high angles of attack. Many simplifications have been adopted: 2-D approach, uniform

flow velocity profile, RANS method, limited amount of simulated time (yet apparently reasonable). Therefore, as a general comment, future work should involve a more realistic scenario. For example, including 3-dimensionality, blade taper, sheared flow velocity profile. In addition, a longer simulated time may clarify some ambiguous behaviours (here addressed as “pseudo-lock-in” and “transitional” conditions). More specifically, some avenues for future work are:

- LES/DES method, to treat turbulence with a different approach;
- three degrees of freedom coupled motion (pitching, stream-wise, transverse);
- free vibrating system (*coupled system model* as per Païdoussis *et al.* [16]);
- parametric study with different flow velocities/Reynolds numbers;
- experiments should be conducted to confirm/verify the reliability of the results coming from CFD calculations.

Nonetheless, this thesis presents information on the indicative behaviour of an airfoil typical of wind turbine blades at high angles of attack.

Bibliography

- [1] T. Burton, N. Jenkins, D. Sharpe, and E. Bossanyi. *Wind energy handbook*. Wiley, 2011.
- [2] D.A. Spera. *Wind turbine technology*. 1994.
- [3] Anon. *BP Statistical Review of World Energy 2013*. BP, 2013.
- [4] R. Priddle. *World Energy Outlook 2010*. International Energy Agency, 2010.
- [5] P. Ruffles. *The Cost of Generating Electricity*. The Royal Academy of Engineers, 2004.
- [6] IEC. Wind turbines. part 1: Design requirements. *Technical Report, International Electrotechnical Commission*, 61400-1:2005+A1:2010.
- [7] V.A. Riziotis, S.G. Voutsinas, E.S. Politis, and P.K. Chaviaropoulos. Aeroelastic stability of wind turbines: the problem, the methods and the issues. *Wind Energy*, 7(4):373–392, 2004.
- [8] M.O.L. Hansen and M.H. Aagaard. Review paper on wind turbine aerodynamics. *Journal of fluids engineering*, 133(11), 2011.
- [9] G.N. Barakos and D. Drikakis. Computational study of unsteady turbulent flows around oscillating and ramping aerofoils. *International Journal for Numerical Methods in Fluids*, 42(2):163–186, 2003.
- [10] R. Elakoury, M. Braza, Y. Hoarau, J. Vos, G. Harran, and A. Sevrain. Unsteady flow around a naca0021 airfoil beyond stall at 60° angle of attack. *IUTAM Symposium, Unsteady Separated Flows and their control, Corfu-Greece*, 2007.

- [11] M.O.L. Hansen, J.N. Sørensen, S. Voutsinas, N. Sørensen, and H.A. Madsen. State of the art in wind turbine aerodynamics and aeroelasticity. *Progress in Aerospace Sciences*, 42(4):285–330, 2006.
- [12] Z. Liu and G.A. Kopp. A numerical study of geometric effects on vortex shedding from elongated bluff bodies. *Journal of Wind Engineering and Industrial Aerodynamics*, 101:1–11, 2012.
- [13] E. Naudascher and D. Rockwell. Oscillator-model approach to the identification and assessment of flow-induced vibrations in a system. *Journal of Hydraulic Research*, 18:59–82, 1980.
- [14] E. Naudascher and D. Rockwell. *Flow-Induced Vibrations: An Engineering Guide*. Rotterdam: A.A. Balkema, 1994.
- [15] D.S. Weaver. On flow induced vibrations in hydraulic structures and their alleviation. *Canadian Journal of Civil Engineering*, 3(1):126–137, 1976.
- [16] M.P. Païdoussis, S. Price, and E. de Langre. *Fluid-structure Interactions: Cross-flow-induced Instabilities*. Cambridge University Press, 2010.
- [17] R.D. Blevins. *Flow-induced vibration*. New York, 1990.
- [18] A. Roshko. Perspectives on bluff body aerodynamics. *Journal of Wind Engineering and Industrial Aerodynamics*, 49(1-3):79–100, 1993.
- [19] Th. von Kármán. Über den Mechanismus des Widerstandes, den ein bewegter Körper in einer Flüssigkeit erfährt. *Nachrichten von der Gesellschaft der Wissenschaften zu Göttingen, Mathematisch-Physikalische Klasse*, 1911:509–517, 1911.
- [20] A. Fage and F.C. Johansen. On the flow of air behind an inclined flat plate of infinite span. *Proceedings of the Royal Society of London. Series A, Containing Papers of a Mathematical and Physical Character*, 116(773):170–197, 1927.
- [21] A. Roshko. On the drag and shedding frequency of two-dimensional bluff bodies. *Technical Report, DTIC Document*, 1954.

- [22] D.B. Steinman. Bridges and aerodynamics. *Transactions of the New York Academy of Sciences*, 16(3 Series II):125–141, 1954.
- [23] R. King. A review of vortex shedding research and its application. *Ocean Engineering*, 4(3):141–171, 1977.
- [24] Y.C. Fung. Fluctuating lift and drag acting on a cylinder in a flow at supercritical reynolds numbers. *Journal of the Aerospace Sciences*, 27(11):801–814, 1960.
- [25] M.M. Zdravkovich. Flow around circular cylinders, vol. 1. Fundamentals. *Journal of Fluid Mechanics*, 350:377–378, 1997.
- [26] C.H.K. Williamson. Vortex dynamics in the cylinder wake. *Annual review of fluid mechanics*, 28(1):477–539, 1996.
- [27] J.H. Gerrard. The mechanics of the formation region of vortices behind bluff bodies. *Journal of Fluid Mechanics*, 25(2):401–413, 1966.
- [28] C. Norberg. Fluctuating lift on a circular cylinder: review and new measurements. *Journal of Fluids and Structures*, 17(1):57–96, 2003.
- [29] P. Sonnevile. Etude de la structure tridimensionnelle des écoulements autour d'un cylindre circulaire. *Bulletin de la Direction des Etudes et Recherches, Electricité de France, Serie A, No. 3*, 1976.
- [30] C. Farell. Flow around fixed circular cylinders: Fluctuating loads. *Journal of the Engineering Mechanics Division*, 107(3):565–588, 1981.
- [31] K. Shimada and T. Ishihara. Application of a modified $k - \varepsilon$ model to the prediction of aerodynamic characteristics of rectangular cross-section cylinders. *Journal of Fluids and Structures*, 16(4):465–485, 2002.
- [32] J.H. Lienhard. *Synopsis of lift, drag, and vortex frequency data for rigid circular cylinders*. Washington State University, College of Engineering, Research Division Bulletin 300, 1966.

- [33] Z.J. Taylor, R. Gurka, and G.A. Kopp. Effects of leading edge geometry on the vortex shedding frequency of an elongated bluff body at high reynolds numbers. *Journal of Wind Engineering and Industrial Aerodynamics*, 128:66–75, 2014.
- [34] Y. Nakamura, Y. Ohya, S. Ozono, and R. Nakayama. Experimental and numerical analysis of vortex shedding from elongated rectangular cylinders at low reynolds numbers $200 - 10^3$. *Journal of Wind Engineering and Industrial Aerodynamics*, 65(1):301–308, 1996.
- [35] C.W. Knisely. Strouhal numbers of rectangular cylinders at incidence: a review and new data. *Journal of Fluids and Structures*, 4(4):371–393, 1990.
- [36] J.S. Leontini and M.C. Thompson. Vortex-induced vibrations of a diamond cross-section: Sensitivity to corner sharpness. *Journal of Fluids and Structures*, 39:371–390, 2013.
- [37] R. Parker and M.C. Welsh. Effects of sound on flow separation from blunt flat plates. *International Journal of Heat and Fluid Flow*, 4(2):113–127, 1983.
- [38] A.L. Csiba and R.J. Martinuzzi. Investigation of bluff body asymmetry on the properties of vortex shedding. *Journal of Wind Engineering and Industrial Aerodynamics*, 96(6):1152–1163, 2008.
- [39] A.E. Perry and T.R. Steiner. Large-scale vortex structures in turbulent wakes behind bluff bodies. Part 1. Vortex formation processes. *Journal of Fluid Mechanics*, 174:233–270, 1987.
- [40] K.M. Lam. Phase-locked eduction of vortex shedding in flow past an inclined flat plate. *Physics of Fluids*, 8:1159, 1996.
- [41] K.M. Lam and M.Y.H. Leung. Asymmetric vortex shedding flow past an inclined flat plate at high incidence. *European Journal of Mechanics-B/Fluids*, 24(1):33–48, 2005.

- [42] M. Breuer, N. Jovičić, and K. Mazaev. Comparison of DES, RANS and LES for the separated flow around a flat plate at high incidence. *International Journal for Numerical Methods in Fluids*, 41(4):357–388, 2003.
- [43] M.T. Nair and T.K. Sengupta. Onset of asymmetry: flow past circular and elliptic cylinders. *International Journal for Numerical Methods in Fluids*, 23(12):1327–1345, 1996.
- [44] M.T. Nair and T.K. Sengupta. Unsteady flow past elliptic cylinders. *Journal of Fluids and Structures*, 11(6):555–595, 1997.
- [45] D. Medici and P.H. Alfredsson. Measurements on a wind turbine wake: 3D effects and bluff body vortex shedding. *Wind Energy*, 9(3):219–236, 2006.
- [46] E. Simiu and R.H. Scanlan. *Wind effects on structures: an introduction to wind engineering*. New York, 1978.
- [47] N.N. Sørensen, J. Johansen, and S. Conway. *CFD computations of wind turbine blade loads during standstill operation - KNOW-BLADE, Task 3.1 report*. Risø National Laboratory, Roskilde, Denmark, 2004.
- [48] W. Skrzypiński, M. Gaunaa, N.N. Sørensen, F. Zahle, and J. Heinz. Vortex-induced vibrations of a DU96-W-180 airfoil at 90° angle of attack. *Wind Energy*, 17(10):1495–1514, 2014.
- [49] C.H.K. Williamson and R. Govardhan. A brief review of recent results in vortex-induced vibrations. *Journal of Wind Engineering and Industrial Aerodynamics*, 96(6-7):713–735, 2008.
- [50] C.H.K. Williamson and R. Govardhan. Vortex-induced vibrations. *Annual Review of Fluid Mechanics*, 36:413–455, 2004.
- [51] T. Sarpkaya. A critical review of the intrinsic nature of vortex-induced vibrations. *Journal of Fluids and Structures*, 19(4):389–447, 2004.

- [52] P.K. Stansby. The locking-on of vortex shedding due to the cross-stream vibration of circular cylinders in uniform and shear flows. *Journal of Fluid Mechanics*, 74(4):641–665, 1976.
- [53] E. Konstantinidis. On the response and wake modes of a cylinder undergoing stream-wise vortex-induced vibration. *Journal of Fluids and Structures*, 45:256–262, 2014.
- [54] M.M. Bernitsas, K. Raghavan, Y. Ben-Simon, and E.M. Garcia. VIVACE (Vortex Induced Vibration Aquatic Clean Energy): a new concept in generation of clean and renewable energy from fluid flow. *Journal of Offshore Mechanics and Arctic Engineering*, 130(4):041101, 2008.
- [55] R.E.D. Bishop and A.Y. Hassan. The lift and drag forces on a circular cylinder oscillating in a flowing fluid. *Proceedings of the Royal Society of London. Series A. Mathematical and Physical Sciences*, 277(1368):51–75, 1964.
- [56] C.C. Feng. *The measurement of vortex induced effects in flow past stationary and oscillating circular and D-section cylinders*. MAsc Thesis, 1968.
- [57] C.H.K. Williamson and A. Roshko. Vortex formation in the wake of an oscillating cylinder. *Journal of Fluids and Structures*, 2(4):355–381, 1988.
- [58] A. D. Trim, H. Braaten, H. Lie, and M. A. Tognarelli. Experimental investigation of vortex-induced vibration of long marine risers. *Journal of Fluids and Structures*, 21(3):335–361, 2005.
- [59] Z. Chen and W.J. Kim. Numerical investigation of vortex shedding and vortex-induced vibration for flexible riser models. *International Journal of Naval Architecture and Ocean Engineering*, 2(2):112–118, 2010.
- [60] R.H.J. Willden and J.M.R. Graham. Numerical prediction of VIV on long flexible circular cylinders. *Journal of Fluids and Structures*, 15(3):659–669, 2001.
- [61] H. Kawai. Vortex induced vibration of tall buildings. *Journal of Wind Engineering and Industrial Aerodynamics*, 41(1):117–128, 1992.

- [62] G. Diana, F. Resta, M. Belloli, and D. Rocchi. On the vortex shedding forcing on suspension bridge deck. *Journal of Wind Engineering and Industrial Aerodynamics*, 94(5):341–363, 2006.
- [63] O.M. Griffin and S.E. Ramberg. Vortex shedding from a cylinder vibrating in line with an incident uniform flow. *Journal of Fluid Mechanics*, 75(02):257–271, 1976.
- [64] C.H.K. Williamson and N. Jauvtis. A high-amplitude 2T mode of vortex-induced vibration for a light body in XY motion. *European Journal of Mechanics-B/Fluids*, 23(1):107–114, 2004.
- [65] O.M. Griffin and S.E. Ramberg. The vortex-street wakes of vibrating cylinders. *Journal of Fluid Mechanics*, 66(03):553–576, 1974.
- [66] E. Naudascher. Flow-induced streamwise vibrations of structures. *Journal of Fluids and Structures*, 1(3):265–298, 1987.
- [67] S. Mittal and T.E. Tezduyar. A finite element study of incompressible flows past oscillating cylinders and aerofoils. *International Journal for Numerical Methods in Fluids*, 15(9):1073–1118, 1992.
- [68] T. Srikanth, H.N. Dixit, R. Tatavarti, and R. Govindarajan. Vortex shedding patterns, their competition, and chaos in flow past inline oscillating rectangular cylinders. *Physics of Fluids (1994-present)*, 23(7):073603, 2011.
- [69] N. Cagney and S. Balabani. Mode competition in streamwise-only vortex induced vibrations. *Journal of Fluids and Structures*, 41:156–165, 2013.
- [70] N. Cagney and S. Balabani. Wake modes of a cylinder undergoing free streamwise vortex-induced vibrations. *Journal of Fluids and Structures*, 38:127–145, 2013.
- [71] N. Jauvtis and C.H.K. Williamson. Vortex-induced vibration of a cylinder with two degrees of freedom. *Journal of Fluids and Structures*, 17(7):1035–1042, 2003.
- [72] T. Theodorsen. General theory of aerodynamic instability and the mechanism of flutter. 1935.

- [73] I.E. Garrick. *Propulsion of a flapping and oscillating airfoil*. NACA Report 567. US Government Printing Office, Washington, DC, 1937.
- [74] R. Katzmayr. *Effect of periodic changes of angle of attack on behavior of airfoils*. National Advisory Committee for Aeronautics, 1922.
- [75] W.J. McCroskey. Unsteady airfoils. *Annual review of Fluid Mechanics*, 14(1):285–311, 1982.
- [76] L.W. Carr. Progress in analysis and prediction of dynamic stall. *Journal of Aircraft*, 25(1):6–17, 1988.
- [77] W.J. McCroskey, L.W. Carr, and K.W. McAlister. Dynamic stall experiments on oscillating airfoils. *AIAA Journal*, 14(1):57–63, 1976.
- [78] M.M. Koochesfahani. Vortical patterns in the wake of an oscillating airfoil. *AIAA Journal*, 27(9):1200–1205, 1989.
- [79] J.W. Chang and H. Eun. Reduced frequency effects on the near-wake of an oscillating elliptic airfoil. *Journal of Mechanical Science and Technology*, 17(8):1234–1245, 2003.
- [80] M.H. Akbari and S.J. Price. Simulation of the flow over elliptic airfoils oscillating at large angles of attack. *Journal of Fluids and Structures*, 14(6):757–777, 2000.
- [81] D.E. Raveh and E.H. Dowell. Frequency lock-in phenomenon for oscillating airfoils in buffeting flows. *Journal of Fluids and Structures*, 27(1):89–104, 2011.
- [82] B. Zhu and K. Kamemoto. Probability of self-oscillation induced by vortex shedding from a thin cambered blade. *Experimental thermal and fluid science*, 29(1):129–135, 2004.
- [83] J. Johansen, N.N. Sørensen, J.A. Michelsen, and S. Schreck. Detached-eddy simulation of flow around the NREL phase VI blade. *Wind Energy*, 5(2-3):185–197, 2002.

- [84] G.H. Yu, X.C. Zhu, and Z.H. Du. Numerical simulation of a wind turbine airfoil dynamic stall and comparison with experiments. *Journal of Power and Energy*, 224(5):657, 2010.
- [85] H. Hasegawa and K. Nakagawa. Dynamic behavior of vortex shedding from an oscillating three-dimensional airfoil. *Proceedings of the 27th Congress of the International Council of the Aeronautical Sciences*, 2010.
- [86] D. Tang and E.H. Dowell. Experimental aerodynamic response for an oscillating airfoil in buffeting flow. *AIAA Journal*, 52(6):1170–1179, 2014.
- [87] Besem F.M., Kamrass J.D., J.P. Thomas, Tang D., and Kielb R.E. Vortex-induced vibration and frequency lock-in of an airfoil at high angles of attack. *Proceedings of ASME Turbomachinery Exposition 2014 - Düsseldorf, Germany, June 16-20, 2014*.
- [88] Z.J. Wang. Vortex shedding and frequency selection in flapping flight. *Journal of Fluid Mechanics*, 410(1):323–341, 2000.
- [89] J.C.S. Lai and M.F. Platzer. Jet characteristics of a plunging airfoil. *AIAA Journal*, 37(12):1529–1537, 1999.
- [90] J. Young and J.C.S. Lai. Vortex lock-in phenomenon in the wake of a plunging airfoil. *AIAA Journal*, 45(2):485–490, 2007.
- [91] R.S. Ehrmann, K.M. Loftin, S. Johnson, and E.B. White. Lock-in of elastically mounted airfoils at a 90° angle of attack. *Journal of Fluids and Structures*, 44:205–215, 2014.
- [92] H. Glauert. The force and moment on an oscillating aerofoil. *Vorträge aus dem Gebiete der Aerodynamik und verwandter Gebiete*, pages 88–95, 1930.
- [93] M.F. Platzer, K.D. Jones, J. Young, and J.C.S. Lai. Flapping wing aerodynamics: progress and challenges. *AIAA Journal*, 46(9):2136–2149, 2008.
- [94] K. Ohmi, M. Coutanceau, T.P. Loc, and A. Dulieu. Vortex formation around an oscillating and translating airfoil at large incidences. *Journal of Fluid Mechanics*, 211:37–60, 1990.

- [95] K. Ohmi, M. Coutanceau, O. Daube, and T.P. Loc. Further experiments on vortex formation around an oscillating and translating airfoil at large incidences. *Journal of Fluid Mechanics*, 225:607–630, 1991.
- [96] I.H. Tuncer and M.F. Platzer. Computational study of flapping airfoil aerodynamics. *Journal of Aircraft*, 37(3):514–520, 2000.
- [97] M.A. Ashraf, J. Young, and J.C.S. Lai. Reynolds number, thickness and camber effects on flapping airfoil propulsion. *Journal of Fluids and Structures*, 27(2):145–160, 2011.
- [98] K. Isogai, Y. Shinmoto, and Y. Watanabe. Effects of dynamic stall on propulsive efficiency and thrust of flapping airfoil. *AIAA Journal*, 37(10):1145–1151, 1999.
- [99] O. Guerri, A. Hamdouni, and A. Sakout. Fluid structure interaction of wind turbine airfoils. *Wind Engineering*, 32(6):539–557, 2008.
- [100] C. Maresca, D. Favier, and J. Rebont. Experiments on an aerofoil at high angle of incidence in longitudinal oscillations. *Journal of Fluid Mechanics*, 92(04):671–690, 1979.
- [101] W.J. McCroskey. The 1976 freeman scholar lecture: Some current research in unsteady fluid dynamics. *Journal of fluids engineering*, 99(1):8–39, 1977.
- [102] D. Favier, A. Agnes, C. Barbi, and C. Maresca. Combined translation/pitch motion—a new airfoil dynamic stall simulation. *Journal of Aircraft*, 25(9):805–814, 1988.
- [103] D.M. Somers. Design and experimental results for the S809 airfoil. Technical Report NREL/SR-440-6918; ON: DE97000206; TRN: 97:001243, 1997. Airfoils, Inc., State College, PA, United States.
- [104] ESDU 96030. *Response of structures to vortex shedding: structures of circular or polygonal cross section*. The Institution of Mechanical Engineers, 1998.
- [105] R. D. Gabbai and H. Benaroya. An overview of modeling and experiments of vortex-induced vibration of circular cylinders. *Journal of Sound and Vibration*, 282(35):575–616, 2005.

- [106] R.E.D. Bishop and A.Y. Hassan. The lift and drag forces on a circular cylinder in a flowing fluid. *Proceedings of the Royal Society of London. Series A. Mathematical and Physical Sciences*, 277(1368):32–50, 1964.
- [107] R.T. Hartlen and I.G. Currie. Lift-oscillator model of vortex-induced vibration. *Journal of the Engineering Mechanics Division*, 96(5):577–591, 1970.
- [108] M.L. Facchinetti, E. de Langre, and F. Biolley. Coupling of structure and wake oscillators in vortex-induced vibrations. *Journal of Fluids and Structures*, 19(2):123–140, 2004.